Nanomaterials Design and Fabrication for Solar Energy Conversion and Photocatalysis Applications

Submitted by Bandar Alfaifi, to the University of Exeter
as a thesis for the degree of
Doctor of Philosophy in Renewable Energy
In November 2018.

I certify that all material in this thesis which is not my own work has been identified and that no material has previously been submitted and approved for the award of a degree by this or any other University.

(Signature)……

Abstract

The use of nanomaterials in solar energy conversion and photocatalytic degradation of environmental pollutants represents an opportunity to improve the performance, density, and ease of transportation in renewable resources. Among renewables resources, solar energy is considered as the largest exploitable resource, supplying the earth with energy in 1 hour equivalent to mankind's total energy consumption in an entire year. Collecting and storing sunlight in chemical bonds (solar fuel) using photoelectrochemical water splitting (PEC) is a promising, a clean and sustainable way for hydrogen generation. Moreover, the photocatalytic process has great potential and high efficiency for removal of organic pollutants from water under direct natural sunlight irradiation. The aim of this project is to design, fabricate, characterize and performance enhancement of novel semiconductor materials that could efficiently harvest and store solar energy by splitting water to produce hydrogen and to perform dye degradation as well. The lack of suitable p-type photocathode has been considered and the focus of this work was to design and develop the new stable visible light absorbing photocathode materials.

In pursuit of the stable photocathode, in this work $YFeO_3$, which is a cheap and abundant material, with promising properties, and so was chosen as the photocathode in the development of the PEC cell. $YFeO_3$ thin films were produced by spray pyrolysis technique onto fluorine-doped tin oxide film on glass. Results showed that $YFeO_3$ photoelectrode has achieved a photocurrent of 0.6 mA cm^{-2} at 0.5 V vs. RHE and maximum of 0.41 μmol/cm^2 of hydrogen has obtained as well.

Similarly, to look for suitable and cheap materials for environmental remediation, Bi_2WO_6 thin films were produced by spray pyrolysis and aerosol-assisted chemical vapour deposition techniques. Results showed that the nanostructure and texture of the films can be controlled by controlling the deposition parameters. Moreover, photocatalytic degradation of rhodamine B (RhB) and methylene blue (MB) dyes have been successfully achieved.

Finally, α-Fe_2O_3 films were fabricated as counter electrodes for dye-sensitized solar cells in order to compete for platinum counter electrode. These films were fabricated using aerosol-assisted chemical vapour deposition and spray pyrolysis techniques. The results showed that the performance of the samples prepared by aerosol-assisted chemical vapour deposition as a counter electrodes is higher than of the samples prepared by spray pyrolysis.

.

Acknowledgments

Firstly, I do thank god who gave me the strength, health, and ability to complete this work. I would like to express the deepest appreciation to my supervisors Dr. Asif Ali Tahir for the continuous support of my PhD study, for his patience, motivation and immense knowledge. His guidance helped me throughout my research and writing. I would like to thank my co-supervisors Prof Tapas Mallick and Dr. Senthilarasu for their support.

I would also like to thank my colloquies at the solar group for the stimulating discussions and suggestions, and my friends for the times in and out of university. My PhD experience would not have been the same without any of them.

I am very grateful to the Ministry of Higher Education at the Kingdom of Saudi Arabia, for providing the scholarship funding my PhD at the University of Exeter.

Last but not the least, I would like to thank my parents; my family, my loved wife and my little one for their joining and completing this journey in a country away from the whole family.

Table of Contents

List of Tables

List of Figures

List of Abbreviations

AACVD	Aerosol-Assisted Chemical Vapour Deposition
AFM	Atomic Force Microscope
AP	Artificial Photosynthesis
CB	Conduction Band
CE	Counter Electrode
DSSCs	Dye Sensitized Solar Cells
EDX	Energy-Dispersive X-Ray Spectroscopy
EIS	Electrochemical Impedance Spectroscopy
FE-SEM	Field Emission Scanning Electron Microscope
FTO	Fluorine Doped Tin Oxide
GC	Gas Chromatography
HMA	Hybrid Microwave Annealing
LSV	Liner Sweep Voltammetry
NHE	Normal Hydrogen Electrode
NPs	Nanoparticles
NP	Natural Photosynthesis
NRs	Nanoroads
NTs	Nanotubes
PC	Photocatalytic
PEC	Photoelectrochemical
PV	Photovoltaic
RGO	Reduced Graphene Oxide
RHE	Reversible Hydrogen Electrode
SCE	Saturated Calomel Electrode
SEM	Scanning Electron Microscopy
SP	Spray Pyrolysis
TEM	Transmission Electron Microscopy
TF-VLS	Thin Film Vapour Liquid Solid
UV/Vis	Ultraviolet Visible Spectroscopy
VB	Valence Band
V_{fb}	Flat Band Potential
XRD	X-Ray Diffraction

Chapter 1: Introduction

The motivation of this project is presented in this chapter and various applications of solar energy conversion were discussed. One of which is the photoelectrochemical process which directly harvests the solar energy and converts such energy to split water to produce hydrogen. Hydrogen was the desired product because hydrogen could be used as fuel and chemical feedstock for different processes. The solar hydrogen generation is considered as Holy Grail of future fuel but its development is hindered due to lack of suitable nanomaterials. Another application is focused on solar photocatalysis for water remediation. Solar energy can be used to remove different pollutants from water. The photocatalysis also has the same requirement of stable and suitable nanomaterials. The aims and objectives of this thesis are described. The thesis outline is then presented.

1.1. Solar Energy for Energy Application

Traditional sources of energy such as coal, oil and natural gas have supplied the world with energy and driven developments. However, global energy consumption has increased dramatically and it is estimated that this will double by 2050.[1] Fossil fuel resources are limited and are concentrated in certain regions around the world. Therefore, while global demand is increasing, a secure supply is increasingly challenging to assure.[2] Furthermore, There are also environmental and human health impacts. Moreover, the emissions of greenhouse gas and carbon dioxide have a negative impact on our planet.

Renewable energy resources such as wind, biomass and solar fuel have been investigated for years to help with the replacement of fossil fuels. Extensive

research and development have been required to produce such a technology that can compete with fossil fuels and be commercially viable everywhere. The most developed renewable energy sources are based on electricity generation, producing a transportable and storable fuel, all of which presents challenges.

Among these energy resources, solar energy is considered a primary carrier that may hold potential promise for a sustainable and clean energy future.[3] Solar energy focusses on direct conversion of sunlight into chemical fuels in the form of hydrogen gas (H_2).[4] The most developed application of solar energy is to convert light into solar fuel, (hydrogen fuel), by splitting water into oxygen and hydrogen. The advantages and appeal of solar water splitting, include the small reaction potential required (1.23 eV), and zero CO_2 emission, as well as the ready availability of the raw materials, i.e. sunlight and water.[5] However, solar energy use is still limited, and researchers are focusing on the development of improved technologies for solar energy conversion. Moreover, sufficient materials are needed to achieve efficient solar to hydrogen conversion. A thorough understanding of the mechanism of photoelectrochemical water splitting, techniques and materials used could serve as guidelines for designing new technologies and materials.

1.2. Solar Energy for Environmental Photocatalytic Application

Environmental pollution is a global threat and it is increasing day-by-day due to heavy industrialization, urbanization, and the changing lifestyles of people. Among all types of environmental pollutants, providing clean water have become an issue worldwide. About 70% of water on the Earth is trapped in the ice or glaciers and only 0.08% of the remaining water is clean.[6] With the shortage of clean water sources and increasing demand, several practical solutions have

been implemented to sustain more viable water resources. Storing the rainwater for daily uses and expanding the catchment capacity for stormwater are just a few examples of short-term solutions. Developing countries with a sunshine arid area, less rainfall, and long-term drought have the challenge to find viable water resources. Therefore, we need a technology that is capable to monitor, detect and clean the contaminants from the existing water.

Nanomaterials offer a great promise for the ability to improve environmental technology. Due to it is small size and the high ratio of surface area to volume ratio, nanomaterials can be used to detect very sensitive contaminants.[6] One of the major application of nanomaterials in the field of environment is photocatalytic degradation of organic pollutant.[7]

Photocatalytic degradation using solar energy is an advanced oxidation process that can be able to degrade of organic pollutants in a simple and efficient manner. Moreover, it can be used to remove, minimize or neutralize the water contaminants that can harm human health. Therefore, it is considered as one of the most economical and promising industrial techniques for water treatments. However, solar energy for photocatalytic degradation is limited due to the lack of suitable materials. The need for designing highly efficient photocatalytic systems and suitable material for water treatment is of vital interest.

1.3. Aims and Objectives

The aims of this work are: First, design and development of p-type stable photocathode for photoelectrochemical for hydrogen generation. Second, design and development of suitable photocatalysts for environmental remediation.

To achieve these aims this PhD work is split into the following objectives;

1. literature survey
2. Development of synthetic strategies for the control of optimal nano-architecture and morphology.
3. Characterization of materials to determine phase, crystallinity, morphology and surface properties.
4. UV-Vis for optical characterization.
5. PEC, and photocatalytic analysis to determine the solar energy conversion efficiency.
6. Electrochemical characterization of materials.
7. Testing the materials for hydrogen generation and photocatalytic applications.

Different materials have been used to fulfil these aims. The P-type $YFeO_3$ thin film material is fabricated and their applications in solar energy conversion for H_2 generation is investigated as well. Different fabrication techniques, such as sol-gel, aerosol assisted chemical vapour deposition (AACVD) and spray pyrolysis (SP), have been used to optimize the ideal fabrication conditions of the $YFeO_3$ thin film. In addition, I study their stability, photoactivity, electrical, optical properties, and fabrication method. Moreover, their capability to reuse in water splitting reaction has been investigated. The outcome results are summarized in the submitted article.

Bi_2WO_6 thin films have been designed and fabricated for by AACVD and SP fabrication methods. Their applications in photocatalytic degradation of different organic dyes have been investigated. In addition, their structured, optical and electrical properties have been studied.

α- Fe_2O_3 thin films are fabricated as counter electrodes for dye-sensitized solar cells in order to compete for platinum counter electrode. Different deposition techniques like spray pyrolysis (SP) and aerosol assisted chemical vapour deposition (AACVD) have been used. Their performance, characterization and PEC measurements have been studied.

1.4. Thesis Outline

The work detailed in this thesis is organized in the following manner:

Chapter 1 is an introduction to the thesis including aims and objectives. Chapter 2 is a literature review on nanomaterial designs and fabrication in the context of their applications for solar-to-hydrogen conversion and for photocatalysts in dye degradation. The literature presents an overview of the current state of the field, discussing the different materials that are being investigated before giving a brief description of some state of the art solar-to-hydrogen devices and finishing with a discussion of the current and future challenges in the field. Chapter 3 is a description of the different characterization and experimental techniques used throughout this thesis. Chapter 4 discusses the fabrication of $YFeO_3$ nanomaterial and its advantages in photoelectrochemical water splitting as a photocathode for hydrogen generation. Chapter 5 focuses on the fabrication of Bi_2WO_6 films using a spray pyrolysis technique and how they act as photo-catalyst for Rhodamine B (RhB) dye degradation. Chapter 6 discusses another fabrication method used to fabricate Bi_2WO_6 films which can be used as photo-catalyst for Methylene Blue (MB) dye degradation. Chapter 7 is based on collaborative work and focuses on the fabrication of α-Fe_2O_3 counter electrodes for dye-sensitized solar cells. The conclusion and possibilities for future work are presented in chapter 8.

1.5. References

(1) Crabtree, G. W.; Dresselhaus, M. S.; Buchanan, M. V. *Phys. Today.* **2004**, 39.

(2) Ginley, D.; Green, M. a.; Collins, R. *MRS Bull.* **2008**, *33* (04), 355.

(3) Park, H. G.; Holt, J. K. *Energy Environ. Sci.* **2010**, *3* (8), 1028.

(4) Crabtree, G. W.; Dresselhaus, M. S. *MRS Bull.* **2008**, *33*, 421.

(5) Walter, M. G.; Warren, E. L.; McKone, J. R.; Boettcher, S. W.; Mi, Q.; Santori, E. a.; Lewis, N. S. *Chem. Rev.* **2010**, *110* (11), 6446.

(6) Yunus, I. S.; Harwin; Kurniawan, A.; Adityawarman, D.; Indarto, A. *Environ. Technol. Rev.* **2012**, *1* (1), 136.

(7) Shan, G.; Yan, S.; Tyagi, R. D.; Surampalli, R. Y.; Zhang, T. C. **2009**, *13* (April), 110.

Chapter 2: Literature Review

This chapter reviews the current state-of-the-art of photoelectrochemical water splitting and photocatalytic dye degradation processes. Several semiconductor materials such as n-type and p-type were discussed. The result of this literature review shows that the general focus on the photoelectrochemical water splitting and photocatalytic dye degradation processes is on the thin film photoelectrodes materials development. The general requirements for the selection of photoelectrode materials were discussed.

2.1. Basic Principles of Photo-Driven Water Splitting

Generating Hydrogen fuel directly from sunlight is based on the natural phenomenon called natural photosynthesis (NP), a process which exists in plant. [1,2] Where sunlight is used to convert water and carbon dioxide into oxygen and carbohydrates. The potential technology that converts water into H_2 and O_2 using sunlight for generation of solar fuel is referred to as artificial photosynthesis (AP) and mimics NP using man-made materials.[2,3]

The water-splitting reaction is an uphill reaction with a net Gibbs free energy of 238 kJ/mol or 1.23 eV, as shown in Eq. (1-3)[4],

$$H_2O + 2(H^+) \rightarrow {}^1/_2\, O_2 + 2H^2 \quad (HER) \qquad (1)$$

$$2H^+ + 2e^- \rightarrow H_2 \qquad (OER) \qquad (2)$$

$$H_2O \rightarrow {}^1/_2\, O_2 + H_2 \quad \Delta G = 238\ kJ/mol \qquad (3)$$

The basic mechanism of photocatalysis water splitting is based on the generation of photo-excited charge carriers. Photocatalytic water splitting reactions in semiconductor particles generally involves three main steps. Firstly, the

absorption of the light irradiation with energies exceeding the semiconductor bandgap generates electron (e^-) and hole (h^+) pairs inside the semiconductor particles. The generated electrons-holes pairs are subsequently separated, followed by migration of the charges to the interface of the semiconductor particles. The final step is the chemical reaction between the charge carriers and various compounds (e.g., H_2O) produce H_2 and O_2, respectively as shown in Figure 1.[5,6] Recombination of electrons and holes may also occur on a very fast timescale without participating in any chemical reaction.[4,5,7,8]

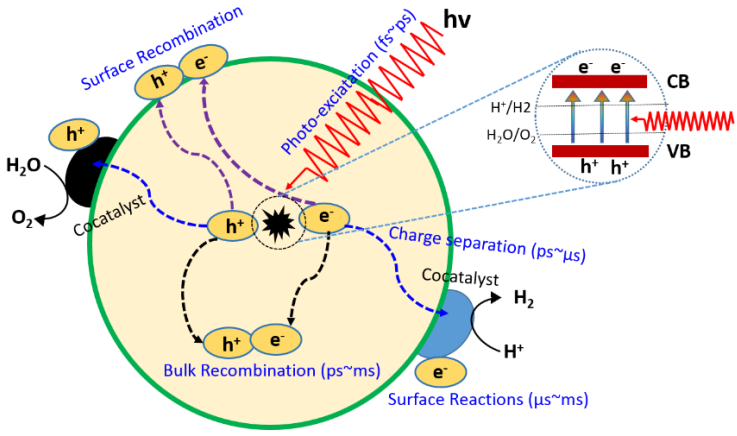

Figure 1: Fundamental principle of photocatalytic water splitting in a semiconductor.

2.2. General Approaches for Water Splitting

Production of Hydrogen, using water splitting techniques fall into two main categories: photocatalyst systems (PC) and photoelectrochemical systems (PEC).[9,10] Photocatalytic systems (PC), considered as the simplest, efficient, and promising method for water splitting. Photocatalysts which form as powders are dispersed in water to split the water molecules under light irradiation (Figure 2). Photocatalysts possess the advantage that the water splitting can occur in the homogeneous phase without the need for transparent electrodes and without the

need for directional illumination.[6] However, PCs have many disadvantages that limit its use for water splitting. (1) Immediate separation of the generated hydrogen and oxygen when formed are required, which will consume additional energy, causing low efficiency of the water splitting process. (2) The illumination of PC systems without fast removal of the catalysts will eventually cause a photostationary state, where all forward and backward reactions have identical rates, and no more water splitting can take place.[11] (3) Due to these limitations, implementing PC systems on a commercial scale remains challenging. Thus, PC systems will not be covered in this literature.

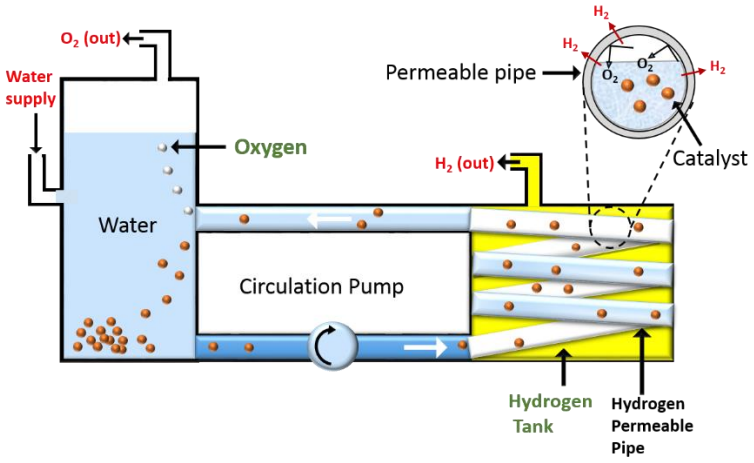

Figure 2: Schematic diagram for solar hydrogen via photocatalytic water splitting system (PC).

In photoelectrochemical water splitting technique (PEC), the photocatalysts are initially prepared on conductive substrates as electrodes and then the additional small bias is applied for water splitting. Photoelectrochemical water splitting was reported for the first time in 1968 using illumination of a conductive electrode made from TiO_2 in aqueous solution.[12] The interaction of incident light with TiO_2 generates electron-hole pairs, where the holes oxidize water at the TiO_2 surface

to generate oxygen, and the electrons travel to the platinum (Pt) counter electrode to split water to produce hydrogen (Figure 3a).[7,8,10,11]

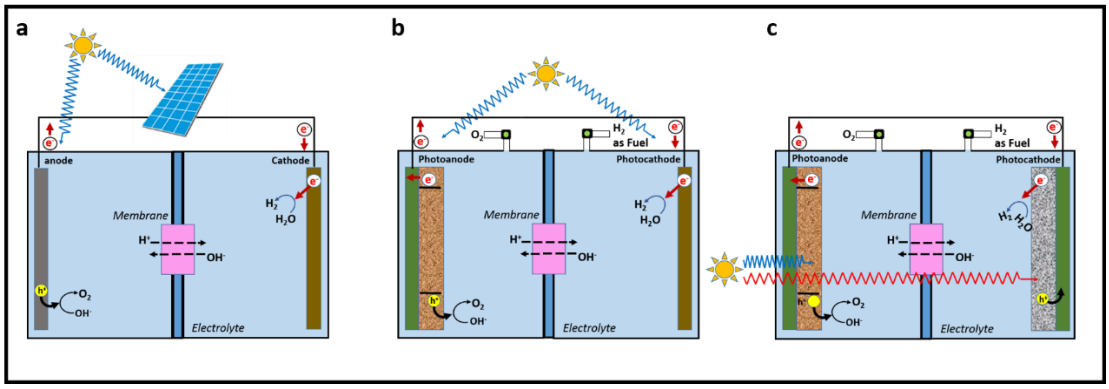

Figure 3: Illustration of PEC configurations: (a) a single photoelectrode PEC powered by a photovoltaic (PV) cell to allow water reduction at the cathode. (b) two photoelectrodes PEC connected in parallel. (c) two photoelectrodes connected in series.

To make a PEC cell, one or both electrodes should be a photoactive semiconductor, where the charge separation forms at the semiconductor/liquid interface (Figure 3b and 3c). When the cell is exposed to sunlight, photogenerated carriers are separated by the space-charge field and the minority charges (holes for an *n*-type photoanode and electrons for a *p*-type photocathode) travel to the semiconductor electrode-liquid interface for reaction.[13] Compared to a photocatalyst system (PC), PECs have the advantage that there is no need for gas separation because the generation of H_2 and O_2 is spatially separated at different electrode sides.[13,14] This literature review discusses different semiconductor materials used to fabricate both photocathodes and photoanodes in PECs.

2.3. Photocathode for Hydrogen Evolution

Water splitting photocathodes are generally p-type semiconductors and must generate the required cathodic current to reduce water to hydrogen and need to

have high stability in aqueous environments. The optimal photocathode material, need to have the conduction band edge potential to be more negative than the hydrogen redox potential. Many earlier studies on electrochemical photocathodes focused on p-type silicon and III-V semiconductors such as InP and GaP. Recently, *p*-type semiconductor including oxides and sulphide have received much attention. In particular various photocathodes materials, including single metallic and bimetallic oxides, chalcopyrites, silicon, and III-V semiconductors.

2.3.1. Single Metallic

Cuprous oxide (Cu_2O), cupric oxide (CuO), and nickel oxide (NiO) are among the forefront *p*-type semiconductor oxides that have been investigated for solar water splitting. They are favourable photocathodes having low cost, earth abundance, and ideal band-gap energies that allow for the absorption of visible light.

2.3.1.1. Cu_2O

Cuprous oxide is one of the most investigated *p*-type semiconductors, used for solar water splitting. Cu_2O has a direct band gap of 1.9-2.2 eV [15], which makes it an excellent solar absorber; however, photocorrosion is a major limitation of Cu_2O.[15,16] Recent studies show that there is a possibility to suppress the photocorrosion of Cu_2O by adding a passivation layer on the surface of Cu_2O (Figure 4a). This layer prevents direct contact between the Cu_2O surface and the surrounding electrolyte.[17] The best performance of Cu_2O was demonstrated in the cathodic reduction of Cu^{2+} ions in aqueous solution with pH 12, where TiO_2 was as a protective layer with a photocurrent of -7.6 mA/cm^2 at 0V vs RHE as shown in Figure 4c.[18]

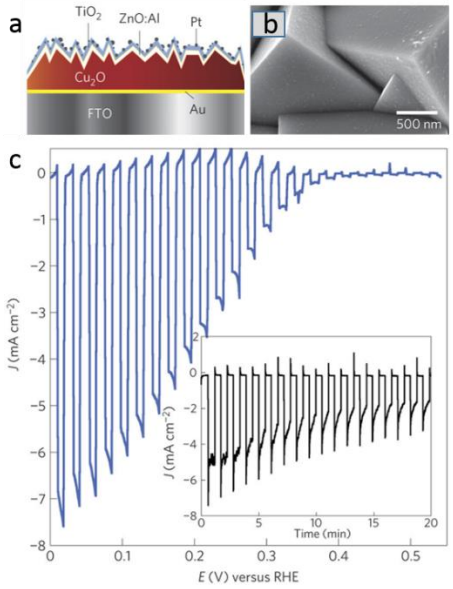

Figure 4: (a) Schematic diagram of FTO/Cu_2O photocathodes deposited with ZnO: Al and TiO_2 protective layers and (b) SEM image of deposited Cu_2O, (b) J-V plot of the FTO/Cu_2O/TiO_2 photocathodes, reproduced from ref [22].

2.3.1.2. CuO

Cupric oxide (CuO) is another p-type copper oxide with an indirect band gap of 1.2-1.8 eV [19,20], where its small band gap allows CuO to achieve more photocurrent than Cu_2O. However, CuO as a photocathode for water splitting has received less attention than Cu_2O, due to its conduction band being more positive than that of the Cu_2O.[21–23] However, recent studies on hydrogen evolution by CuO with composite photocatalysts, confirm the possibility of CuO to reduce water to hydrogen.[24–27] Like Cu_2O, photocorrosion is another major drawback of using CuO as photocathode in water splitting, although some recent studies show that a reduction in photocorrosion of Cu_2O may apply to CuO.[27–29]

2.3.1.3. NiO

Nickel oxide (NiO) is a semi-transparent p-type semiconductor with a direct band gap of 3.6-4.0 eV.[30] This wide bandgap NiO possess low resistance, high p-type concentration, high hole mobility, and low lattice mismatch with ZnO, which are favourable for the formation of p-n heterojunction.[30–33] On the other hand, the

photocurrents obtained by NiO photocathode are low due to low potential of its valence band (0.3V vs SCE).[34] However, sensitizing NiO photocathodes with quantum dots (e.g., CdSe) possess high photocurrent and photopotential as shown in Figure 5a and 5b.[33,35]

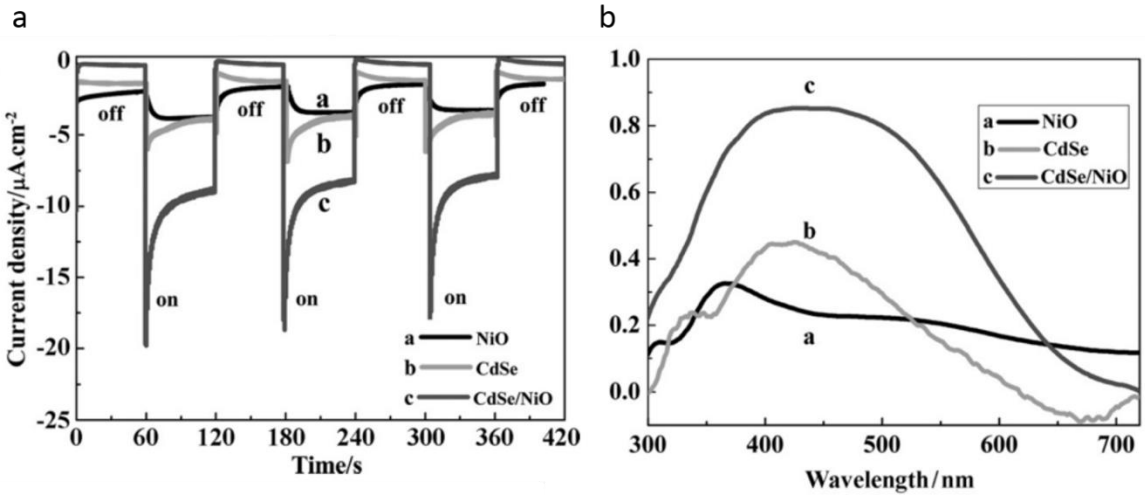

Figure 5: (a) Photocurrent response of NiO/CdSe/CdSe:NiO electrodes under dark and visible light. (b) UV/Vis absorption spectra of NiO/CdSe/CdSe:NiO electrodes; Reproduced from ref [38].

2.3.2 Bimetallic

2.3.2.1. $CuFeO_2$

$CuFeO_2$ has an ABO_2-type semiconductor delafossite structure with a bandgap of 1.5eV, which can absorb the most of visible light.[36] In addition to its small band gap, $CuFeO_2$ is an earth abundant material with high onset potential and good stability in aqueous solution.[36,37] However, poor charge transfer, limit its performance for PEC water splitting. Recent studies show that the fabrication techniques, involving post-treatment in the air with hybrid microwave annealing, enhanced the activity of the electrode which makes the $CuFeO_2$ attractive candidate for PEC water splitting as shown in Figure 6a.[38] In Figure 6b and 6c,

photocurrent activity of $CuFeO_2$ possess enhancement after modifying with electrocatalyst such as nickel-iron (NiFe) and reduced graphene oxide (RGO).[38]

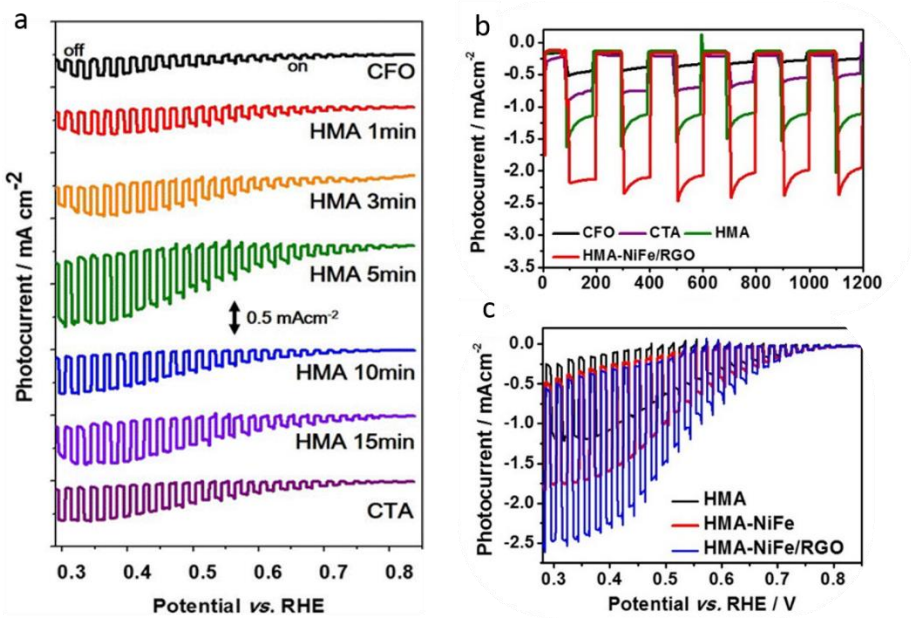

Figure 6: (a) J-V plot of untreated $CuFeO_2$ electrode (CFO) and post treated at different annealing time with using hybrid microwave annealing (HMA) comparing to the conventional thermal annealing (CTA). (b) chronoamperemetry of $CuFeO_2$ treated with CTA, HMA, and and HMA-NiFe/RGO. (c) J-V plot of HMA, HMA-NiFe, and HMA-NiFe/RGO simulated in 1 sun irradiation in 1 M NaOH electrolyte; Reproduced from ref [38].

2.3.2.2. $LaFeO_3$

Perovskite oxides are quite encouraging materials for PEC water splitting due to their high efficiency and stability in water. $LaFeO_3$ with ABO_3 perovskite structure is a promising candidate to be used for water splitting due to its high stability, optoelectronic properties and small band gap energy.[39–42] However, failure to improve their photoresponse limit their use as photocathode which is because of the lack of preparative technique for $LaFeO_3$ photocathode with effective quality.[42] Recent effort show that the efficiency of $LaFeO_3$ as photocathode can

be improved via doping with metals which have 2^+ oxidation state similar to that of Fe^{3+}, such as Mg^{2+} and Zn^{2+}. These dopant agents lead to change the structure and electrical properties of the photocathode which enhanced the overall photoelectrochemical response of $LaFeO_3$ (Figure 7a and 7b).[43]

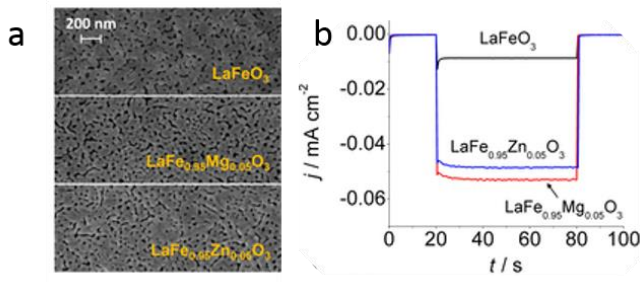

Figure 7: (a) FE-SEM images of pristine $LaFeO_3$ comparing to doped $LaFeO_3$ electrodes. (b) Photocurrent transients for pristine $LaFeO_3$, Mg, and Zn doped $LaFeO_3$ electrodes at -0.25 V; Reproduced from ref [47].

2.3.2.3. $CaFe_2O_4$

Calcium iron Oxide ($CaFe_2O_4$) has been discovered for the first time as a p-type semiconductor oxide for use of electrolyse of water.[44] It has a bandgap of 1.9 eV with suitable conduction and valence band edges of -0.6 and +1.3 V vs NHE, respectively, which is suitable for splitting water.[45] However, the photoresponse of $CaFe_2O_4$ is relatively low, because of its poor charge separation and charge carrier mobility.[46,47] Moreover, $CaFe_2O_4$ photocathode with metal doping such as CuO and Au shows a higher photocurrent response due to the increase absorption wavelength range.[48] Furthermore, $CaFe_2O_4$ doped with Ag exhibited 23 times higher photocurrent response than undoped $CaFe_2O_4$ as shown in Figure 8.[49]

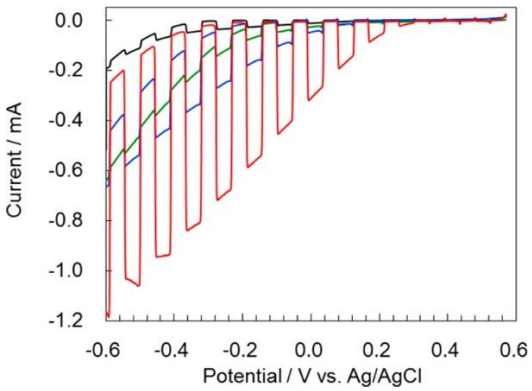

Figure 8: J-V curves for the; Ag- $CaFe_2O_4$ (red line), Cuo- $CaFe_2O_4$ (blue line), Au- $CaFe_2O_4$ (green line), and undoped $CaFe_2O_4$ (black line); Reproduced from ref [53].

2.3.3 Chalcogenides

To date, some p-type chalcogenides have been studied as a photocathode for solar water splitting. Semiconductors with chalcopyrite structure (e.g. $CuInS_2$, $CuGaS_2$), have recently shown significant photocathode performance for solar water splitting due to their excellent photovoltaic properties.

2.3.3.1. $CuInS_2$

Copper indium disulphide ($CuInS_2$) is considered as a promising candidate to be used in thin film solar cells due to its direct bandgap (1.5 eV) and large absorption coefficient (10^5 cm^{-1}) in the visible spectral range.[50–52] Moreover, it is environmentally friendly [52], but the fabrication of $CuInS_2$ thin film is expensive. Fabrication techniques such as chemical deposition, especially spray pyrolysis possess an attraction solution to this issue where the large area of the thin film can easily be coated.[53] Spray pyrolysis at low temperature (about 150-200 ^oC) shows the possibility of the $CuInS_2$ thin film on cheap and flexible substrates.[53]

2.3.3.2. $CuGaS_2$

Copper gallium disulphide ($CuGaS_2$) is less interesting to be used as photocathode in the solar cell than $CuInS_2$ due to its wide direct band gap of 2.4 eV.[54] However, $CuGaS_2$ has a conduction band located at more negative potential than that of $CuInS_2$ which make it a possible photocathode for solar water splitting.[17,55,56] In addition to its wide band gap, gallium deposition requires more cathodic potential than that of indium metal, where the fabrication of uniform film remain is challenging.[17] Recent studies suggested that doping $CuGaS_2$ film with co-catalyst such as Zn and Ti enhanced the morphology and phase structure of Cu-Ga photocathode film (Figure 9).[57]

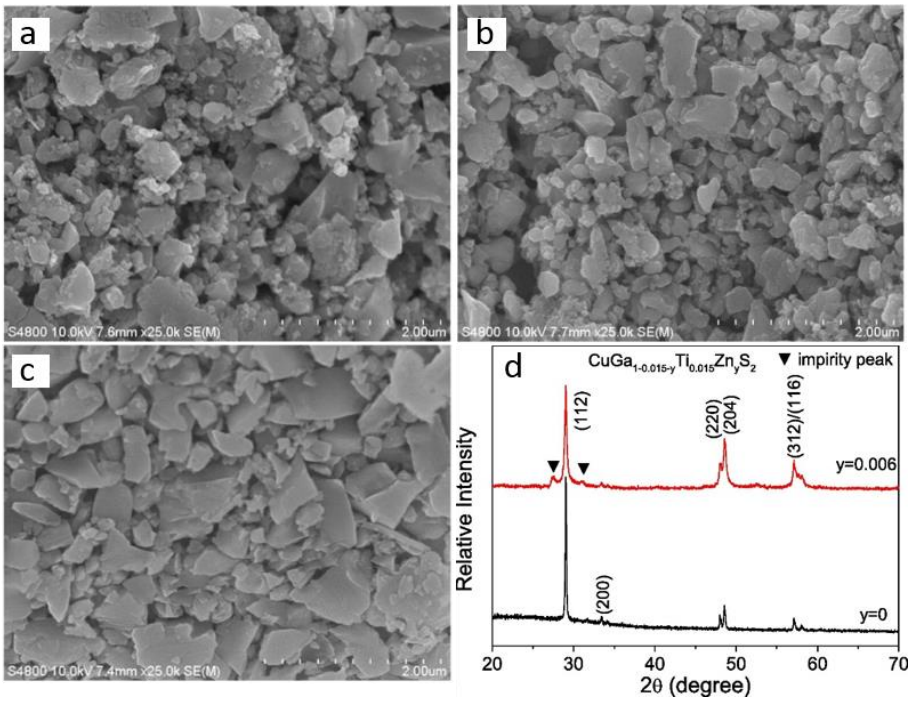

Figure 9: (a) The SEM images of $CuGaS_2$, (b) doped with Ti, (c) doped with Ti and Zn, (d) XRD patterns of pristine $CuGaS_2$ before and after doping. Reproduced from ref [61].

2.3.4 III-V Semiconductors

2.3.4.1. GaP

Gallium phosphide (GaP) has an indirect band gap (2.2-2.3 eV) and band edges above the reduction potential of hydrogen which makes it a suitable material for water splitting.[58,59] The n-type of GaP is unstable in water, but the p-type form has more stability for long periods of time in electrolytes under cathodic conditions.[58] Despite the wide bandgap of GaP, still, it does not show the expected photocurrent.[60,61] Recent investigation shows that the influence of the interface structure region between the semiconductor and the electrolyte, depositing of platinum particles on top of GaP notable increased the efficiency of the photoelectrochemical cell.[59]

2.3.4.2. InP

Indium phosphide (InP) has a direct band gap of 1.35 eV, which makes it well-matched to the solar spectrum.[62–65] Moreover, its conduction band edge is slightly above the water reduction potential.[65] For these reasons, InP is considered a promising photocathode for water splitting. Although p-type InP is suffering from photocorrosion in acidic solution [66,67], the stability and efficiency of InP electrode can be enhanced with protective coat-layer of TiO_2.[68] Despite its efficiency, high cost of bulk materials and fabrication process of InP photocathode limits its scalable application.[68] Latest studies demonstrated a low-cost and high-efficiency solar device, implemented using the thin-film vapour−liquid−solid (TF-VLS) growth technique that decreases usage of feedstock materials.[69]

2.3.5. Silicon

Silicon (Si) has been extensively used for water reduction over the past few decades due to its narrow band gap (1.1 eV)[70,71] In addition to its small band gap energy, silicon is one of the most promising materials for photoelectrodes in a photoelectrochemical water splitting due to its natural abundance, environmentally friendly and ability for large-scale production.[72–74] The practical use of Si as photocathode electrode in water splitting was originally limited due to its instability in water.[71] However, several approaches have been developed to protect its surface from corrosion using protective layers (e.g., ALD of TiO_2,Al_2O_3 , and different catalysts layers) to enable more stable PEC performances of Si electrodes in different aqueous environments.[66,75–79] The latest study indicated that Si photocathode deposited with strontium titanate, $SrTiO_3$ (STO), as protective layer achieved photocurrent density of (35 mA cm^{-2}) and long-term stability as illustrated in Figure 10.[73]

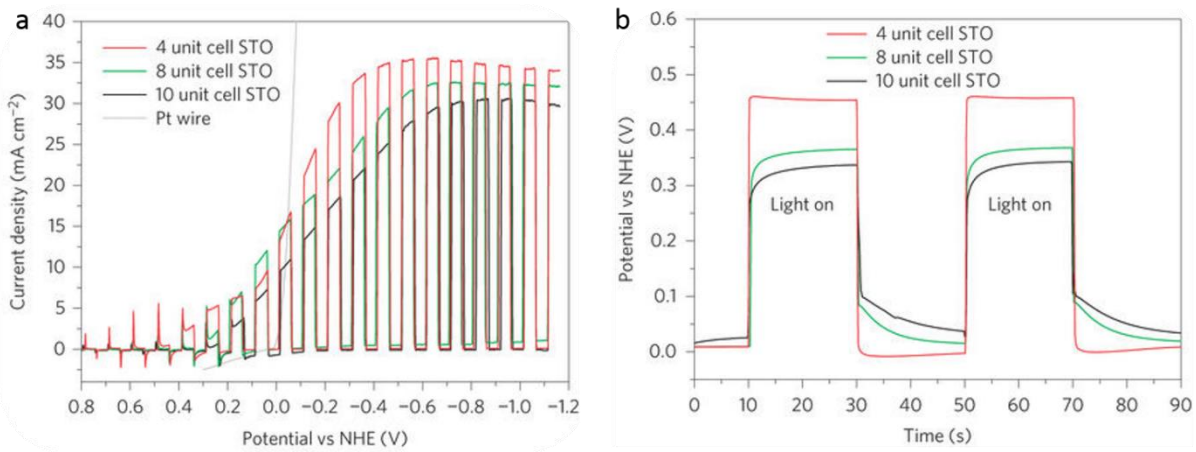

Figure 10: (a) current-voltage curve of Si coated with various STO thicknesses as protective layer. (b) Voltage versus time curve. Reproduced from ref [77].

2.4. Photoanode for Water Splitting

Photoanode materials, responsible for oxygen evolution must be; an n-type semiconductor, band gap that are suitable for absorbing a wide range of the spectrum, and efficient charge collection and charge carriers' mobilities. In addition to that, the materials must be stable in aqueous solution, low cost, and environmentally friendly. This section will focus on the n-type semiconductors that have been investigated as a photoanodic electrode in PEC water splitting. They include monometallic, bimetallic oxides, chalcogenide, and nitride.

2.4.1. Monometallic

2.4.1.1. TiO_2

Titanium dioxide (TiO_2), which is an n-type semiconductor having a bandgap of ~3.2 eV, is considered to be the most promising oxides used in photoelectrochemical water splitting.[80–83] It's reported for the first PEC water splitting as photoanode under UV irradiation by Honda and Fujishima in 1972.[7] Due to its excellent stability in aqueous solution, it has been implemented as protection layers for photoelectrodes (e.g., Cu_2O,Si, InP, etc.) that are not stable in water.[68,77,78] However, the applications of TiO_2 photoanode in PEC water splitting is limited due to its wide band gap. Several techniques have been explored to improve the light absorption and charge carrier transport of TiO_2 such as doping with cocatalyst (e.g., Co and Ag) (Figure 11). For example, N- modified TiO_2 photoanode, which were synthesized via the nitridation of hydrothermally synthesized TiO_2 nanowire arrays in the NH_3 atmosphere, obtained a band gap of 2.4 eV.[84] Additionally, TiO_2 nanotubes treated with heat and chemical reduction demonstrated enhanced photocatalytic activity, with a photocurrent of 2.0 mA at 1.23 V.[85]

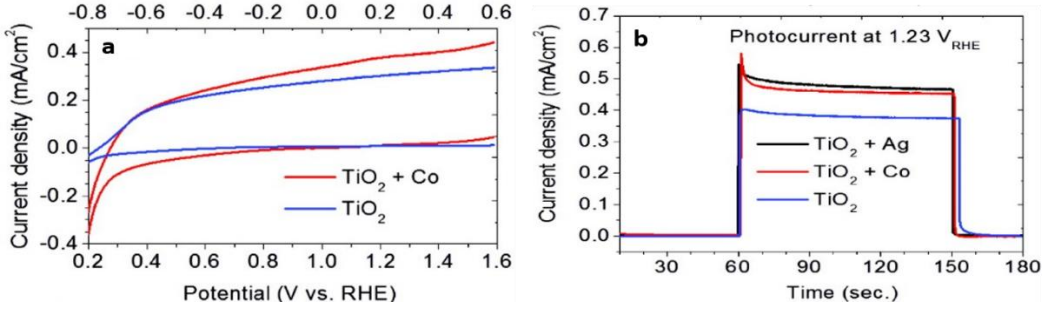

Figure 11: (a) Linear sweep voltammetry of, TiO_2 nanowire arrays (blue), Cobalt doped TiO_2. (b) chronoamperometry measurement of TiO_2 nanowire arrays and the same film after treated with cobalt and silver. Reproduced from ref [88].

2.4.1.2. ZnO

Zinc oxide (ZnO) is also an n-type semiconductor which is environmentally friendly and inexpensive.[86–88] It has a bandgap of 3.2 eV, similar to TiO_2 but higher carrier mobility.[87–92] Nevertheless, the effective applications of ZnO as photoanodes for water splitting still requires the improved design and synthesis technique to overcome the limitations of ZnO.[93] Recent studies revealed that by controlling the morphology of ZnO, the light harvesting ability can be enhanced. Figure 12a and 12b shows that thermal evaporation approaches can also enhance the morphology of ZnO and a photocurrent of ~0.4mA/cm^2 at the applied potential of 0.8$V_{Ag/AgCl}$ is achieved.[93,94]

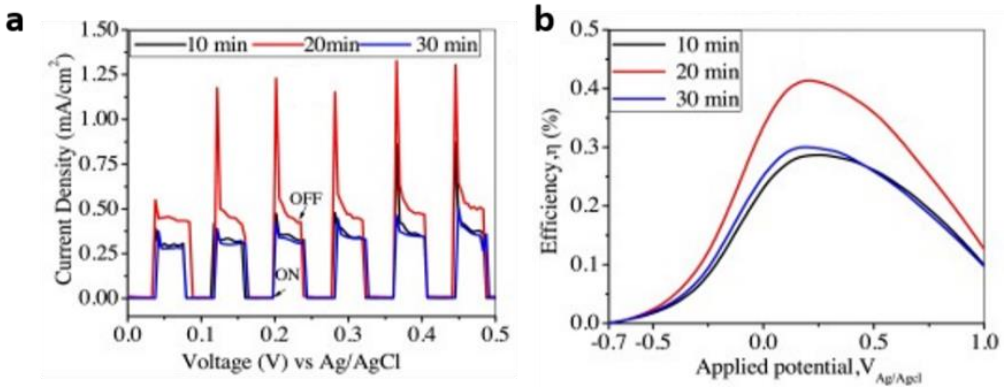

Figure 12: (a) Photocurrent response of ZnO photoanode at different deposition time, (b) Solar to hydrogen conversion efficiency with respect to applied voltage; Reproduced from ref [98].

2.4.1.3. WO_3

Tungsten oxide (WO_3), an n-type semiconductor has been well studied as photoanodes for water splitting compared to their other metal oxides. It has an indirect band gap of 2.5-2.8 eV which can harvest about 12% of the solar spectrum.[95] WO_3 is an inexpensive, nontoxic, and possess high stability in acidic aqueous solution.[95–97] However, this material can only absorb a limited portion of visible light due to its wide band gap.[95] Moreover, its conduction band is too low (0.3V vs RHE) comparing to Hydrogen evolution reaction redox potential.[98] Recent studies have demonstrated that morphological control and hydrothermal treatment can significantly affect the morphology of the synthesized electrode and may exhibit a far higher enhancing photocurrent of WO_3.[99,100] In particular, it was shown that fabricated WO_3 nanospheres by removing the top platelets of WO_3 via a hydrothermal method exhibited a photocurrent of 2.6 $mAcm^{-2}$ at 1.2V as presented in Figure 13.[100]

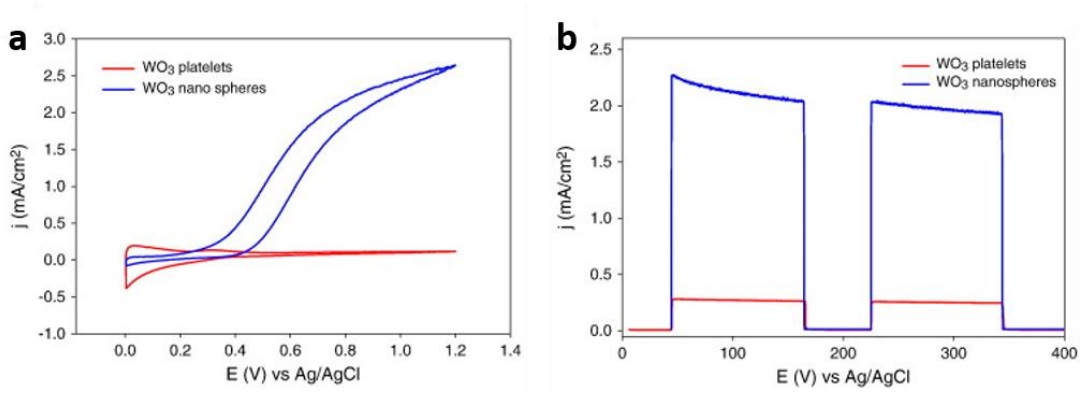

Figure 13: (a) Cyclic voltammograms measurements comparing the photocurrent of WO_3 plates and the resulting nanospheres, (b) photocurrent of WO_3 plates treated by hydrothermal and WO_3 nanospheres under 1.0V applied potentials; Reproduced from ref [104].

2.4.1.4. α-Fe_2O_3

Alpha-Hematite (α-Fe_2O_3) is undoubtedly the most extensively studied n-type semiconductor to be used in water splitting. It has a bandgap of 2.0-2.2 eV which absorb a significant portion of visible light with efficiency exceeds 12%.[13,101–103] It is also stable in most of the aqueous media and has high resistance towards photocorrosion.[13,104,105] In addition, it is environmentally friendly and inexpensive but it has low absorption efficiency, low electrical conductivity, short diffusion length (2-4 nm), and facile surface recombination are serious challenges for its use in practical application as a photoanode.[106] To overcome these limitations, several synthesis techniques and strategies have been developed, which include surface modification and composition.[104,107,108] Surface modification with catalysts such as IrO_2, aims to reduce the overpotential and thus enhanced the efficiency [109,110], while composition aims to increase charge mobility.[110] Recent study reported that preparing α-Fe_2O_3 film by electrodeposition method followed by surface decorating with Co-Pi catalyst showed a stable photocurrent of ~ 1.89 mA cm^{-2} as presented in Figure 14.[111]

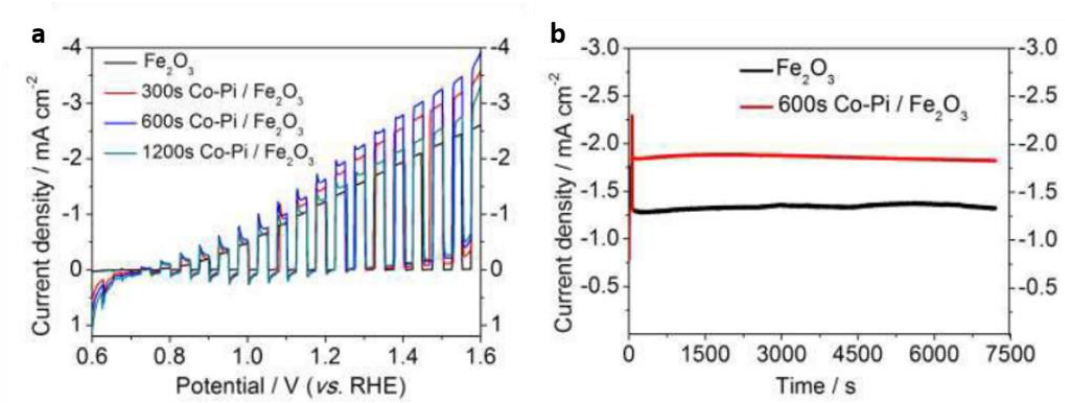

Figure 14: (a) J-V measurements with chopped light for Co-Pi / α-Fe_2O_3 films at different deposition times (300s, 600s, and 1200s). (b) Photocurrent versus time curve of α-Fe_2O_3 and 600s Co-Pi / α-Fe_2O_3 photoanode; Reproduced from ref [115].

2.4.2. Bimetallic

2.4.2.1. $BiVO_4$

Another n-type semiconductor is Bismuth vanadate ($BiVO_4$), which is recently emerged as a viable candidate for photocatalytic water splitting. It has a band gap of 2.4 eV and can absorb a significant portion of the visible spectrum.[112,113] It has a suitable conduction band position very near to the H_2 evolution potential and relatively low onset potential for O_2 evolution.[114,115] However, $BiVO_4$ lacks low photocurrent efficiency under solar radiation, fast electron-hole recombination, slow charge transfer and low water oxidation kinetics.[116–118] To overcome these drawbacks, several techniques have been applied such as the construction of heterojunction structures, morphology control, and doping. Previous works have demonstrated that $WO_3/BiVO_4$ heterojunction possess photocurrent less than 1.0 mA cm^2 at 1.0 V vs RHE.[119,120]

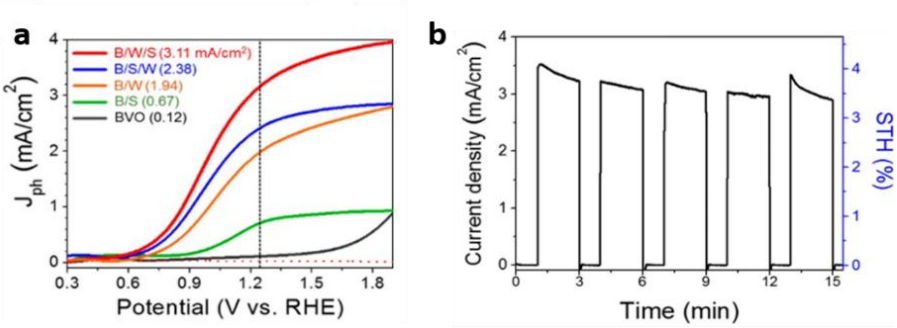

Figure 15: (a) *J-V* curves of five photoanodes (i.e., BVO= $BiVO_4$, B/W = $BiVO_4/WO_3$, B/S= $BiVO_4$/ SnO_2, B/S/W = $BiVO_4$/ SnO_2/WO_3, B/W/S = $BiVO_4/WO_3$ /SnO2). (b) Photocurrent density and solar to hydrogen conversion efficiency as a function of time for the $BiVO_4/WO_3$ / SnO_2 photoanode tandem cell ; Reproduced from ref [121].

A significant enhancement has been achieved using a double-heterojunction photoanode based on $BiVO_4/WO_3$ /SnO_2 triple layers prepared by spin coating (Figure 15), which has an increased the PEC photocurrent to 3.1 mA cm^{-2} at 1.23V vs RHE.[121]

2.4.2.2. $CuWO_4$

Copper tungstate, also known as copper tungsten oxide ($CuWO_4$) is an n-type semiconductor with indirect optical band gap of 2.3 eV.[122–124] It has been widely studied for different applications such as a detector, lasers, and optical sensor.[123–125] Due to its small band gap, it is very close to the ideal potential for PEC water spiting as promising photoanode material.[124,126] In addition, the single crystal of this materials have a maximum conversion efficiency of 0.52%.[123] The PEC of $CuWO_4$ is significantly low due to its low absorption light and high bulk charge transfer resistance.[126–129] Several approaches such as surface modification and construction of heterojunction structures can help to mitigate some of its PEC water splitting limitations. Recent studies demonstrated that modification of the $CuWO_4$ photoanode surface with TiO_2-coated Au NPs can significantly increase the PEC water-splitting performance and increased the water splitting photocurrent from 0.03 to 0.1 mA cm^{-2} (Figure 16).[130] Coupling $CuWO_4$ with WO_3, to form heterojunction photoanode can enhance the absorbed photon density and charge mobility.[131,132]

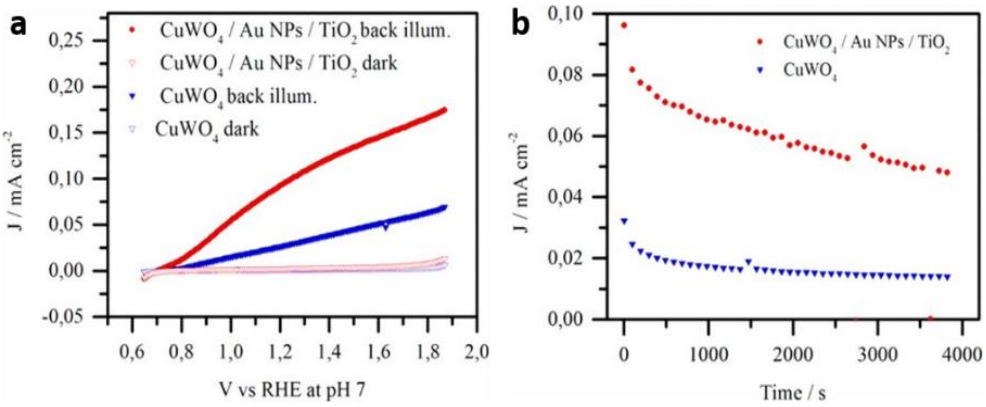

Figure 16: (a) Photocurrent versus voltage (J-V) curve of Current vs time curve for $CuWO_4$ electrode before and after decorating with TiO_2-coated Au NPs. (b) Photocurrent versus time curves at 1.23 V vs RHE under AM 1.5 irradiation; Reproduced from ref 134.

2.4.3. Nitride

2.4.3.1. TaON

Tantalum oxynitride (TaON) with a bandgap of 2.5 eV is another n-type semiconductor, suitable for solar water splitting.[133–135] It has achieved a maximum quantum efficiency of 34 %.[136] Moreover, TaON shows reasonably alignment of its CB and VB edges relative to the OH^-/O_2 oxidation and $H+/H_2$ reduction potentials, generate H_2 and O_2.[133] However, the activities for H_2 production is lower than those for O_2 evolution, which is sufficiently negative for H_2 production.[137] TaON suffer from low stability due to the introduction of N 2p orbitals in the valence band.[133] Recent studies have demonstrated that the photocatalytic activity of TaON for water splitting can be enhanced through photo-deposition with noble nanoparticles such as Ru.[138] Also, a significant enhancement to the photocurrent in TaON photoanode by heat treatment of the surface with $TiCl_4$ has been reported (Figure 17).[139]

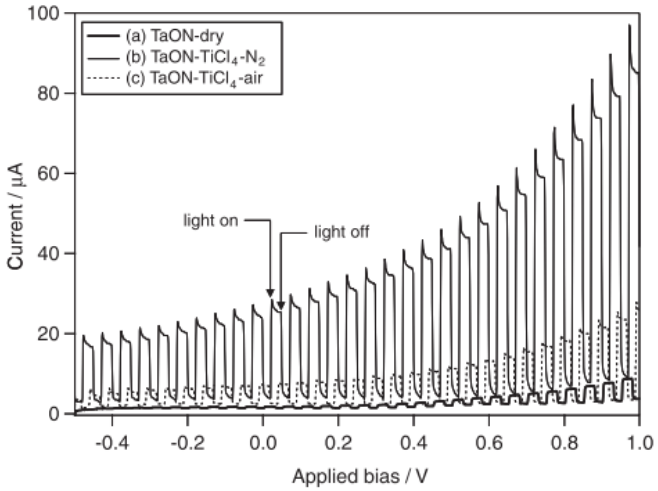

Figure 17: Current–bias dependence over the TaON electrodes before and after the $TiCl_4$ treatment under chopped visible light irradiation; Reproduced from ref [143].

2.4.3.2. Ta_3N_5

Tantalum nitride (Ta_3N_5) has received significant attention over the past years due to its small band gap (2.1 eV) and stability.[135,140–143] It has CB lies at ca.-0.4V vs. NHE, and VB lies at ca. +1.6V vs. NHE, which possibly allow Ta_3N_5 to perform unassisted solar water splitting.[140,144] Due to these band energies, Ta_3N_5 can theoretically split water spontaneously as a single photoanode with maximum solar to hydrogen efficiency of about ~15 %.[144–146] However, Ta_3N_5 suffer from the poor charge transport, low photocurrent efficiency and insufficient light absorption.[147–149] Effective strategies have been developed to enhance the PEC performance of Ta_3N_5 photoanode, such as nanostructuring and morphology control.[150,151] Particularly, Ta_3N_5 photoanode with a 1D configuration, such as nanotubes (NTs), nanorods (NRs), has been considerably investigated.[147,148,152–156] These 1D nanostructure offer advances of charge transfer to the solid-liquid interface without recombination and high absorption of incident light. Ta_3N_5 nanorod arrays modified by $Co(OH)_x$ co-catalyst yields a stable photocurrent density of 2.8 mA cm^{-2} at 1.23 V vs RHE as illustrated in Figure 18.[153]

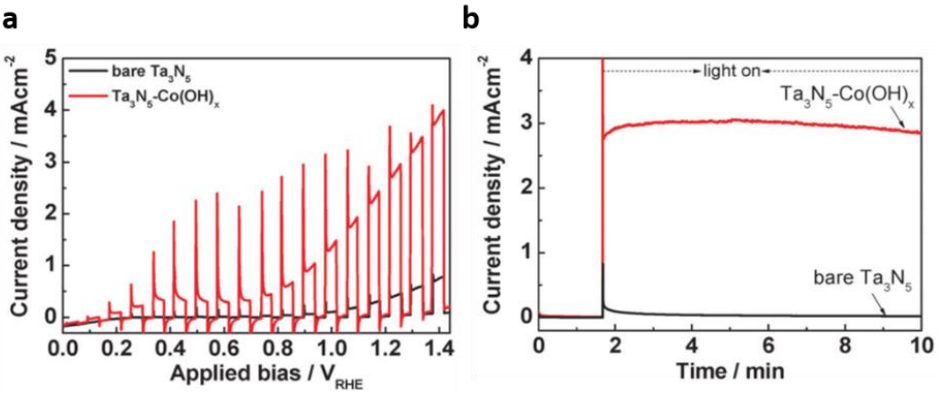

Figure 18: (a) Photocurrent vs applied potential bias curve of Ta_3N_5 photoanode before and after loading of the Co $(OH)_x$ co-catalyst. (b) Photocurrent vs time (j-t) curve; Reproduced from ref [157].

2.4.4. Chalcogenides

2.4.4.1. CdS

Cadmium sulphide (CdS) is the most investigated metal chalcogenide materials for water splitting under visible light irradiation due to its favourable direct band gap (2.4eV). Furthermore, its band edge positions are suitable for water splitting to produce hydrogen and oxygen.[157,158] Despite these advantages, the photocurrent activity of CdS is not sufficient due to the photogenerated charges (electrons and holes) which cannot be efficiently separated and transferred.[158–160] Additionally, CdS suffer from photocorrosion in aqueous media which hampers their long-term stability in solar water splitting.[157,161] To overcome these drawbacks, extensive studies have been investigated to improve the stability and efficiency of CdS photoanode. Recent studies demonstrated that the formation of CdS 2D-nanostructuers offer significant advantages such as, reduction of the scattering rate which increase the carrier collection efficiency and increase the absorption of incident light (Figure 19).[162]

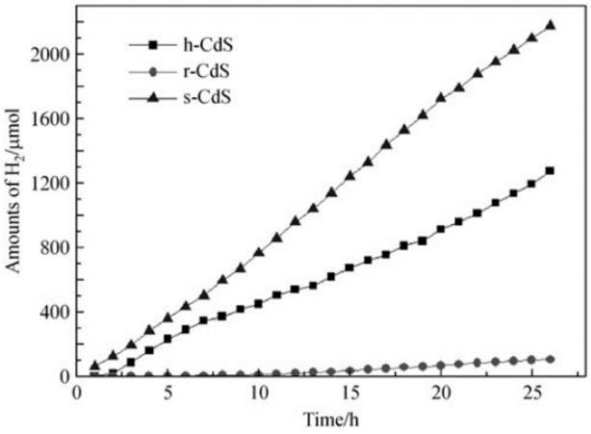

Figure 19: Hydrogen evolution activity of different CdS nanostructured; solid nanospheres (s-CdS), (b) hollow nanospheres (h-CdS), and (c) nanorods (r-CdS); Reproduced from ref [166].

2.4.4.2. ZnS

Zinc sulphide (ZnS) is a promising candidate for photocatalysis of hydrogen production due to its ability, generation of mobile photoexcited charge carriers, and high conduction band potential which ensures fast electron transfer.[163–166] Moreover, it has active sites for hydrogen evolution without the need to deposit expensive charge transfer co-catalyst like Pt or RuO_2.[167] But due to its large band gap (≈3.6 eV), the performance in photocatalysis is limited, which means that pure ZnS are only active under UV irradiation.[168,169] Therefore, several studies have been investigated to improve the light absorption behaviour of ZnS photoanode. For instance, it has been reported that doping ZnS with transition metal ions such as Ni, Sn, and Cu has improved the H_2 production under visible light irradiation.[170–172] An alternative approach to doping is the defect engineering, which also increases the overall efficiency of ZnS.[173] Moreover, the modification of the fabrication conditions can lead to defect states in ZnS thin films which also enhance visible-light absorption, charge separation, and photocurrent up to 1.6 mA/cm^2 as shown in Figure 20.[173]

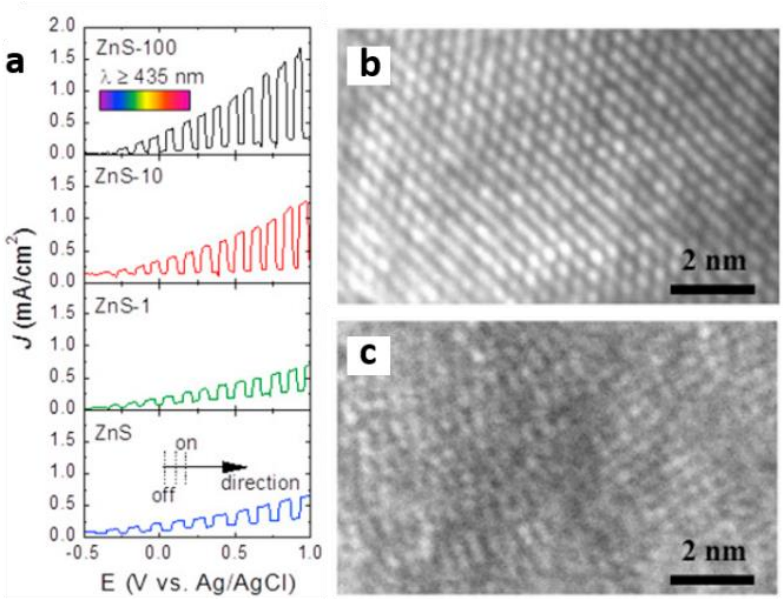

Figure 20: (a) J-V curves for from bulk ZnS, ZnS-1, ZnS-10, and ZnS-100. (b) And (c) TEM images showing the atomic structure of ZnS and ZnS-100 respectively. ZnS-xx labels indicate the N2 gas pressure (in mTorr) used during the deposition. Reproduced from ref [177].

2.5. Current State of The Art for Water Splitting

2.5.1. Tandem Approach

Photoelectrochemical water splitting (PEC) is considered a promising technology to convert solar energy into storable and transportable fuel. Potential energy greater than 1.23 eV should be sufficient to split water. However, the actual required energy is considerably greater due to the different kinetic and thermodynamic non-idealities in the oxidation and reduction reactions. Therefore, using a single semiconductor absorber requires a semiconductor with large energy bandgap to absorb a maximum portion of the solar spectrum.[174] This drawback, can be solved by dual-absorber-four photon (D4) tandem approach (Figure 21).[175]

In PEC tandem device, the cell configuration is composed of two-sided light absorption electrodes, a p-type photoanode and an n-type photocathode, where

hydrogen evolution (water oxidization) and oxygen reduction (water reduction) reactions take place on the photocathode and photoanode, respectively.[175]

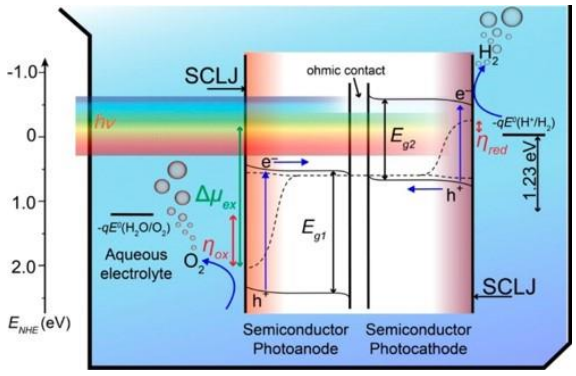

Figure 21: Schematic diagram of PEC water splitting approach using a dual-absorber tandem cell; Reproduced from ref [179].

The Tandem cell has an improved overall efficiency due to the two different band gaps used and the high portion of the light absorbed. It shows a theoretical estimated light conversion efficiency of 18%.[176] Tandem cell used a III–V semiconducting materials have been shown to perform with efficiencies of 12.4% under concentrated sunlight.[177] Though, their commercial applications still far to achieve due to poor stability, high cost and complexity of their fabrication.[178] To reduce the cost, increase stability, and enhanced the efficiency, several methods have been proposed.[175,179–184] Recently, Graetzel et al. reported a perovskite tandem solar cell based on $CH_3NH_3PbI_3$ and achieved solar-to-hydrogen efficiency of 12.3%.[185]

2.5.2. PEC/PV Approach

Due to the difficulties in designing PEC tandem cell with sufficient bandgap energies and band edge positions of photocathodes and photoanodes; photovoltaic-integrated photoelectrochemical cells are an attractive approach for mitigating this aspect. In this configuration, the bandgap energy levels in PEC

cells have no role with the water redox due to PV cells could play the direct role of potential supply; therefore, there are no limitations on selecting the material type (Figure 22).[180] PV-PEC systems possess many advantages for water splitting compared with PEC systems, excluding major cost. PV-PEC device has been developed for the first time for hydrogen production via water splitting in 1998, using a $GaInP_2$/GaAs tandem cell which has achieved more than 10 % efficiency.[177]

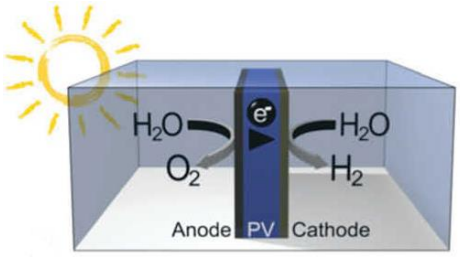

Figure 22: Photovoltaic-integrated photoelectrochemical cells,
Reproduced from ref [190].

Moreover, coupling a WO_3/$BiVO_4$ photoanode with a double junction GaAs/InGaAsP solar cell, to build a self-operating integrated PEC device, generated solar to hydrogen efficiency of up to 8.1%.[114] The highest efficiency of PV-PEC approach was recently achieved through the fabrication of an integrated system with Ni electrodes and multi-junction GaInP/GaAs/Ge solar cell, delivered solar water splitting efficiency of about 22.4%.[186] Despite this high efficiency, the fabrication of PV-PEC solar cells is complicated and expensive. Without considering the cost factor, PV-PEC systems are the most viable hydrogen production method for practical applications. PV-PEC system based hydrogen production is expected to be primarily used in navigation, military, and aerospace applications to provide fuel for these special situations.

2.6. Photocatalytic for Dye Degradation

2.6.1. Mechanism of Photocatalytic Dye Degradation

The term ‘‘photocatalytic degradation’’ involves photogenerated photons and a catalyst. Under light irradiation, the photoelectron is excited from the filled valence band to the empty conduction of a photocatalyst. This process leaves behind a hole in the valence band. The photogenerated holes then react with water to produce $OH^{\cdot}$ radical as shown in Eq.(4),

$$H_2O + h^+(VB) \longrightarrow OH^{\cdot} + H^+ \qquad (4)$$

The formed $OH^{\cdot}$ radical on the semiconductor surface is a very powerful oxidizing agent. It can attack adsorbed organic molecules that are close to the catalyst surface causing them to mineralize to an extent according to their structure and stability level.[187] Moreover, It can also attack microorganisms for their enhanced decontamination.[188]

2.6.2. Nanomaterials for Photocatalytic Dye Degradation

The use of nanomaterials in photocatalytic dye degradation was initially considered after the discovery of the phenomenon of a photocatalytic water splitting on a TiO_2 electrode under UV irradiation by Honda and Fujishima in 1972[7]. In particular, TiO_2 shows excellent performance for photocatalytically breaking down organic compounds. For example, suspend a catalytically active TiO_2 powder into a shallow pool of polluted water and allows it to be illuminated with sunlight, the water will gradually become purified.[189] Since then, semiconductor photocatalysts have attracted considerable attention due to its promising applications in water purification.

The ideal photocatalyst should be stable, non-toxic, inexpensive and, of course, highly photoactive. Other primary criteria for the degradation of organic compounds are that the redox potential of the $H_2O/^{\bullet}OH$ couple

($OH^- \rightarrow {}^{\bullet}OH + e^-$; $E^0 = -2.8$ V) should lies within the bandgap of the semiconductor.[190] Several semiconductors (e.g., TiO_2, ZnO, SnO_2, In_2O_3, WO_3, and CdS) can act as photocatalysts for photocatalytic degradation of organic compounds because of their unique electronic structure and sufficient bandgap energies.[191–194] Most researchers have earlier used these photocatalysts in a nanoparticles powder form dispersed in industrial water for the photodegradation of organic pollutants. Nanoparticle powders are particularly effective since their small size allow them to readily mix with the contaminated solution and have a high surface area. However, low recovery of the nanoparticles is challenging, which makes their use in these applications potentially cost-prohibitive.[195] Moreover, there is a possible leaking of photocatalyst powder into the environment. In order to overcome these problems, an alternative technique is used where the photocatalyst is presented as a thin film on a solid substrate.[195] The thin film structured based nanomaterials appears to have lots of potential in photocatalytic applications. It can solve the recyclability and tedious treatment issues of powder photocatalysts.

2.6.2.1. TiO_2

Among the various photocatalytic materials, the titanium dioxide (TiO_2) has been extensively studied as a semiconductor photocatalyst due to its physical and chemical properties such as stability, chemical inertness, lower cost, strong oxidizing power, high photosensitivity, resistance to corrosion, and nontoxicity.[196–199] Due to its wide band gap (3.2 eV) ,the titanium dioxide thin film

has been intensively employed for several applications including photocatalytic degradation of organic compounds such as methylene blue[200,201], phenol[202], rhodamine B [202], and methyl orange.[202] However, TiO_2 can only be activated by UV light (λ<400nm) which limit its application in environmental remediation.

2.6.2.2. ZnO

Zinc oxide (ZnO) is a wide band gap semiconductor (3.2 eV) with attractive properties including high transparency in the visible wavelength, a high piezoelectric constant, a large electro-optic coefficient and a large exciton binding energy (~ 60 meV) at room temperature.[203] Several studies have recently focused on ZnO materials because of their potential applications in solar cells, gas sensors, and piezoelectric.[204,205] Moreover, ZnO has been widely investigated as one of the most representative photocatalysts for degrading of organic compounds.[205] Many researchers have been employed ZnO thin film in photocatalytic degradation of organic dyes such as methylene blue [206,207], rhodamine B[208], and methyl orange[209]. However, photo-corrosion is a major concern for ZnO thin films which could limit their use in environmental remediation.

2.7. Literature Review Concluding Remarks

This literature review has investigates the basic principles, mechanism, materials and most current methods of photoelectrochemical water splitting for solar fuel production and for photocatalytic dye degradation. Many semiconducting materials have been investigated for photoelectrochemical water splitting and photocatalytic water treatments. However, to perform high-efficiency solar water splitting and photocatalytic dye degradation, it is necessary for the materials used to satisfy three conditions. They should have an appropriate

bandgap energy, a suitable position of the bandgap, and chemical stability. In order to induce the water decomposition reaction, the conduction band (CB) and valence band (VB) above the water reduction level and below the oxidation level of water. At present, most materials did not fulfil these requirements for water splitting. Some materials such as sulphide face a stability issue which limits their use in hydrogen generation. Moreover, with nanoparticle powders, there are issues of recollection and their toxicity to the environments may hinder their use in the photocatalytic application. The need to design highly efficient materials that can generate hydrogen is of vital importance. Also, there is a need to design and develop a stable and visible light absorbing materials for photocatalytic application. The summary of this literature review can be outlined in the following points;

- PCs system is limited by recyclability and toxicity issues.
- PECs required stable semiconductors materials.
- More research is done on n-type materials as photoanodes.
- P-type stable photocathodes are not much investigated.
- There is a potential to use metal ferrites as suitable materials for hydrogen generation and dye degradation.

2.8. References

(1) Tachibana, Y.; Vayssieres, L.; Durrant, J. R. *Nat. Photonics* **2012**, *6* (8), 511.

(2) Cogdell, R. J.; Brotosudarmo, T. H. P.; Gardiner, a T.; Sanchez, P. M.; Cronin, L. *Biofuels* **2010**, *1* (6), 861.

(3) Osterloh, F. E.; Parkinson, B. A. *Mrs Bull.* **2011**, *36* (1), 17.

(4) Walter, M. G.; Warren, E. L.; McKone, J. R.; Boettcher, S. W.; Mi, Q.; Santori, E. a.; Lewis, N. S. *Chem. Rev.* **2010**, *110* (11), 6446.

(5) Chen, X.; Shen, S.; Guo, L.; Mao, S. S. *Chem. Rev.* **2010**, *110*, 6503.

(6) Li, R. *Chin. J. Catal.* **2017**, *38*, 5.

(7) Fujishima, a; Honda, K. *Nature.* **1972**, *238*, 37.

(8) Navarro, R. M.; Alvarez-Galván, M. C.; Villoria de la Mano, J. a.; Al-Zahrani, S. M.; Fierro, J. L. G. *Energy Environ. Sci.* **2010**, *3*, 1865.

(9) Abe, R. *J. Photochem. Photobiol. C Photochem. Rev.* **2010**, *11* (4), 179.

(10) Hunter, B. M.; Gray, H. B.; Muller, A. M. *Chem. Rev.* **2016**, *116*, 14120.

(11) Osterloh, F. E.; Parkinson, B. A. *MRS Bull.* **2011**, *36*, 17.

(12) P.J. Boddy, J. *Electrochem. Soc.* Electrochem. Soc 1968, p 199.

(13) Sivula, K.; Le Formal, F.; Grätzel, M. *ChemSusChem.* **2011**, *4* (4), 432.

(14) Kumar, P. *Orient. J. Chem.* **2016**, *32* (3), 1473.

(15) Hara, M.; Kondo, T.; Komoda, M.; Ikeda, S.; Shinohara, K.; Tanaka, A.; Kondo, J. N.; Domen, K.; Hara, M.; Shinohara, K.; Tanaka, A. *Chem. Commun.* **1998**, No. 3, 357.

(16) de Jongh, P. E.; Vanmaekelbergh, D.; Kelly, J. J. *Chem. Commun.* **1999**, No. 12, 1069.

(17) Kang, D.; Kim, T. W.; Kubota, S. R.; Cardiel, A. C.; Cha, H. G.; Choi, K. S. *Chem. Rev.* **2015**, *115*, 12839.

(18) Paracchino, A.; Laporte, V.; Sivula, K.; Grätzel, M.; Thimsen, E. *Nat. Mater.* **2011**, *10*, 456.

(19) Chiang, C. Y.; Shin, Y.; Aroh, K.; Ehrman, S. *Int. J. Hydrog. Energy.* **2012**, *37*, 8232.

(20) Chiang, C.-Y.; Aroh, K.; Franson, N.; Satsangi, V. R.; Dass, S.; Ehrman, S. H. *Int. J. Hydrog. Energy.* **2012**, *36*, 15519.

(21) Chauhan, D.; Satsangi, V. R.; Dass, S.; Shrivastav, R. *Bulletin of Materials Science*. 2006, pp 709–716.

(22) Koffyberg, F. P.; Benko, F. A. *J. Appl. Phys.* **1982**, *53* (2), 1173.

(23) Hsu, Y.-K.; Yu, C.-H.; Lin, H.-H.; Chen, Y.-C.; Lin, Y.-G. *J. Electroanal. Chem.* **2013**, *704*, 19.

(24) Xu, S.; Ng, J.; Du, A. J.; Liu, J.; Sun, D. D. *Int. J. Hydrog. Energy.* **2011**, *36* (11), 6560.

(25) Zhang, L.; Liu, Y. N.; Zhou, M.; Yan, J. *Appl. Surf. Sci.* **2013**, *282*, 531.

(26) Jin, Z.; Li, P.; Liu, G.; Zheng, B.; Yuan, H.; Xiao, D. *J. Mater. Chem. A.* 2013, pp 14736–14743.

(27) Barreca, D.; Fornasiero, P.; Gasparotto, A.; Gombac, V.; Maccato, C.; Montini, T.; Tondello, E. *ChemSusChem.* **2009**, *2* (3), 230.

(28) Hang, N. K.; Kadir, H. A.; Minggu, L. J.; Kassim, M. Bin. *Mater. Sci. Forum.* **2013**, *756*, 219.

(29) Emin, S.; Abdi, F. F.; Fanetti, M.; Peng, W.; Smith, W.; Sivula, K.; Dam, B.; Valant, M. *J. Electroanal. Chem.* **2014**, *717–718*, 243.

(30) Gupta, R. K.; Ghosh, K.; Kahol, P. K. *Phys. E.* **2009**, *41*, 617.

(31) Wang, J. Y.; Lee, C. Y.; Chen, Y. T.; Chen, C. T.; Chen, Y. L.; Lin, C. F.; Chen, Y. F. *Appl. Phys. Lett.* **2009**, *95* (13), 131117.

(32) Zhang, Z.; Shao, C.; Li, X.; Wang, C.; Zhang, M.; Liu, Y. *ACS appl.mater .interfaces.* **2010**, *2* (10), 2915.

(33) Hu, C.; Chu, K.; Zhao, Y.; Teoh, W. Y. *ACS appl.mater .interfaces.* **2014**, *6*, 18558.

(34) Dong, Y.; Chen, Y.; Jiang, P.; Wang, G.; Wu, X.; Wu, R.; Zhang, C. *Chem. Asian J.* **2015**, *10*, 1660.

(35) Barceló, I.; Guillén, E.; Lana-villarreal, T.; Gómez, R.; Universitari, I. *J. Phys. Chem. C.* **2013**, *117*, 22509.

(36) Read, C. G.; Park, Y.; Choi, K.-S. *J. Phys. Chem. Lett.* **2012**, *3*, 1872.

(37) Oh, Y.; Yang, W.; Kim, J.; Jeong, S.; Moon, J. *ACS Appl.Mater.Interfaces.* **2017**, *9*, 14078.

(38) Jang, Y. J.; Park, Y. Bin; Kim, H. E.; Choi, Y. H.; Choi, S. H.; Lee, J. S. *Chem. Matter.* **2016**, *28*, 6054.

(39) Milanova, M.; Zaharieva, J.; Todorovska, R.; Todorovsky, D. *Thin Solid Film.* **2014**, *562*, 43.

(40) Tang, P.; Tong, Y.; Chen, H.; Cao, F.; Pan, G. *Curr.Appl.Phys.* **2013**, *13*, 340.

(41) Parida, K. M.; Reddy, K. H.; Martha, S.; Das, D. P.; Biswal, N. *Int. J. Hydrog. Energy.* **2010**, *35* (22), 12161.

(42) Yu, Q.; Meng, X.; Wang, T.; Li, P.; Liu, L.; Chang, K.; Liu, G.; Ye, J. *Chem. Commun.* **2015**, *51*, 3630.

(43) Díez-García, M. I.; Gómez, R. *ChemSusChem.* **2017**, *10*, 1.

(44) Matsumoto, Y.; Omae, M.; Sugiyama, K.; Sato, E. *J. Phys. Chem.* **1987**, *91*, 577.

(45) Ida, S.; Yamada, K.; Matsunaga, T.; Hagiwara, H.; Matsumoto, Y.; Ishihara, T. *J. Am. Chem. Soc.* **2010**, *132* (49), 17343.

(46) Kim, E. S.; Nishimura, N.; Magesh, G.; Kim, J. Y.; Jang, J. W.; Jun, H.; Kubota, J.; Domen, K.; Lee, J. S. *J. Am. Chem. Soc.* **2013**, *135*, 5375.

(47) Wang, G.; Ling, Y.; Wang, H.; Xihong, L.; Li, Y. *Photochem. Photobiol. C.* **2014**, *19* (1), 35.

(48) Huang, Q.; Ye, Z.; Xiao, X. *J. Mater. Chem. A.* **2015**, *3*, 15824.

(49) K.Sekizawa, T.Nonaka, T.Arai, and T. M. *ACS Appl.Mater.Interfaces.* **2014**, *6*, 10969.

(50) Klaer, J.; Bruns, J.; Henninger, R.; Siemer, K.; Klenk, R.; Ellmer, K.; Bräunig, D. *Semicond. Sci. Technol.* **1998**, *13*, 1456.

(51) Bihri, H.; Messaoudi, C.; Sayah, D.; Abd-Lefdil, M.; Cadéne, M. *Thin Solid Film.* **1999**, *338*, 125.

(52) Yuan, J.; Shao, C.; Zheng, L.; Fan, M.; Lu, H.; Hao, C.; Tao, D. *Vacuum.* **2014**, *99*, 196.

(53) Fischereder, A.; Rath, T.; Haas, W.; Amenitsch, H.; Schenk, D.; Zankel, A.; Saf, R.; Hofer, F.; Trimmel, G. *ACS appl.mater .interfaces.* **2012**, *4*, 382.

(54) Kaga, H.; Kudo, A. *J. Catal.* **2014**, *310*, 31.

(55) Quintans, C. S.; Kato, H.; Kobayashi, M.; Kaga, H.; Iwase, A.; Kudo, A.; Kakihana, M. *J. Mater. Chem. A.* **2015**, *3*, 14239.

(56) Iwase, A.; Ng, Y. H.; Amal, R.; Kudo, A. *J. Mater. Chem. A.* **2015**, *3*, 8566.

(57) Li, Q.; Wu, J.; Wang, Y.; Fan, W.; Zhu, J.; Wang, X.; Yang, Y. *Mater. Lett.* **2018**, *210*, 70.

(58) Memming, R.; Schwandt, G. *Electrochim. Acta.* **1968**, *13*, 1299.

(59) Ziegler, J.; Fertig, D.; Kaiser, B.; Jaegermann, W.; Blug, M.; Hoch, S.; Busse, J. *Energy Procedia.* **2012**, *22*, 108.

(60) Aspnes, D. E.; Studna, A. A. *Phys. Rev. B Condens. Matter.* **1983**, *27* (2), 985.

(61) Yoneyama, H.; Shiota, H.; Tamura, H. *J. Electroanal. Chem.* **1983**, *159*, 361.

(62) Heller, A.; Miller, B.; Lewerenz, H. J.; Bachmann, K. J. *J. Am. Chem. Soc.* **1980**, *102* (21), 6555.

(63) Aharon-Shalom, E.; Heller, A. *J. Electrochem. Soc.* **1982**, *129* (12), 2865.

(64) Szklarczykt, M.; Bockris, J. O. M. *J. Phys. Chem.* **1984**, *88* (22), 5241.

(65) Lee, M. H.; Takei, K.; Zhang, J.; Kapadia, R.; Zheng, M.; Chen, Y. Z.; Nah, J.; Matthews, T. S.; Chueh, Y. L.; Ager, J. W.; Javey, A. *Angew. Chem. Int. Ed.* **2012**, *51*, 10760.

(66) Moriya, M.; Minegishi, T.; Kumagai, H.; Katayama, M.; Kubota, J.; Domen, K. *J. Am. Chem. Soc.* **2013**, *135*, 3733.

(67) Marsen, B.; Cole, B.; Miller, E. L. *Sol. Energy Mater. Sol. Cells.* **2008**, *92*

(9), 1054.

(68) Lin, Y.; Kapadia, R.; Yang, J.; Zheng, M.; Chen, K.; Hettick, M.; Yin, X.; Battaglia, C.; Sharp, I. D.; Ager, J. W.; Javey, A. *J. Phys. Chem. C.* **2015**, *119*, 2308.

(69) Hettick, M.; Zheng, M.; Lin, Y.; Sutter-Fella, C. M.; Ager, J. W.; Javey, A. *J. Phys. Chem. Lett.* **2015**, *6*, 2177.

(70) Candea, R. M.; Kastner, M.; Goodman, R.; Hickok, N. *J. Appl. Phys.* **1976**, *47* (6), 2724.

(71) Stephen, R. G.; Riley, F. L. *J. Eur. Ceram. Soc.* **1989**, *5*, 219.

(72) Reece, S. Y.; Hamel, J. A.; Sung, K.; Jarvi, T. D.; Esswein, A. J.; Pijpers, J. J. H.; Nocera, D. G. *Science.* **2011**, *334* (6056), 645.

(73) Ji, L.; McDaniel, M. D.; Wang, S.; Posadas, A. B.; Li, X.; Huang, H.; Lee, J. C.; Demkov, A. A.; Bard, A. J.; Ekerdt, J. G.; Yu, E. T. *Nat Nanotechnol.* **2015**, *10*, 84.

(74) Sun, K.; Shen, S.; Liang, Y.; Burrows, P. E.; Mao, S. S.; Wang, D. *Chem. Rev.* **2014**, *114*, 8662.

(75) Ran, J.; Zhang, J.; Yu, J.; Jaroniec, M.; Qiao, S. Z. *Chem Soc Rev.* **2014**, *43*, 7787.

(76) Shen, L.; He, C.; Qiu, J.; Lee, S. M.; Kalita, A.; Cronin, S. B.; Stoykovich, M. P.; Yoon, J. *ACS appl.mater .interfaces.* **2015**, *7*, 26043.

(77) Seger, B.; Tilley, D. S.; Pedersen, T.; Vesborg, P. C. K.; Hansen, O.; Grätzel, M.; Chorkendorff, I. *RSC Adv.* **2013**, *3*, 2590225907.

(78) Seger, B.; Pedersen, T.; Laursen, A. B.; Vesborg, P. C. K.; Hansen, O.; Chorkendorff, I. *J. Am. Chem. Soc.* **2013**, *135*, 1057.

(79) Bao, X. Q.; Liu, L. *J. Power Sources.* **2014**, *268*, 677.

(80) Ni, M.; Leung, M. K. H.; Leung, D. Y. C.; Sumathy, K. *Renew Sustain Energy Rev.* **2007**, *11* (3), 401.

(81) Roy, P.; Berger, S.; Schmuki, P. *Angew. Chem. Int. Ed.* **2011**, *50* (13), 2904.

(82) Lee, K.; Mazare, A.; Schmuki, P. *Chem. Rev.* **2014**, *114*, 9385.

(83) Tian, J.; Zhao, Z.; Kumar, A.; Boughton, R. I.; Liu, H. *Chem. Soc. Rev.* **2014**, *43*, 6920.

(84) Hoang, S.; Guo, S.; Hahn, N. T.; Bard, A. J.; Mullins, C. B. *Nano Lett.* **2012**, *12*, 26.

(85) Cho, I. S.; Choi, J.; Zhang, K.; Kim, S. J.; Jeong, M. J.; Cai, L.; Park, T.; Zheng, X.; Park, J. H. *Nano Lett.* **2015**, *15*, 5709.

(86) Jarup, L. *Br. Med. Bull.* **2003**, *68* (1), 167.

(87) Kolodziejczak-Radzimska, A.; Jesionowski, T. *Materials (Basel).* **2014**, *7* (4), 2833.

(88) Djurišić, A. B.; Chen, X.; Leung, Y. H.; Man Ching Ng, A. *J. Mater. Chem.*

2012, *22* (14), 6526.

(89) Özgür, Ü.; Alivov, Y. I.; Liu, C.; Teke, A.; Reshchikov, M. A.; Doğan, S.; Avrutin, V.; Cho, S. J.; Morkoç, H. *J. Appl. Phys.* **2005**, *98* (4), 1.

(90) Tang, H.; Prasad, K.; Sanjinès, R.; Schmid, P. E.; Lévy, F. *J. Appl. Phys.* **1994**, *75* (4), 2042.

(91) Wang, Z. L. *J. Phys. Condens. Matter* **2004**, *16* (25), R829.

(92) Chandiran, A. K.; Abdi-Jalebi, M.; Nazeeruddin, M. K.; Grätzel, M. *ACS Nano* **2014**, *8* (3), 2261.

(93) Hamid, S. B. A.; Teh, S. J.; Lai, C. W. *Catalysts.* **2017**, *7*, 93.

(94) Islam, M. S.; Hossain, M. F.; Razzak, S. M. A. *J. Photochem. Photobiol.* **2016**, *326*, 100.

(95) Liu, X.; Wang, F.; Wang, Q. *Phys. Chem. Chem. Phys.* **2012**, *14*, 7894.

(96) Iwai, T. *J. Phys. Soc. Jpn.* 1960, pp 1596–1600.

(97) Butler, M. A. *J. Appl. Phys.* **1977**, *48* (5), 1914.

(98) Desilvestro, J.; Grätzel, M. *J. Electroanal. Chem.* **1987**, *238*, 129.

(99) Amano, F.; Tian, M.; Wu, G.; Ohtani, B.; Chen, A. *ACS appl.mater .interfaces.* **2011**, *3*, 4047.

(100) Thind, S. S.; Tian, M.; Chen, A. *Electrochem. Commun.* **2014**, *43*, 13.

(101) Bak, T.; Nowotny, J.; Rekas, M.; Sorrell, C. C. *Int. J. Hydrog. Energy.* **2002**, *27*, 991.

(102) van de Krol, R.; Liang, Y.; Schoonman, J. *J. Mater. Chem.* **2008**, *18* (20), 2311.

(103) Li, J.; Wu, N. *Catal. Sci. Technol.* **2015**, *5*, 1360.

(104) Dotan, H.; Sivula, K.; Grätzel, M.; Rothschild, A.; Warren, S. C. *Energy Environ. Sci.* **2011**, *4* (3), 958.

(105) Katz, M. J.; Riha, S. C.; Jeong, N. C.; Martinson, A. B. F.; Farha, O. K.; Hupp, J. T. *Coord. Chem. Rev.* **2012**, *256*, 2521.

(106) Chen, S.; Thind, S. S.; Chen, A. *Electrochem. Commun.* **2016**, *63*, 10.

(107) Dare-Edwards, M. P.; Goodenough, J. B.; Hamnett, A.; Trevellick, P. R. *J. Chem. Soc., Faraday Trans.* **1983**, *79* (9), 2027.

(108) Hamann, T. W. *Dalt. Trans.* **2012**, *41*, 7830.

(109) Kay, A.; Cesar, I.; Grätzel, M. *J. Am. Chem. Soc.* **2006**, *128* (49), 15714.

(110) Malara, F.; Minguzzi, A.; Marelli, M.; Morandi, S.; Psaro, R.; Dal Santo, V.; Naldoni, A. *ACS Catal.* **2015**, *5*, 5292.

(111) Zeng, Q.; Bai, J.; Li, J.; Xia, L.; Huang, K.; Li, X.; Zhou, B. *J. Mater. Chem. A* **2015**, *3*, 4345.

(112) Park, Y.; McDonald, K. J.; Choi, K.-S. *Chem. Soc. Rev.* **2013**, *42*, 2321.

(113) Kudo, A.; Omori, K.; Kato, H. *J. Am. Chem. Soc.* **1999**, *121* (49), 11459.

(114) Pihosh, Y.; Turkevych, I.; Mawatari, K.; Uemura, J.; Kazoe, Y.; Kosar, S.; Makita, K.; Sugaya, T.; Matsui, T.; Fujita, D.; Tosa, M.; Kondo, M.; Kitamori, T. *Sci. Rep.* **2015**, *5*, 11141.

(115) Abdi, F. F.; Han, L.; Smets, A. H. M.; Zeman, M.; Dam, B.; van de Krol, R. *Nat. Commun.* **2013**, *4*, 1.

(116) Huang, Z.-F.; Pan, L.; Zou, J.-J.; Zhang, X.; Wang, L. *Nanoscale.* **2014**, *6*, 14044.

(117) Wu, Q.; Voorhis, T. Van; Nocera, D. G.; Nocera, D. G.; Bansal, A.; Turner, J. A.; Kapur, M.; Kainthla, R. C.; Bockris, J. O. M.; Turner, J. A.; Miller, E. L.; Misra, A.; Gibson, T. L.; Kelly, N. A.; Gau, S. C.; Murphy, O. J.; Kapur, M.; Bockris, J. O. M.; Nocera, D. G.; Kanan, M. W.; Nocera, D. G.; Surendranath, Y.; Nocera, D. G.; Dinc, M.; Nocera, D. G.; Surendranath, Y.; Reece, S. Y.; Nocera, D. G.; Gascon, J. A.; Mcevoy, J. P.; Brudvig, G. W.; Batista, V. S.; Kawakami, K.; Kamiya, N.; Surendranath, Y.; Lutterman, D. A.; Nocera, D. G.; Choi, K. S.; Choi, K. S.; Sun, J.; Inumaru, H.; Gamelin, D. R.; Gamelin, D. R.; Cornuz, M.; Sivula, K.; Gamelin, D. R.; Schiff, E. A.; Luque, A.; Hegedus, S.; Survey, U. S. G. *Science.* **2014**, *343*, 990.

(118) Chen, Y. S.; Manser, J. S.; Kamat, P. V. *J. Am. Chem. Soc.* **2015**, *137*, 974.

(119) Su, J.; Guo, L.; Bao, N.; Grimes, C. a. *Nano Lett.* **2011**, *11*, 1928.

(120) Hong, S. J.; Lee, S.; Jang, J. S.; Lee, J. S. *Energy Environ. Sci.* **2011**, *4*, 1781.

(121) Baek, J. H.; Kim, B. J.; Han, G. S.; Hwang, S. W.; Kim, D. R.; Cho, I. S.; Jung, H. S. *ACS appl.mater .interfaces.* **2017**, *9*, 1479.

(122) Benko, F. A.; MacLaurin, C. L.; Koffyberg, F. P. *Mater. Res. Bull.* **1982**, *17* (1), 133.

(123) S K Arora, T. M. and N. M. B. *J. Phys. D Appl. Phys.* **1990**, *23*, 460.

(124) Chang, Y.; Braun, A.; Deangelis, A.; Kaneshiro, J.; Gaillard, N. *J. Phys. Chem. C.* **2011**, *115*, 25490.

(125) Ume, V. O. I. *Phys. Rev.* **1959**, *113* (3), 801.

(126) Yourey, J. E.; Bartlett, B. M. *J. Mater. Chem.* **2011**, *21*, 7651.

(127) Pandey, P. K.; Bhave, N. S.; Kharat, R. B. *Mater. Lett.* **2005**, *59*, 3149.

(128) Gaillard, N.; Chang, Y.; Deangelis, A.; Higgins, S.; Braun, A. *Int. J. Hydrog. Energy.* **2013**, *38*, 3166.

(129) Yourey, J. E. J.; Pyper, K. J. K.; Kurtz, J. B.; Bartlett, B. M. *J. Phys. Chem. C* **2013**, *117*, 8708.

(130) Valenti, M.; Dolat, D.; Biskos, G.; Schmidt-Ott, A.; Smith, W. A. *J. Phys. Chem. C.* **2015**, *119*, 2096.

(131) Zhan, F.; Xie, R.; Li, W.; Li, J.; Yang, Y.; Li, Y.; Chen, Q. *Int. J. Hydrog.*

Energy. **2015**, *40*, 6512.

(132) Yourey, J. E.; Kurtz, J. B.; Bartlett, B. M. *J. Phys. Chem. C.* **2012**, *116*, 3200.

(133) Higashi, M.; Domen, K.; Abe, R. *J. Am. Chem. Soc.* **2012**, *134*, 6968.

(134) Abe, R.; Higashi, M.; Domen, K. *J. Am. Chem. Soc.* **2010**, *132*, 11828.

(135) Higashi, M.; Domen, K.; Abe, R. *Energy Environ. Sci.* **2011**, *4*, 4138.

(136) Hitoki, G.; Takata, T.; Kondo, J. N.; Hara, M.; Kobayashi, H.; Domen, K. *Chem. Commun.* **2002**, *2* (16), 1698.

(137) Maeda, K.; Domen, K. *J. Phys. Chem.* **2007**, *111* (22), 7851.

(138) Hara, M.; Nunoshige, J.; Takata, T.; Kondo, J. N.; Domen, K. *Chem. Commun.* **2003**, No. 24, 3000.

(139) Abe, R.; Takata, T.; Sugihara, H.; Domen, K. *Chem. Lett.* **2005**, *34* (8), 1162.

(140) Yokoyama, D.; Hashiguchi, H.; Maeda, K.; Minegishi, T.; Takata, T.; Abe, R.; Kubota, J.; Domen, K. *Thin Solid Film.* **2011**, *519*, 2087.

(141) Hara, M.; Chiba, E.; Ishikawa, A.; Takata, T.; Kondo, J. N.; Domen, K. *J. Phys. Chem.* **2003**, *107*, 13441.

(142) Hara, M.; Hitoki, G.; Takata, T.; Kondo, J. N.; Kobayashi, H.; Domen, K. *Catal. Today.* **2003**, *78*, 555.

(143) Kerlau, M.; Merdrignac-Conanec, O.; Guilloux-Viry, M.; Perrin, A. *Solid State Sci.* **2004**, *6*, 101.

(144) Chun, W.; Ishikawa, A.; Fujisawa, H.; Takata, T.; Kondo, J. N.; Hara, M.; Kawai, M.; Matsumoto, Y.; Domen, K. *J. phys. Chem. B.* **2003**, *107*, 1798.

(145) Chen, Z.; Jaramillo, T. F.; Deutsch, T. G.; Kleiman-Shwarsctein, A.; Forman, A. J.; Gaillard, N.; Garland, R.; Takanabe, K.; Heske, C.; Sunkara, M.; McFarland, E. W.; Domen, K.; Miller, E. L.; Turner, J. A.; Dinh, H. N. *J. Mater. Res.* **2010**, *25* (1), 3.

(146) Seitz, L. C.; Chen, Z.; Forman, A. J.; Pinaud, B. A.; Benck, J. D.; Jaramillo, T. F. *ChemSusChem.* **2014**, *7*, 1372.

(147) Pinaud, B. a.; Vesborg, P. C. K.; Jaramillo, T. F. *J. Phys. Chem. C* **2012**, *116*, 15918.

(148) Dabirian, A.; Van De Krol, R. *Chem. Matter.* **2015**, *27*, 708.

(149) Ziani, A.; Nurlaela, E.; Dhawale, D. S.; Silva, D. A.; Alarousu, E.; Mohammed, O. F.; Takanabe, K. *Phys. Chem. Chem. Phys.* **2015**, *17* (4), 2670.

(150) Osterloh, F. E. *Chem. Soc. Rev.* **2013**, *42*, 2294.

(151) Zhang, P.; Zhang, J.; Gong, J. *Chem Soc Rev.* **2014**, *43*, 4395.

(152) Feng, X.; LaTempa, T. J.; Bastiam, J. I.; Mor, G. K.; Varghese, O. K.; Grimes, C. A. *Nano Lett.* **2010**, *10* (3), 948.

(153) Zhen, C.; Wang, L.; Liu, G.; Lu, G. Q. (Max); Cheng, H.-M. *Chem. Commun.* **2013**, *49* (29), 3019.

(154) Hou, J.; Cheng, H.; Takeda, O.; Zhu, H. *Energy Environ. Sci.* **2015**, *8*, 1348.

(155) Wang, L.; Nguyen, N. T.; Zhou, X.; Hwang, I.; Killian, M. S.; Schmuki, P. *ChemSusChem.* **2015**, *8*, 2615.

(156) Zhang, P.; Wang, T.; Zhang, J.; Chang, X.; Gong, J. *Nanoscale.* **2015**, *7*, 13153.

(157) Pareek, A.; Gopalakrishnan, A.; Borse, P. H. *J. Phys. Conf. Ser.* **2016**, *755*, 012006.

(158) Xu, Y.; Zhao, W.; Xu, R.; Shi, Y.; Zhang, B. *Chem. Commun.* **2013**, *49*, 9803.

(159) Pareek, A.; Purbia, R.; Paik, P.; Hebalkar, N. Y.; Kim, H. G.; Borse, P. H. *Int. J. Hydrog. Energy.* **2014**, *39*, 4170.

(160) Pareek, A.; Paik, P.; Borse, P. H. *Langmuir.* **2014**, *30*, 15540.

(161) Kageshima, Y.; Kumagai, H.; Hisatomi, T.; Minegishi, T.; Kubota, J.; Domen, K. *J. Phys. Chem. C.* **2016**, *120*, 10781.

(162) Chen, X.; Shangguan, W. *Front. Energy.* **2013**, *7* (1), 111.

(163) Monroy, E.; Omn s, F.; Calle, F. *Semicond. Sci. Technol.* **2003**, *18*, R33.

(164) Youn, H. C.; Baral, S.; Fendler, J. H. *J. Phys. Chem.* **1988**, *92*, 6320.

(165) Reber, J. F.; Meier, K. *J. Phys. Chem.* **1984**, *88* (24), 5903.

(166) Tran, T.; Park, W.; Tong, W. *J. Appl. Phys.* **1997**, *81* (6), 2803.

(167) Bhatt, M. D.; Lee, J. S. *J. Mater. Chem. A.* **2015**, *3*, 10632.

(168) Chen, Z. G.; Cheng, L.; Xu, H. Y.; Liu, J. Z.; Zou, J.; Sekiguchi, T.; Lu, G. Q.; Cheng, H. M. *Adv. Mater.* **2010**, *22* (21), 2376.

(169) Hu, J.-S.; Ren, L.-L.; Guo, Y.-G.; Liang, H.-P.; Cao, A.-M.; Wan, L.-J.; Bai, C.-L. *Angew. Chem. Int. Ed.* **2005**, *44* (8), 1269.

(170) Mukherjee, A.; Mitra, P. *Mat. Res.* **2017**, *20* (2), 430.

(171) Huang, C. M.; Chen, L. C.; Pan, G. T.; Yang, T. C. K.; Chang, W. S.; Cheng, K. W. *Mater. Chem. Phys.* **2009**, *117*, 156.

(172) Öztaş, M.; Bedir, M.; Necmeddin Yazici, A.; Vural Kafadar, E.; Toktamiş, H. *Phys. B.* **2006**, *381*, 40.

(173) Kurnia, F.; Ng, Y. H.; Amal, R.; Valanoor, N.; Hart, J. N. *Sol. Energy Mater. Sol. Cells.* **2016**, *153*, 179.

(174) Pan, H. *Renew Sustain Energy Rev.* **2016**, *57*, 584.

(175) Sivula, K.; Prevot, M. S. *J. Phys. Chem. C.* **2013**, *117*, 17879.

(176) Fujishima, A.; Honda, K. *Bull. Chem. Soc. Jpn.* 1971, pp 1148–1150.

(177) Khaselev, O.; Turner, J. a. *Science.* **1998**, *280*, 425.

(178) Brillet, J.; Yum, J.-H.; Cornuz, M.; Hisatomi, T.; Solarska, R.; Augustynski, J.; Graetzel, M.; Sivula, K. *Nat. Photonics.* **2012**, *6*, 824.

(179) Warren, S. C.; Voïtchovsky, K.; Dotan, H.; Leroy, C. M.; Cornuz, M.; Stellacci, F.; Hébert, C.; Rothschild, A.; Grätzel, M. *Nat. Mater.* **2013**, *12*, 842.

(180) Zhang, K.; Ma, M.; Li, P.; Wang, D. H.; Park, J. H. *Adv. Energy Mater.* **2016**, *6*, 1600602.

(181) Gurudayal; Sabba, D.; Kumar, M. H.; Wong, L. H.; Barber, J.; Gratzel, M.; Mathews, N. *Nano Lett.* **2015**, *15*, 3833.

(182) Landman, A.; Dotan, H.; Shter, G. E.; Wullenkord, M.; Houaijia, A.; Maljusch, A.; Grader, G. S.; Rothschild, A. *Nat. Mater.* **2017**, *16*, 646.

(183) Shaner, M. R.; Atwater, H. A.; Lewis, N. S.; McFarland, E. W. *Energy Environ. Sci.* **2016**, *9*, 2354.

(184) Weber, M. F. *J. Electrochem. Soc.* **1984**, *131* (6), 1258.

(185) Luo, J.; Im, J.-H.; Mayer, M. T.; Schreier, M.; Nazeeruddin, M. K.; Park, N.-G.; Tilley, S. D.; Fan, H. J.; Gratzel, M. *Science.* **2014**, *345*, 1593.

(186) Bonke, S. A.; Wiechen, M.; Macfarlane, D. R.; Spiccia, L. *Energy Environ. Sci.* **2015**, *8*, 2791.

(187) Chong, M. N.; Jin, B.; Chow, C. W. K.; Saint, C. *Water Res.* **2010**, *44* (10), 2997.

(188) Ajmal, A.; Majeed, I.; Malik, R. N.; Idriss, H.; Nadeem, M. A. *RSC Adv.* **2014**, *4* (70), 37003.

(189) Fujishima, A.; Rao, T. N.; Tryk, D. A. *J. Photochem. Photobiol. C Photochem. Rev.* **2000**, *1* (1), 1.

(190) Beydoun, D.; Amal, R.; Low, G.; McEvoy, S. *J. Nanoparticle Res.* **1999**, *1* (4), 439.

(191) Vinodgopal, K.; Kamat, P. V. *Environ. Sci. Technol.* **1995**, *29* (3), 841.

(192) Lathasree, S.; Rao, A. N.; Sivasankar, B.; Sadasivam, V.; Rengaraj, K. *J. Mol. Catal. A Chem.* **2004**, *223* (1–2), 101.

(193) Kansal, S. K.; Singh, M.; Sud, D. *J. Hazard. Mater.* **2007**, *141* (3), 581.

(194) Sadale, S. B.; Chaqour, S. M.; Gorochov, O.; Neumann-Spallart, M. *Mater. Res. Bull.* **2008**, *43* (6), 1472.

(195) Konstantinou, I. K.; Albanis, T. A. *Appl. Catal. B Environ.* **2004**, *49* (1), 1.

(196) Wang, X.; Yu, J. C.; Ho, C.; Hou, Y.; Fu, X. *Langmuir* **2005**, *21* (6), 2552.

(197) Linsebigler, A. L.; Lu, G.; Yates, J. T. *Chem. Rev.* **1995**, *95* (3), 735.

(198) Hoffmann, M. R.; Martin, S. T.; Choi, W.; Bahnemann, D. W. *Chem. Rev.* **1995**, *95* (1), 69.

(199) Hashimoto, K.; Irie, H.; Fujishima, A. *Jpn. J. Appl. Phys.* **2005**, *44* (12), 8269.

(200) Sangpour, P.; Hashemi…, F. *J. Phys. … VN - readcube.com* **2010**, *2*, 13955.

(201) Yogi, C.; Kojima, K.; Takai, T.; Wada, N. *J. Mater. Sci.* **2009**, *44* (3), 821.

(202) Dumitriu, D.; Bally, A. .; Ballif, C.; Hones, P.; Schmid, P. .; Sanjinés, R.; Lévy, F.; Pârvulescu, V. . *Appl. Catal. B Environ.* **2000**, *25* (2–3), 83.

(203) Wang, L.-L.; Ren, Z.-Q.; Li, Q. *J. Mater. Sci. Mater. Electron.* **2014**, *25* (7), 2992.

(204) Wang, Zhong Lin; Song, J. *Science (80-.).* **2006**, *312* (5771), 242.

(205) Beek, W. J. E.; Wienk, M. M.; Janssen, R. A. J. *Adv. Funct. Mater.* **2006**, *16* (8), 1112.

(206) Velanganni, S.; Manikandan, A.; Prince, J. J.; Mohan, C. N.; Thiruneelakandan, R. *Phys. B Condens. Matter* **2018**, *545* (July), 383.

(207) Shankar, S.; Saroja, M.; Venkatachalam, M.; Parthasarathy, G. **2017**, *03* (01), 180.

(208) Gebreslassie, T. W.; Pattabi, M.; Pattabi, R. M. *Int. J. Sci. Res.* **2015**, *4* (5), 2252.

(209) Mohd Hir, Z.; Abdullah, A.; Zainal, Z.; Lim, H. *Catalysts* **2017**, *7* (11), 313.

Chapter 3: Characterization and Experimental Techniques

This chapter outlines the characterization techniques used for this project. It also discusses in details the theory behind each technique.

3.1. X-Ray Diffraction

X-ray diffraction (XRD) is probably the most essential and widely used technique of characterising crystalline solids materials. XRD can be used to determine the atomic structure of a crystalline material since the wavelength of an X-ray, (~0.1-100 Å), is similar to the interatomic distances in a crystal, allowing crystal structures to diffract X-rays with an angle equal to the angle of incidence.[1] When the X-ray incident upon a sample it can either be transmitted, or it will be scattered by the electrons of the atoms in the material. When two parallel X-rays scatter from two adjacent planes of atoms within the crystal, they can either do so constructively or destructively depending on their phase. Constructive interference occurs when two X-ray waves with phases separated by an integer number of wavelengths add to make a new wave with a larger amplitude, Figure 23.

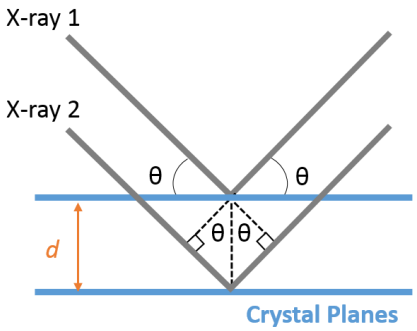

Figure 23: Schematic representation of diffraction of X-ray by crystal (Bragg's Law).

The relationship between the wavelengths of the incident X-rays, the angle of incidence and distance between the crystal lattice planes of atoms is described by Bragg's Law:

$$n\lambda=2d\sin\theta \quad (5)$$

where n order of reflection, λ is the wavelength of the X-ray, d is the distance between the layers and θ is the angle of incidence beam. Since the crystal atoms are arranged in a periodic fashion, the diffracted waves will consist of sharp interference peaks with the same symmetry as in the distribution of crystal atoms. Measuring the diffraction pattern, therefore, allows the determination of the distribution of atoms in a crystal. The main application of XRD is to identify and quantify of different compounds and phases in the sample by search and match it with the extensive databases available.

3.2. Scanning Electron Microscopy

Scanning electron microscopy (SEM) is a technique that uses a focused high electron beam to scan rapidly over the surface of the sample to obtain high-resolution images of the surface. While an optical microscope cannot go beyond the limits of the visible range of the spectrum, since our eyes can only detect photons with wavelengths greater than ≈ 400 nm, a beam of high energy electrons can be produced with lower wavelength compared to that of visible light. The wavelength of the electrons depends on their speed, and this depends on the accelerating voltage applied to them, which is a controllable parameter. Since the optical microscopes have their resolution limited to about 200 nm, most SEMs can go down to 10 nm nowadays.

The principle of scanning electron microscope is that: a beam of electrons is generated by a source into a probe which scans rapidly across the surface of the

sample in raster fashion. The interaction between the sample and the electron probe generates various types of emissions, which are captured by different detectors placed in appropriate position and combined to form images on the computer screen, Figure 24 .[2] Magnetic lens are used to focus the electron beam, resulting in all the electrons converging in a highly focused beam. This process occurs inside a vacuum chamber to avoid any interaction between any particles carried by air and the electrons.

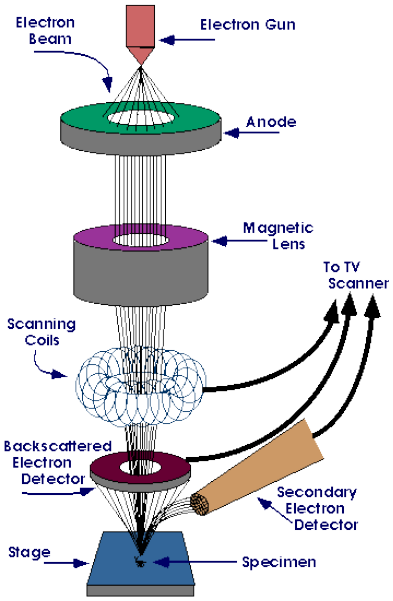

Figure 24: Schematic diagram of the scanning electron microscope (SEM)

3.3. Energy-Dispersive X-Ray Spectroscopy

SEM is often complemented with energy-dispersive X-ray spectroscopy (EDX), which used to identify the elemental composition of the features in the SEM image. This is achieved by detects X-rays emitted from the sample during the bombardment of the sample by an electron beam.[3] When the sample is stricken by SEM electron beam, electron is rejected from the atoms on the sample surface.

The rejected electron leave behind a vacancy which filled by electrons from a higher state and an x-ray is emitted to balance the energy difference between the two electrons states. The EDX detector measures the abundance of emitted x-ray versus their energy. When this emitted x-ray strikes the detector they generate a small current which is converted to a voltage pulse, the size of this proportional to the frequency of the X-rays. The EDX spectrum is plotted as x-ray energy versus counts and is used to determine the elemental composition of the sample.

3.4. Raman Spectroscopy

Raman spectroscopy is a scattering technique and often used as a complementary technique to XRD in the characterisation of the semiconductor. It is based on the inelastic scattering of incident radiation through its interaction with vibrating molecules.[4] When the sample is illuminated with a light from the laser beam, it will interact with the molecules of the sample and generates a scattered light. The scattered light with a frequency different from that of incident light is used to construct a Raman spectrum. Raman spectra arise due to the collision between incident radiation and molecules of the sample. When a monochromatic radiation focused onto the sample, it scatters in all directions after its interaction with sample molecules. The vast majority of this scattered radiation has a frequency which is equal to the frequency of incident radiation and give Rayleigh scattering. Only a small fraction of scattered radiation has a frequency different from the frequency of incident light and give Raman scattering. Finally, when the frequency of incident light higher or lower than the frequency of scattered radiation give the Stokes and anti-Stokes scattering respectively.[5,6]

These variation on the scattered light is depending on the vibration state of the material, Figure 25.

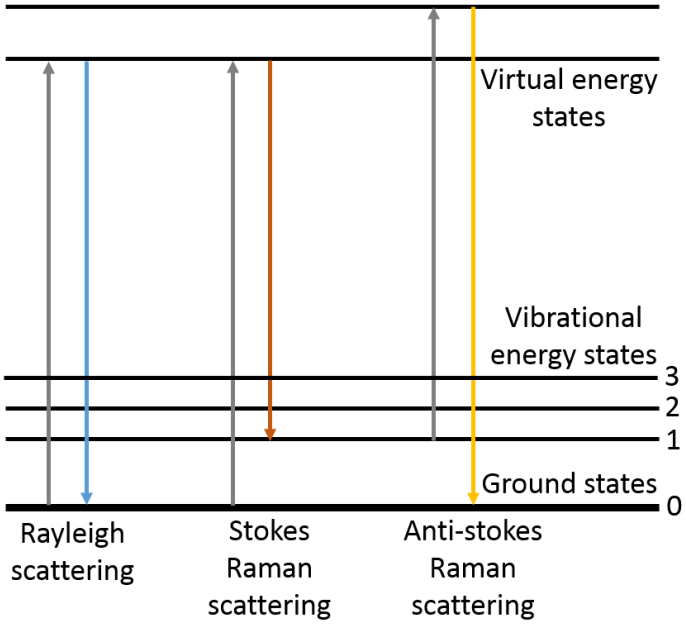

Figure 25: Energy level diagram for Rayleigh, Raman, Stokes and Anti-Stokes scattered light.

Raman spectra can reveal a wide range of information about a material, including the crystal structure type and orientation, dopant concentration etc. Raman bands arise from a change in polarizability during the molecular vibration which means the observed bands arise from specific characteristic molecular vibrations.[5] The changes in energies of these transitions can be plotted as a spectrum, and they can be used to identify the material and provide a "molecular fingerprint" of the material being observed. Raman spectrum is presented as an intensity versus wavelength shift.

3.5. Atomic Force Microscopy

Atomic force microscopy (AFM) is a scanning probe microscope technique to explore the topography of the surface of a material. AFM used to measure the force or potential energy between a small tip attached to the cantilever and a

sample, Figure 26.[7] When the tip attached to the cantilever come close to the surface during with scanning of the sample, Van der Waal forces attract it closer due to the formation of temporal dipoles in the electronic clouds of both the tip and the sample. When the tip touches the surface of the sample, the repulsive coulombic forces overcome the attractive ones and pushing the tip away. This repulsion and attraction effects between the cantilever tip and the sample surface result deflections in the cantilever, which behaves like a spring. This deflection can be calculated by Hook's law;

$$F = -kz \qquad (6)$$

where F is the force, k is the spring's constant and z the cantilever deflection.

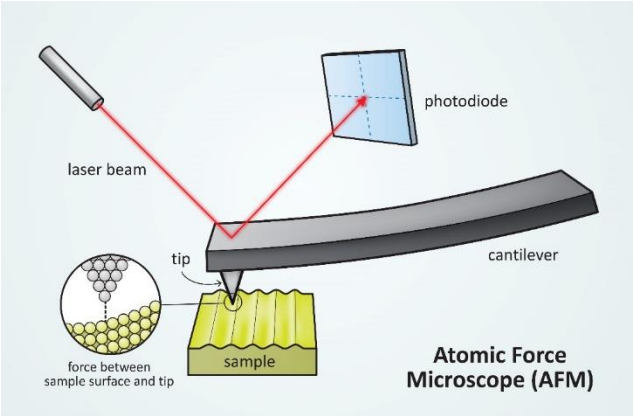

Figure 26: Diagram showing the main components of an atomic force microscope.

AFM enabled to detect hollows and raising features as the cantilever tip moves across the substrate surface, obtaining a topographic map of the sample surface. The detection system is based on a laser beam that is focused onto the back reflective surface of the cantilever: any deflections on the cantilever result in an also subtle change in the direction of the reflected beam, which is collected by a position-sensitive detector. The sample is attached to a holder that is moving in the plane perpendicular to the cantilever, allowing to scan the whole surface of

the sample. The tip of the cantilever is usually made of silicon and it is either pyramidal or tetrahedral in shape. The sharper the tip, the higher the resolution of the AFM image.

3.6. Ultraviolet-Visible Spectroscopy

Ultraviolet and visible (UV-Vis) Spectroscopy is one of the most popular analytical techniques that use light and ultraviolet to analyse the chemical structure of the substance, figure 27. UV-Vis used to measure the attenuation of a beam passing through a sample or reflected from the sample surface. When a sample is exposed to the light of wavelength with energy that matches the energy difference between a possible electronic transitions within the molecule, a fraction of the wavelength will be absorbed by the molecule and the electrons would be into a more excited energetic state. Then, a spectrometer will records the degree of absorption by a sample at different wavelengths and the resulting plot of absorbance (A) versus wavelength (λ) is known as a spectrum. Absorption measurements can be at a single wavelength or over an extended spectral range. The UV-Vis used in this work is PerkinElmer lambda 1050 spectrophotometer with 150mm integrated InGaAs sphere.

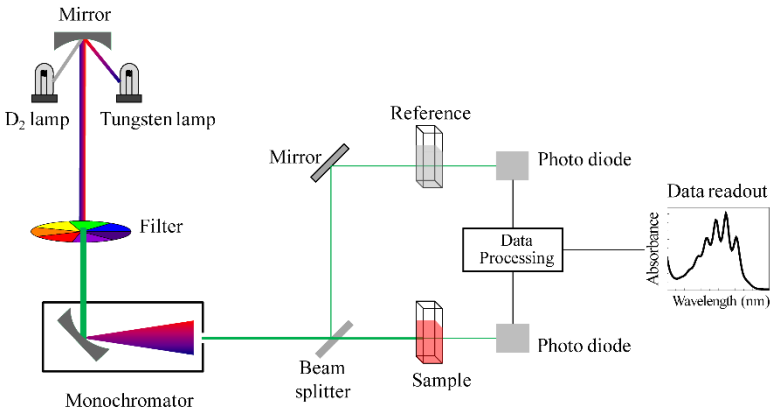

Figure 27: Schematic diagram of UV-Vis spectroscopy [10]

3.7. Substrate Preparation

As mentioned in the literature, incorporating the nanomaterials onto a solid-state substrate is a promising solution in order to overcome the limitation of nanoparticles powder. To do this, transparent conductive materials are used in our work to prepared thin film electrodes. They are totally transparent and coated with conductive thin film onto one side of it. The transparent conductive substrate used in our work is Fluorine doped tin oxide (FTO). FTO is a mechanically, chemically and electrochemically stable under atmospheric condition, and it has high-temperature resistance. [8] Before using it in our experiments, FTO needs to be cleaned in order to remove the debris present on the substrate during the fabrication, in addition to removing grease from the physical handling of the glass. Cleaning of FTOs was done by bath sonication for 15 min in distilled water, acetone and ethanol as solvents, respectively. After sonication in one solvent, FTOs were rinsed thoroughly, dipped in the next solvent and sonicated for 15 min. After completion of sonication, FTOs were washed in ethanol and dried at 100^{o}C in the oven. FTO slides were cut manually, using a diamond-edged glass cutter. The size of the FTO was dependent on the precise deposition technique and the final use of the samples.

3.8. Sol Gel Method

The sol-gel method is a common chemical synthesis approach to produce high purity materials shaped as powders, thin film coatings, fibres, and self-supported bulk structure.[9] It mainly based on inorganic polymerization reactions, initially used for the preparation of inorganic materials such as oxides gels, glasses and ceramics at low temperature. This technique attracted attention for a variety of

applications due to its low process temperature, ease of use, the ability to obtain high surface area materials and the homogeneity of the final product.

The sol-gel process, as the name implies, involves the transition of a system from a colloidal liquid 'sol' into a 'gel' solid phase.[10] Usually, inorganic metal salts or metal organic compounds such as metal oxide are used as precursors. Basically, a colloidal suspension or a 'sol' is formed after a series of hydrolysis and condensation reaction of the precursors. Then the sol particles condense into a continuous liquid phase (gel). By drying and heat treatment, the 'gel' is converted into dense ceramic or glass materials.[11] Due to the ability to adjust the viscosity of a sol into a suitable viscosity range, ceramic fibres can be fabricated from the sol.

3.9. Spry Pyrolysis Deposition (SP)

Spray pyrolysis (SP) is a low-cost, simple, non-vacuum technique for deposition of large area thin films with relatively low production cost and technological abilities for mass production.[12,13] Spray pyrolysis does not require high-quality substrates or chemicals. The SP method has been employed for the deposition of dense films, porous films, and for powder production.[14] Even multi-layered films can be easily prepared using this versatile technique.

This deposition method is based on an ultrasonic-aided generation of an aerosol of fine droplets, further blown onto a pre-heated substrate where the thin film is formed. The SP set-up consists of an atomizer, which generates very fine droplets of a precursor solution, a substrate heater, a temperature controller and a solution container (see Figure 28). In the SP method, no high temperature is required during the deposition process, therefore the deposited samples required

heat treatment in the oven at high temperature to obtain crystalline thin film materials.

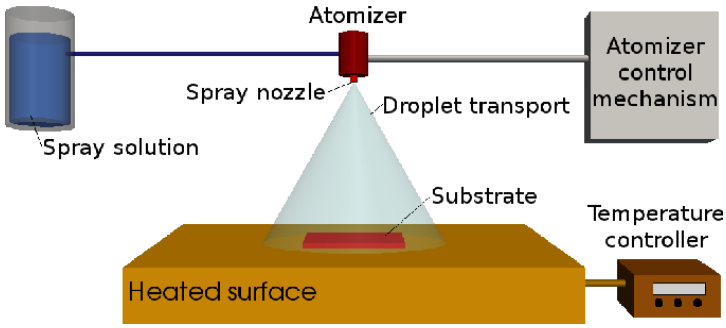

Figure 28: Schematic diagram of a spray pyrolysis deposition technique.[9]

3.10. Aerosol-Assisted Chemical Vapour Deposition (AACVD)

AACVD is a simple and cost-effective method for deposition of the thin film. AACVD based on the atomization of a suitable metal precursor into an aerosol of fine droplets that are distributed through-out a gaseous medium.[15]. AACVD technique consists of a setup of several multi-necked flasks, an aerosol generator (humidifier), and a heater (see Figure 29). In principles, the generated aerosol transported from the precursor flask through delivery tube supported by a carrier gas to a trap round flask, where the large particles trapped leaving only the small particles enclosed by fine droplets aerosol. This fine droplets aerosol subsequently transported into a heated reaction chamber, where the solvent undergoes rapid evaporation and/or decomposition, resulting in nucleation, reaction and film growth. AACVD can generate an aerosol from a variety of precursor with high-quality products. It can perform a high deposition rate and operate under low pressure in an open atmosphere without a chamber. AACVD can deposit a sample at a high temperature without the need for heat treatment.

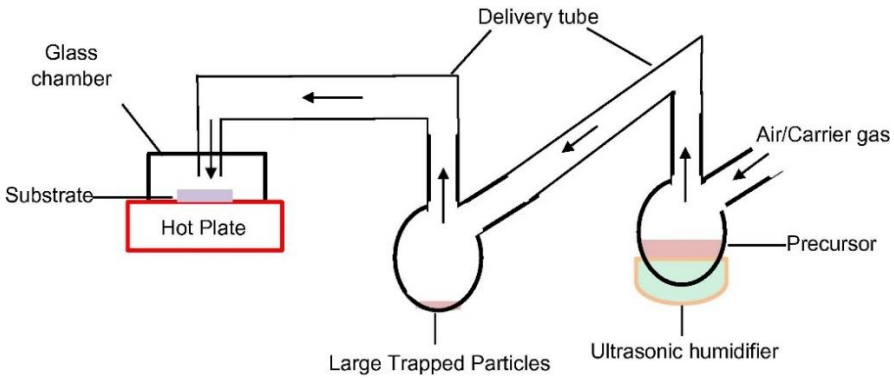

Figure 29: Schematic diagram of aerosol-assisted chemical vapour deposition method.[11]

3.11. Gas Chromatography

Gas chromatography (GC) is a separation technique in which the components of a gas sample are separated as a function of their retention coefficients in a liquid or solid stationary phase held in a column. A GC system is composed of four major components: carrier gas supply, sample injection system, column, and detector (see Figure 30). In GC, a gas sample is introduced into the mobile phase through an injector using calibrated micro-syringe. Since the sample have to be introduced into the gas phase, the temperature of the inlet system of the GC can be controlled from lower than 0^{o}C to avoid the loss of the very volatile components of samples to over 300^{o}C to volatilise the components that have very low volatility.[16] All the separated components travelled through the column and reached to the detector at different times depending on their retention coefficient. Some GC instruments have a thermal conductivity detector that can sense the changes in the thermal conductivity of the separated gas coming out of the column and then compare it to a reference flow gas which Argon in our case.

The detector sends a signal to the computer and plotted as a function of time so that each component appears in the GC as a peak at a specific time. Each component peak has an area that correlated with the % of that gas in the

headspace of the electrochemical cell. Finally, these percentages are then translated into a number of moles. The GC used in this work is Gas chromatography (GC) (PerkinElmer Clarus 580).

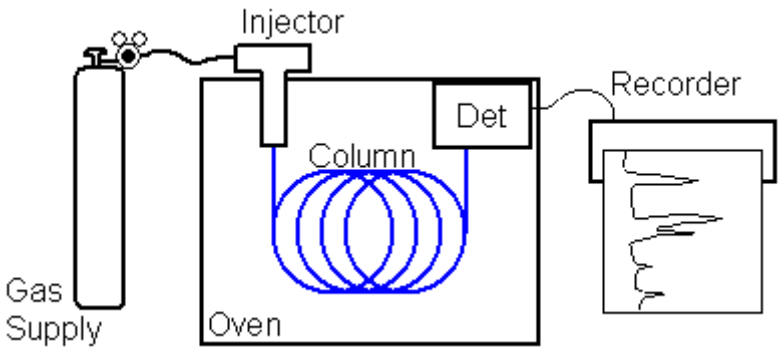

Figure 30: Schematic diagram of gas chromatography.

3.12. Photoelectrochemical Measurements

Photoelectrochemical measurements (PEC) have been performed in specially design three electrodes cell made from quartz (see Figure 31). This three-electrode configuration consists of the prepared film sample as the working electrode, a Platinum wire counter electrode and an Ag/AgCl as a reference electrode. During the measurements, the cell was filled with electrolyte in a way that the total area of the deposited film was covered with electrolyte to obtain better performance, at the same time the electrolyte not touching the crocodile clips that holding the sample to avoid short circuit issues.

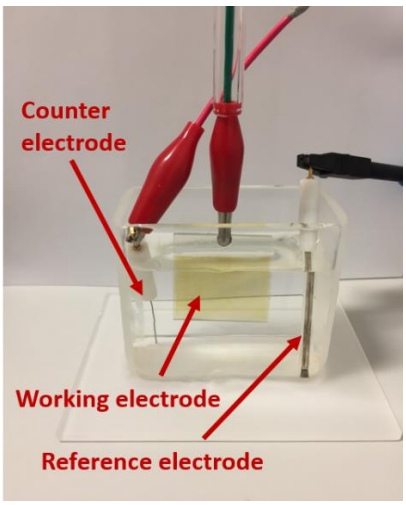

Figure 31: Three-electrode configuration photoelectrochemical cell.

PEC measurements were performed using PGSTAT12 potentiostat (Metrohum Autolab) under illumination of an AM 1.5 using a solar simulator with 100 W ozone free Xenon lamp equipped with an AM 1.5 filter (Oriel LCS-100, Newport). Most experiments were conducted in aqueous NaOH solution electrolyte with different concentrations depending on the thin film material. In my work, I used 1M to test Bi_2WO_6 and α-Fe_2O_3 thin films and 0.1M for testing $YFeO_3$.

Linear sweep voltammetry measurements are used to perfume photocurrents measurements and present it as photocurrent –potential (J-V) curve. The type of semiconductor film can be immediately suggested from the sign of the (J-V) curve; cathodic photocurrents – p-type or anodic photocurrents – n-type. The flatband potential can be obtained from the onset of the J-V curve. In photocurrents measurements, the potential of the working electrode is scanned with a constant scan rate to one direction in a potential window, while the surface of the working electrode is irradiation with pulsed or continues light. Then, the photocurrent generated by the light source is recorded with respect to the applied voltage.

Chronoamperometry measurements technique is used to investigate the stability of the synthesized photoelectrodes. A constant bias potential is applied to the working electrode (typically at which the photocurrent is high enough) followed by the periodic illumination of its surface with a light simulator. Long-term measurements are performed under continuous irradiation to obtain photocurrent transient at a certain potential, while short-term measurements are performed under chopped light irradiation.

Electrochemical Impedance Spectroscopy (EIS) measurements are used to study the effect of the composition of the nanostructured film on the electric properties. EIS works by applying a sinusoidal potential modulation at different frequencies.[17] The resulting impedance is then measured as a function of a frequency of the applied potential. The experiment is then typically repeated at potentials range to acquire a complete understanding of the system. EIS data were acquired using the Nova Software of the Autolab Instrument. Analysing EIS data is commonly performed by fitting it to an equivalent electrical circuit model (see Figure 32) consisting of electrolyte resistance and serially connected to the capacitance of double layer which is in parallel with the resistance of the charge transfer and Warburg impedance.[18]

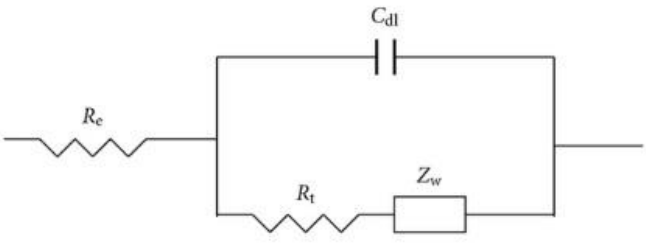

Figure 32: Electrical equivalent circuit for EIS measurements.

Mott-Schottky measurements are used to estimate the flat band potential V_{fb} of the photoelectrode. When applying a potential to the photoelectrode, the potential across the semiconductor electrolyte junction will increases. Under depletion conditions, there are only few charge carriers at the interface while under accumulation conditions the concentration of charge carriers rises resulting in the interfacial capacitance increases. Flatband potential can be estimated by measuring the photoelectrode capacitance (*C*) as a function of electrode potential (*E*). The capacitance as a function of the electrode potential (*E*) can be determined by Mott-Schottky equation:

$$\frac{1}{C^2} = \frac{2}{\varepsilon\varepsilon_0 A^2 e N_D}\left(V - V_{fb} - \frac{k_B T}{e}\right) \qquad (7)$$

Where *C* is the interfacial capacitance, ε is the dielectric constant of the electrode, ε_o the permittivity of the vacuum, *A* is the area of electrode, N_D is the number of donors, *V* is the applied voltage, V_{fb} is the flat band potential, k_B is Boltzmann's constant, *T* is temperature and *e* is the electronic charge. Thus, a plot of $1/C^2$ with respect to applied potential V should lead to a straight line from which V_{fb} can be determined from the intercept with the x-axis.

3.13. Hydrogen Generation

Hydrogen generation experiment was performed using custom-made glass reactor vessel (see Figure 33) with an attached fused silica viewport containing 0.1 M NaOH (pH 13) electrolyte with a dead space of 100ml (total vessel volume is 520ml). The sealed vessel has three-neck on top of it, two of them have a working electrode and a Platinum mesh connected by a single outer wire and the third one is sealed with plastic stopper for taking a test sample by calibrated micro-syringe. Before illumination, the vessel was purged with argon for 2 hours with gentle heating and stirring to remove atmospheric air from the system. The

photoelectrode inside the sealed vessel was subjected to light illumination from the silica viewport side. Hydrogen samples have been taken out every hour using the sample syringe and analysed using gas chromatography (GC).

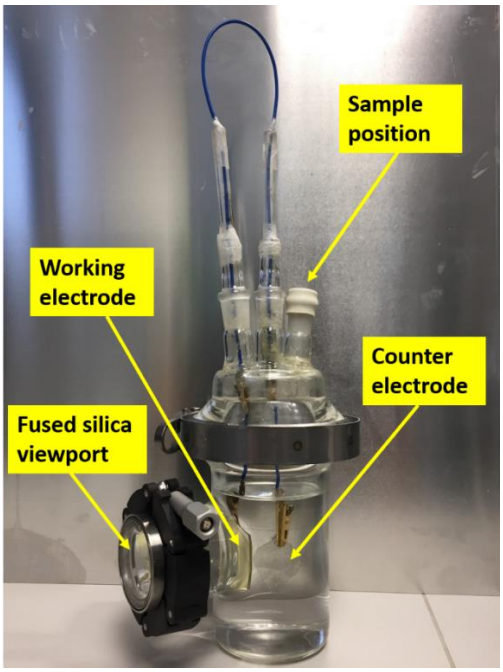

Figure 33: Hydrogen generation reactor

3.14. Dye Degradation

Dye degradation experiments were performed in a quartz cuvette reactor containing 60ml of a dye solution. Prior to irradiation, the electrode was in the dye solution under a dark condition for 30 min to establish an absorption/desorption equilibrium between the dye solution and the electrode. Then, the sample was clamped and immersed into the dye solution and subject to light irradiation. A solar simulator is used to illuminate the sample from the film side. During the reaction, the given amount of the dye solution was sampled at certain time intervals to check the degree of degradation, which was done by measuring the

absorbance at a certain wavelength as a function of reaction time. After the measurement, the dye sampled was returned to the reactor to keep the total volume of the reaction roughly equivalent. Different dyes have been used in this work to investigate the photocatalytic activity of the prepared photoelectrode.

3.15. References

(1) Epp, J. In *Materials Characterization Using Nondestructive Evaluation (NDE) Methods*; Elsevier: **2016**, p 81.

(2) Suga, M.; Asahina, S.; Sakuda, Y.; Kazumori, H.; Nishiyama, H.; Nokuo, T.; Alfredsson, V.; Kjellman, T.; Stevens, S. M.; Cho, H. S. *Progress in Solid State Chemistry* **2014**, *42*, 1.

(3) Hanke, L. D. *Materials Evaluation and Engineering Inc., Plymouth* **2001**, 35.

(4) Braz, A.; López-López, M.; García-Ruiz, C. *Forensic science international* **2013**, *232*, 206.

(5) Das, R. S.; Agrawal, Y. *Vibrational spectroscopy* **2011**, *57*, 163.

(6) Bumbrah, G. S.; Sharma, R. M. *Egyptian Journal of Forensic Sciences* **2016**, *6*, 209.

(7) Seo, Y.; Jhe, W. *Reports on Progress in Physics* **2007**, *71*, 016101.

(8) Banyamin, Z.; Kelly, P.; West, G.; Boardman, J. *Coatings* **2014**, *4*, 732.

(9) Keshmiri, M.; Troczynski, T.; Mohseni, M. *Journal of hazardous materials* **2006**, *128*, 130.

(10) Wright, J. D.; Sommerdijk, N. A. *Sol-gel materials: chemistry and applications*; CRC press, **2014**.

(11) Yang, L., California Institute of Technology, **2005**.

(12) Patil, P. S. *Materials Chemistry and Physics* **1999**, *59*, 185.

(13) Tomar, M.; Garcia, F. *Progress in Crystal Growth and Characterization* **1981**, *4*, 221.

(14) Perednis, D., ETH Zurich, **2003**.

(15) Powell, M. J.; Potter, D. B.; Wilson, R. L.; Darr, J. A.; Parkin, I. P.; Carmalt, C. J. *Materials & Design* **2017**, *129*, 116.

(16) Wang, Z.; Paré, J. J. In *Techniques and Instrumentation in Analytical Chemistry*; Elsevier: **1997**; Vol. 18, p 61.

(17) Cesiulis, H.; Tsyntsaru, N.; Ramanavicius, A.; Ragoisha, G. In *Nanostructures and Thin Films for Multifunctional Applications*; Springer: **2016**, p 3.

(18) Maouche, N.; Nessark, B. *International Journal of Electrochemistry* **2011**, *2011*.

Chapter 4: Unassisted Solar Water Splitting Using Stable $YFeO_3$ Photocathodes

Recently, significant efforts have been made to generate H_2 using unassisted PEC system. The core-shell $WO_3/BiVO_4$/CoPi heterojunction produced 102µmol/h with GaAsP photovoltaic and yield photocurrent of 6.56mA cm^{-2}. [1] Photocell devices containing a *p*-$LaFeO_3$ photocathode and *n*-Fe_2O_3 photoanode have generated 11.5 µmol/h of hydrogen without photovoltaic assistance.[2] Also, single oxide materials have been investigated for PEC water splitting. α-Fe_2O_3 has been reported to generate unassisted H_2 from water, only after dope it with Pt. [3] $LaFeO_3$ photoelectrode has been demonstrated to generate unassisted H_2 and 0.18 µmol/cm^2 of hydrogen is reported. However, its low photocurrent hinder its PEC hydrogen evolution, where the amount of hydrogen decreased to half after the second cycle of the water splitting test. Along with PEC water splitting, $YFeO_3$ has been investigated in water remediation[4,5], and photochemical hydrogen evolution[6] using powder sample. A recent study investigated $YFeO_3$ as photocathode in PEC water splitting, however, it suffers from low photoresponse and poor carrier mobility due to the lack of a sophisticated fabrication technique for high quality nanostructured thin films. [7]

To the best of my knowledge, I report for the first time the fabricated of nanostructured $YFeO_3$ photocathode for spontaneous hydrogen production from water without external applied bias. The $YFeO_3$ photocathode was fabricated by spray-pyrolysis technique, a novel, inexpensive and scalable method, to create a stable thin film p-type semiconductor material which displays an ideal band structure with band edges above and below the redox potential of water. The

fabricated photocathode achieved excellent PEC performance and high stability under redox water.

4.1. Experimental

4.1.1. Optimization of Fabrication Parameters of $YFeO_3$

As the aim of this work is to fabricate $YFeO_3$ material for hydrogen generation, optimization of fabricated methods to obtain the crystalline phase of the material is essential. Fabrication of $YFeO_3$ starts with the sol-gel method to investigate the optimum annealing temperature to obtain a crystalline form of the $YFeO_3$ nanoparticles. Once the optimum annealing temperature is optimised, it will then use to synthesise the $YFeO_3$ in a form of a thin film to overcome the limitation of $YFeO_3$ nanoparticles applications.

4.1.2. Synthesis of Pure $YFeO_3$ by Sol Gel

A sol-gel method described in section 3.8 was used to fabricate pure $YFeO_3$ powder. $Fe(NO_3)_3 \cdot 9H_2O$ (0.1mole) and $Y(NO_3)_3 \cdot 5H_2O$ (0.1 mole) was dissolved in 25ml distilled water and mixed in a stoichiometric ratio of Y: Fe =1:1. Citric acid was then added as a complexing agent to the above solution to yield a Y:Fe:CA ratio of 1.1:4. The solutions stirred for 2 h at room temperature to ensure the complete chelating of metal ions. The resulting solution then heated at 80^oC under stirring to evaporate the liquid phase and formed a sticky gel, followed by drying at 120^oC for 24 h to obtain a yellowish green solid. The dried gel was grounded and calcined in the muffle furnace at different temperatures (600^oC, 700^oC and 800^oC) for 6h to form the nanocrystalline powders.

4.1.3. Fabrication of $YFeO_3$ by AACVD

AACVD method described in section 3.10 was used to fabricate $YFeO_3$ thin film. In a typical deposition, 20 mL of deposition solution described above section was taken in a 50 mL round-bottom flask and placed above the ultrasonic humidifier. Air at a flow rate of 120 mL/min was used as the carrier gas to transfer the aerosol from the solution flask to the trapped flask. The generated aerosol droplets of the precursor were transferred into the hot wall zone of the reactor by another carrier gas with a flow rate of 300ml/min. The substrate was aligned on the hotplate so that aerosol reaches the FTO glass substrate and falls vertically from the top. The substrate was heated up to the deposition temperature for 20 min before the deposition starts.

4.1.4. Fabrication of $YFeO_3$ by Spray Pyrolysis

The $YFeO_3$ photocathodes were prepared by spray pyrolysis. Iron $(acac)_3$ (5 mmoles), $Y(NO_3)_3$. $6H_2O$ (5 mmoles), and DTAB (5 mmoles) were dissolve in 200ml methanol. A few droplets of polyethylene glycol (PEG) were added to the prepared solution and stir it at 60^oC for 5 min. Once it cold down, the solution used for spray pyrolysis. Fluorine-doped tin oxide (FTO) glass was cleaned according to the cleaning procedure described in section (3.7) in the experimental chapter. The precursor solution was sprayed at 200^oC via a syringe pump (New Era Pump Systems NE-1000), an ultrasonic atomizer nozzle (Sonozap) 1mm diameter and a vortex attachment. A certain amount of prepared solution was sprayed on to the FTO at a rate of 1ml/min assisted with compressed air at a rate of 4$Lmin^{-1}$. The prepared sample was annealed at different temperatures for 3 hours.

4.1.5. Characterization

X-ray diffraction (XRD) was acquired using Siemens D5000 diffractometer using a Cu Kα radiation. 40kV/ 40mA, 0.02 $^{o}2\theta$ step and a scan time of 2.5 seconds per step) in the range of 20-80 $^{o}2\theta$. The surface morphology and composition of the thin film was characterized using a high-resolution scanning electron microscope (SEM, TESCAN VEGA3). Film thickness was characterized using a focus ion beam (FIB, NOVA NanoLab FEI 600 dual beam FIB-SEM). Optical absorption measurements were acquired using a spectrophotometer (PerkinElmer lambda 1050 with 150mm integrated InGaAs sphere. The Raman shift pattern was obtained using the Renishaw RM1000 (Renishaw plc, Gloucestershire, UK) with a 532 nm Ar ion-laser.

4.1.6. Photoelectrochemical Measurements

The photoelectrochemical (PEC) measurements of $YFeO_3$ photoelectrode was acquired in 0.1 M NaOH electrolyte (pH 13) using Metrohm Autolab potentiostat under chopped light using a 100 W ozone free Xenon lamp equipped with an AM 1.5 filter (Oriel LCS-100, Newport). The light intensity was 1 sun illumination (100 mW cm^{-2}). A liner sweep voltammetry (LSV) was scanned in the positive to a negative direction between the ranges of +0.3 V to -0.7 V vs Ag/AgCl. Chronoamperometric (CA) measurements of $YFeO_3$ were performed over a period of 6 hours with periodic light chopping. The sample was illuminated from the film side for 30 minutes and another 30 minutes in dark conditions. This was conducted in a standard 3 electrode system in ambient temperature. All the potentials described in this study refer to the reversible hydrogen electrode (RHE) potential, which was calculated according to following the formula: $V_{RHE} = V_{Ag/Agcl} + 0.197+0.059*pH$.

4.1.7. Hydrogen Evolution Measurements

Hydrogen evolution measurements were carried out using gas chromatography (GC) (PerkinElmer Clarus 580). A custom-made glass reactor vessel (see Figure 33 in section 3.13) with an attached fused silica viewport containing 0.1 M NaOH (pH 13) with a dead space of 100ml was purged with argon for 2 hours with gentle stirring to remove atmospheric air from the system. The sealed vessel contained the working $YFeO_3$ electrode connected to a Pt mesh by a single outer wire and was subjected to light illumination for the water splitting reaction. GC measurements were taken every 1 hour.

4.2. Results and Discussion

Sol-gel method has been used to fabricate of a crystalline single phase of $YFeO_3$. Figure 34, shows XRD patterns of the prepared $YFeO_3$ powder at various calcination temperatures. There is no observable peak in the sample annealed at 600^oC, indicating the amorphous form, while sample annealed at 700^oC shows characteristic XRD peaks without observable impurities according to JCPDS no. 48-0529. All peaks were corresponding to a hexagonal phase of $YFeO_3$. As the calcination temperature further increases to 800°C, single orthorhombic $YFeO_3$ (JCPDS no. 39-1489) were obtained.

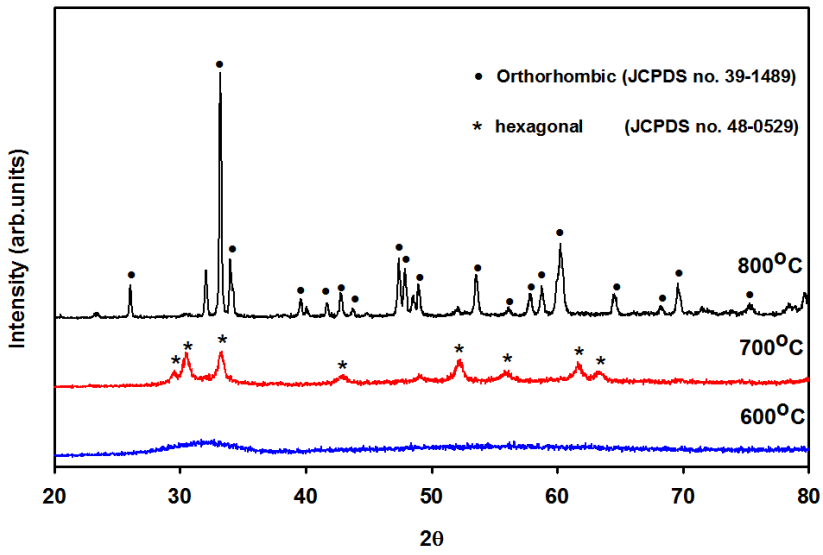

Figure 34: XRD patterns of $YFeO_3$ samples obtained at different calcination temperatures.

The XRD results confirmed that crystalline phase of $YFeO_3$ can be obtained at high calcination temperature (>600°C), where no $YFeO_3$ peaks could obtain below this temperature. This result is in good agreement with previous XRD results described elsewhere.[8]

Based on the above observation, I attempt to use the formed sticky gel to coat FTO glass to fabricate photoelectrode for water splitting process. Doctor-blade coating technique has been used to coat the film. The coated film then annealed at different temperatures (600°C, 650°C and 700°C). It's observed that the sample annealed at 600°C has cracked coated film and not uniform. This can be due to the gases generated during the heating process were suddenly evolved in the coated film, leading to bubbles, cracks or delamination.[9] Further increase in the annealing temperature leads to the melting of the substrate.

To overcome this drawback, I tried to use the aerosol-assisted chemical vapour deposition (AACVD). This deposition method is based on an ultrasonic-aided generation of an aerosol, further blown onto a pre-heated substrate. With this

method, it's expected to coat the surface with particles that progressively undergo thermal decomposition, therefore avoiding a brisk gas evolution and associated cracking of the dried film. As expected, the coated film was uniform, homogeneous and adherence to the substrate. However, deposition of the coated film at a high temperature (>600^{o}C) is required to obtain a crystalline phase of $YFeO_3$. Since the maximum deposition temperature of AACVD is around 500^{o}C, synthesis crystalline phase of $YFeO_3$ by this method was unsuccessful.

An alternative method to synthesise crystalline phase of the $YFeO_3$ film is based on two fabrication processes, where the film coated first at low temperature followed by heat treatment at high temperature. A simple, low cost and rapid spray pyrolysis technique has been used, where fine droplets of liquid precursor are sprayed onto a heated substrate. This technique is very sensitive to the surface temperature. Both structural and optoelectronic properties of the coated film can change significantly if deposited at different surface temperature.[10] When the deposition temperature is too low, the precursor's droplets only evaporates and decomposes on the substrate. If the deposition temperature is increased, the solvents will evaporate before hitting the substrates leaving the precipitate to decompose on the substrate. With further increase in the temperature, decomposition will take place in the vapour phase where solvents completely evaporate and form solid particles before hitting the substrate. This high temperature resulted in powdery ash which will have poor adherence to the FTO substrate.

Spray rate is another parameter that could affect the morphology of the thin films deposited using spray pyrolysis. Higher spray rate results in the formation of rough films. It has already been reported that films deposited at lower spray rates are uniform and thinner due to higher re-evaporation rate.[11] Also, there are

reports saying that changes in spray rate could affect properties like surface morphology, crystallinity, resistivity and even thickness. It is generally observed that lower spray rate favoured formation of better crystalline films.[11]

From our experience with spray pyrolysis deposition, its observed that uniform films have been started obtaining from substrate temperature 200^{o}C onwards and spray rate below 2ml/min. So the substrate temperature is maintained at 200^{o}C and spray rate at 2ml/min. The substrate size used in this work is fixed at 3X3 cm. These parameters are fixed for all thin films samples fabricated by spray pyrolysis. All the spray parameters are listed in table 1. Synthesis $YFeO_3$ film by SP method has been discussed in details in the following section.

Table 1: Summary of the spray pyrolysis parameters

Substrate type	Fluorine-doped tin oxide (FTO)
Substrate size	3x3 cm
Temperature of the heating device	200°C
Liquid flow rate	2ml/min
Heating rate	2°c/min
Final temperature	600°C
Calcination time	3h

4.2.1. Characterization

XRD was used to study the crystallinity of the $YFeO_3$ film. To do this, $YFeO_3$ films were sprayed at 200^{o}C and then annealed at a different temperature from

500°C to 700°C with an increment of 50°C (see Figure 35). It's observed that at low temperature, the XRD peaks for $YFeO_3$ was not detected at 500°C. The $YFeO_3$ XRD peaks start appearing at 550°C and become more crystalline with the increase in temperature. The sample annealed at 600°C tend to have more crystalline peaks, which considered as the optimal sample for rest of characterization and measurements. Additional investigation to study the crystallinity of the sample is to do XRD for the sample before and after measurements. The XRD patterns (see Figure 36) represent the crystalline phase of $YFeO_3$ before and after H evolution test to investigate any texture change. Peaks marked with ***** symbol represent FTO substrate, where the other three peaks, namely, [100], [103], and [121] provides further evidence for the existence of $YFeO_3$ (JCPDS no. 00-048-0529). Strong FTO peaks comparing to small $YFeO_3$ peaks due to the small thickness of the $YFeO_3$ film, therefore, no new phase is detected. There is no crystal structure change after hydrogen evolution test which indicates the high stability of the $YFeO_3$ film.

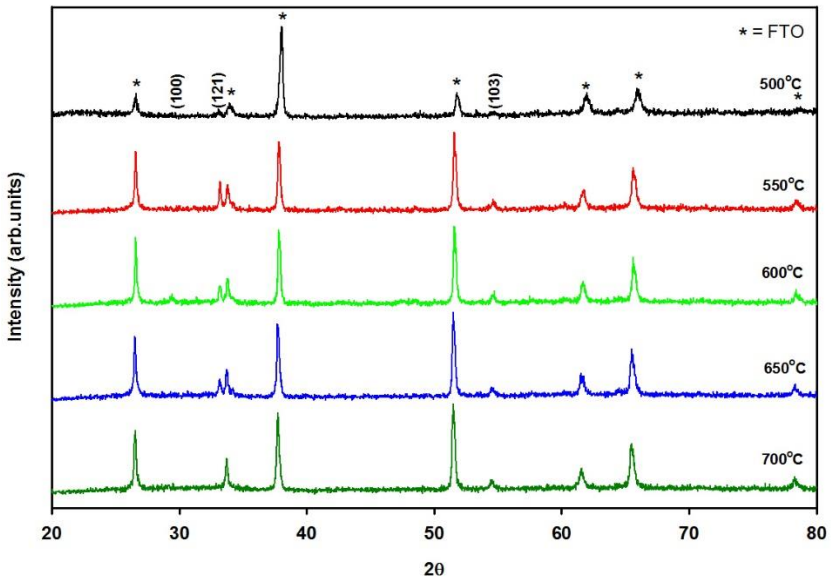

Figure 35: XRD pattern of $YFeO_3$ thin film at different annealing temperature.

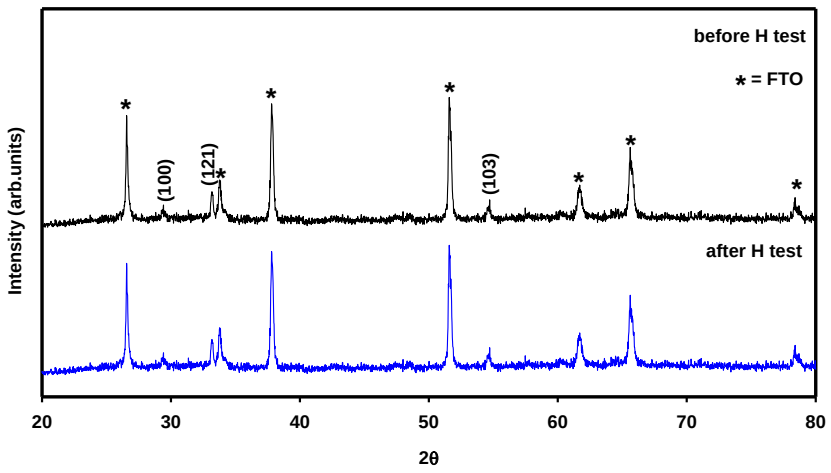

Figure 36: XRD pattern of $YFeO_3$ thin film deposited on FTO glass substrate before and after H evolution test: * symbols indicate the peaks from FTO glass, and the others are related to the $YFeO_3$ film.

Figure 37 shows the Raman spectrum of $YFeO_3$ which is in good match with literature data[12,13] . The pattern shows the structural phase of the film before and after hydrogen test. It shows that there is no change in the structure phase of the film after the hydrogen test. This result is well agreed with the XRD pattern, which provides strong evidence that the film has high stability and does not degrade into iron oxide and Yttrium oxide. The vibration mode around 221 cm^{-1} (A_{1g}) is assigned to FeO_6 octahedral. Other peaks are related to Fe-O bonds (282 cm^{-1} (B_{1g}), 334 cm^{-1} (B_{2g}), 420 cm^{-1} (A_{1g}), 498 cm^{-1} (B_{3g})), and Y-O bonds (146 cm^{-1} (A_{1g}), and 178 cm^{-1} (A_{1g})[12]. The strong peak at 650 cm^{-1} arises from the two-phonon process may be due to crystal disorder[13]. The peak at 1302 cm^{-1} can be attributed to the vibration of magnetic Fe^{3+} ions, which is well agreed with other reports for $YFeO_3$[14,15].

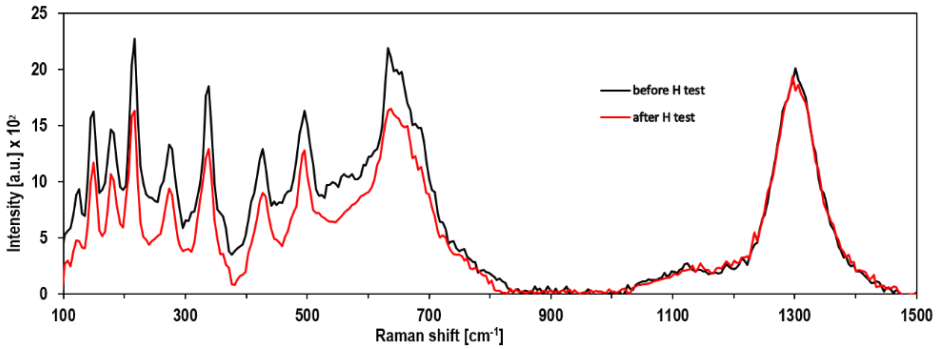

Figure 37: Raman spectrum of $YFeO_3$ electrode, before and after hydrogen test.

Surface morphology of $YFeO_3$ film annealed at 600^oC before and after the hydrogen evolution was investigated (see Figure 38a and b). SEM provides clear evidence that the nanostructure of $YFeO_3$ retains its uniformity and good interconnection between the crystal grains. Figure 38c shows the cross-section of the film with approx. 270nm thickness. The similarity in uniformity and interconnection between the crystals before and after the test are also confirmed by AFM images presented in Figure 39.

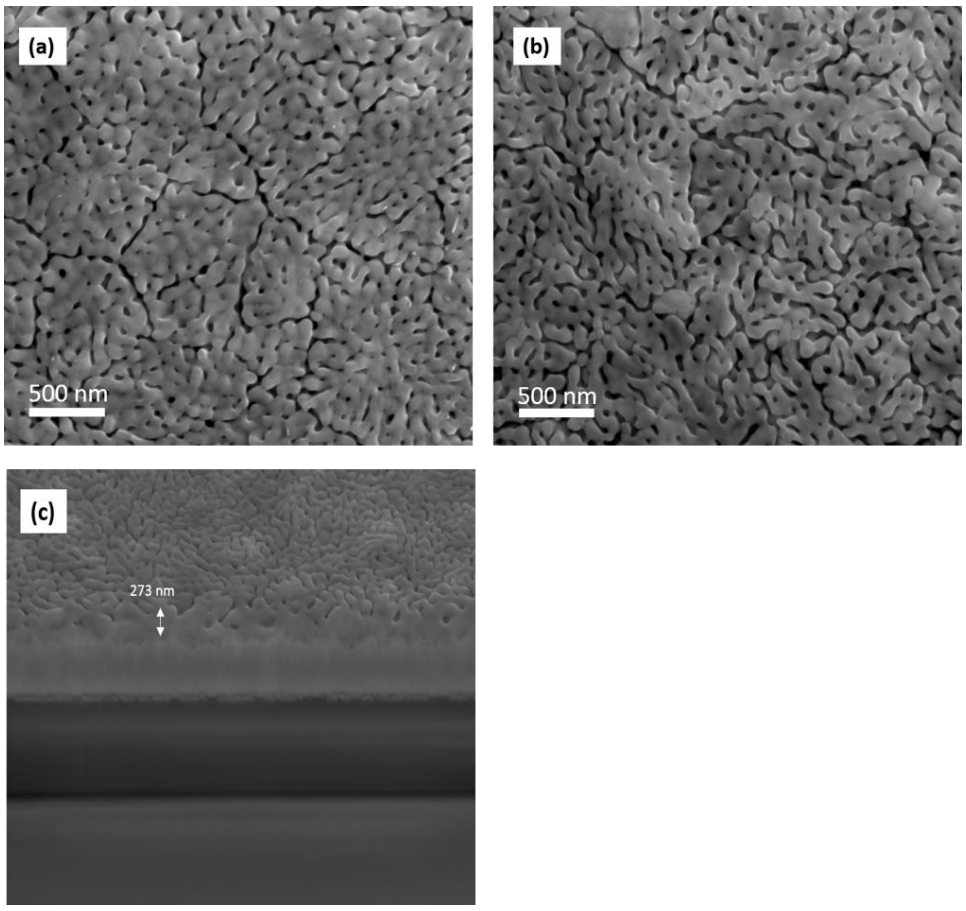

Figure 38: (a) SEM of $YFeO_3$ thin film before hydrogen evolution test, (b) after, (c) cross section of $YFeO_3$ film.

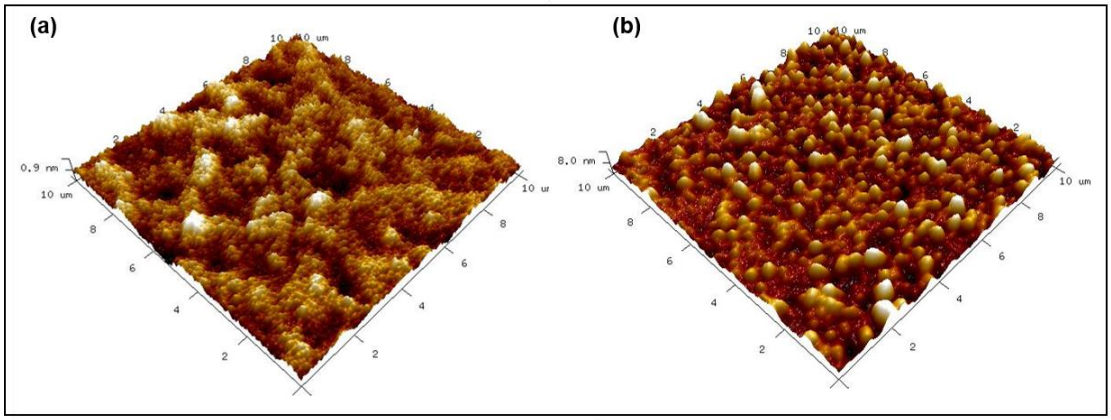

Figure 39: AFM images of $YFeO_3$ electrode, (a) before and (b) after hydrogen test.

Figure 40 shows the EDX of $YFeO_3$ indicating the Yttrium, iron and oxygen peaks, which confirming the composition of the materials and well match it with the XRD patterns. Figure 41 shows the element mapping of homogeneously mixed of Yttrium and iron in the $YFeO_3$ film, which confirmed the uniformity of the film.

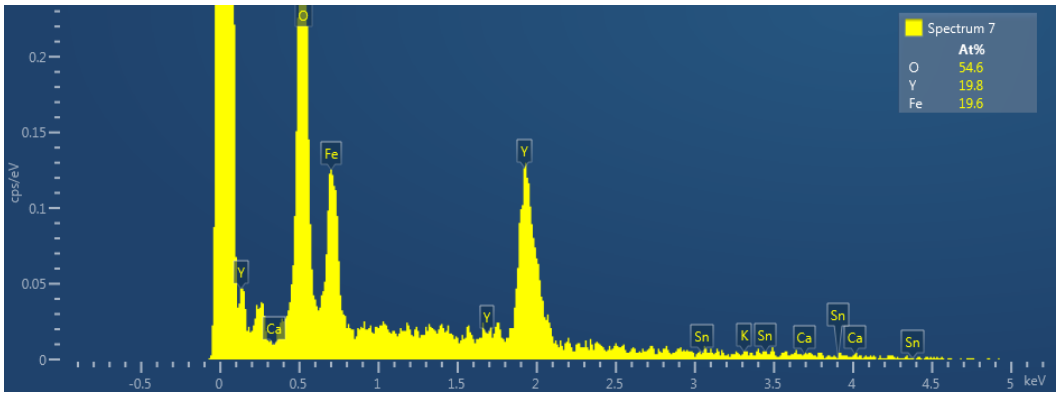

Figure 40: EDX of $YFeO_3$ film showing peaks of Yttrium, iron and oxygen.

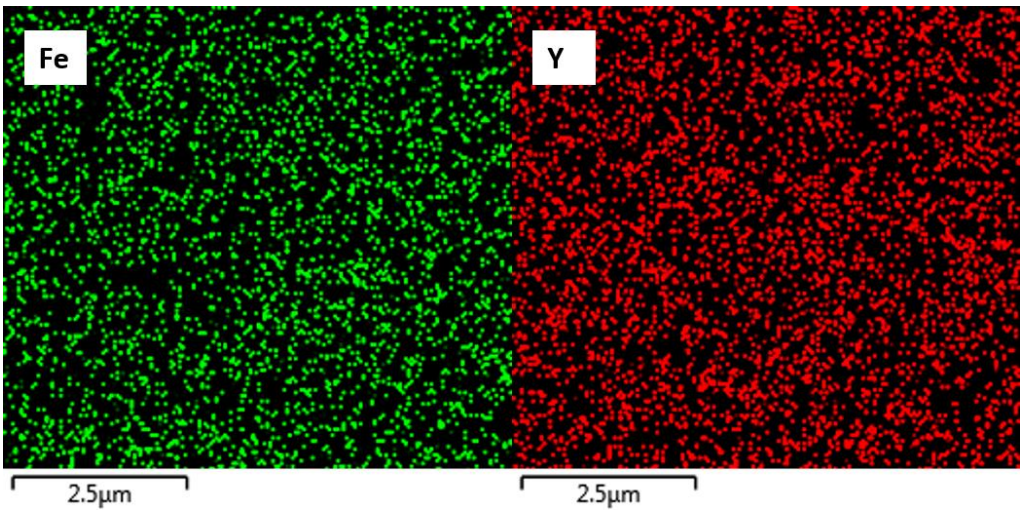

Figure 41: EDX of $YFeO_3$ showing the distribution of yttrium and iron in the film.

4.2.2. Photoelectrochemical Analysis

The photoelectrochemical (PEC) performance of $YFeO_3$ photocathodes was measured in a three-electrode cell device as working electrodes to observe their PEC photoresponse under AM 1.5G simulated solar light irradiation. A platinum wire electrode, Ag/AgCl electrode, and 0.1 M NaOH (pH 13) were also employed in the cell as a counter electrode, reference electrode, and electrolyte, respectively. The photocurrent density (*J*) is plotted against applied bias potential (*V*) (see Figure 42). The steady-state photocurrent onset estimated from the *J*-*V* plot was at 1.34V vs RHE. The photocurrent density rises up to approximately 0.6 mA cm^{-2} at 0.5 V vs. RHE, while no dark current was observed between the potential ranges.

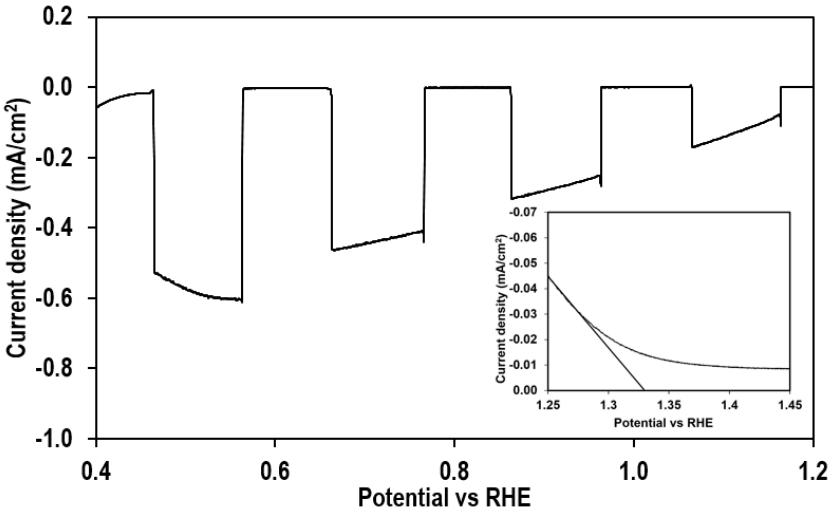

Figure 42: Photocurrent –potential (J-V) curve of $YFeO_3$ under chopped light in 0.1 M pH NaOH. The J-V plot in the inset shows photocurrent onset.

A chronoamperometric test of the $YFeO_3$ photocathode was carried out to investigate its stability under illumination and dark conditions. The stability test was performed in a NaOH electrolyte solution 0.1M (pH 13) at a constant potential of −0.3V over a period of 6 hours under chopped light, where the film was

illuminated for 30 minutes and another 30 minutes in dark conditions (see Figure 43). From the stability test, it is observed that the current density increased during the test and remain still after 2 hours until the end of the test, which indicated the high stability of the $YFeO_3$ photoelectrode. In addition, long-time stability under a dark condition for 21 hours confirmed the high stability of the photoelectrode (see Figure 44).

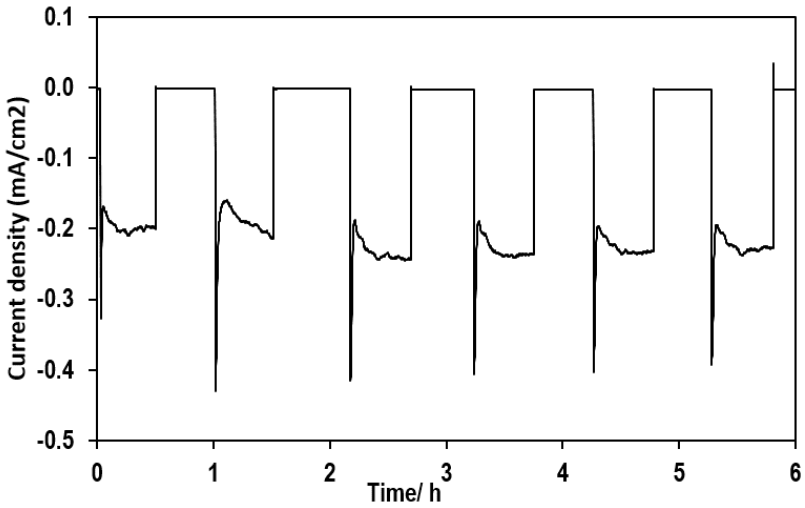

Figure 43: Chronoamperometry test of $YFeO_3$ under chopped light at −0.3V vs Ag/ AgCl.

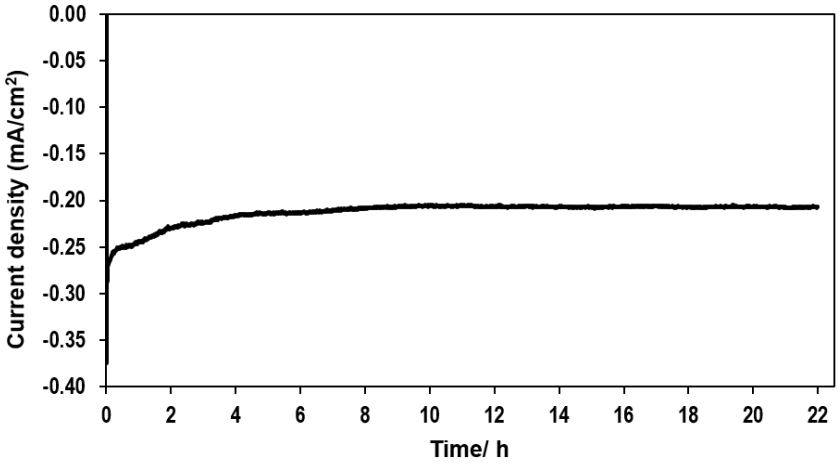

Figure 44: Chronoamperometry test of $YFeO_3$ under dark condition at −0.3V vs Ag/ AgCl.

Annealing temperature and spray amount have been investigated to optimise the best fabrication conditions of $YFeO_3$ photoelectrode. Figure 45 shows that the photocurrent density starts increasing with the increase of annealing temperature and reaches the optimum level at 550 °C. Meanwhile, the photocurrent decreased significantly with further increase in the annealing temperature. The decrease in the photocurrent at the lower temperature (<550°C) can be due to incomplete decomposition and sintering of film respectively[16]. While at high temperature (> 600°C), the FTO glass substrate starts to melt which leading to defect in the $YFeO_3$ film.

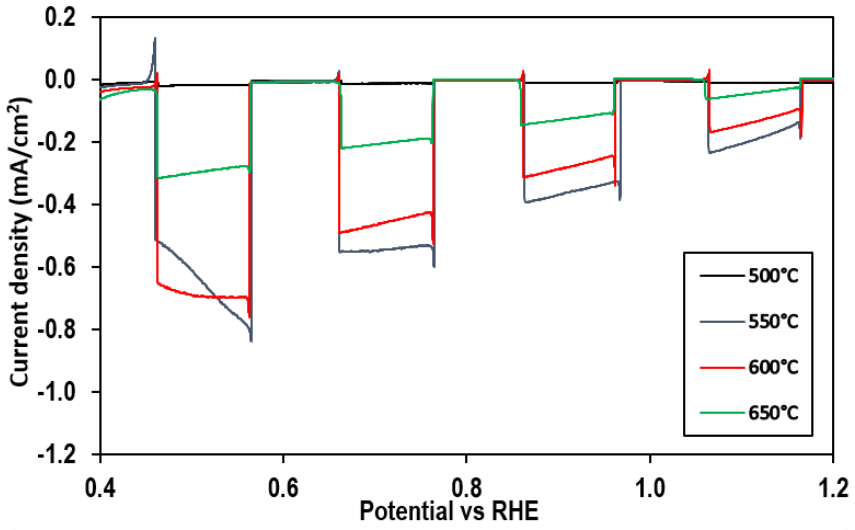

Figure 45: Photocurrent –potential (J-V) curves of $YFeO_3$ at various annealing temperatures.

The relation between photocurrent density and the amount of spray solution /time were investigated (see Figure 46). In addition, the relation between the amount of spray solution /time and the electrode thickness is observed during the experiments. The sample sprayed by 10 ml of solution is relatively thin and shows the lowest photoresponse. The photocurrent density increases with the increase of spray time and reaches the maximum at 30 ml spray amount and then start to decrease. The sample which showed the maximum photocurrent density

had a thickness of approx. 273 nm and corresponds to 30 ml spray solution/30 minutes of spray time (based on 1ml/min spray rate). Low photocurrent density in the electrode with higher thickness most likely due to the photogenerated charges required to travel more before collecting at the FTO substrate, which makes the charges slow and trapped within $YFeO_3$ photoelectrode[17].

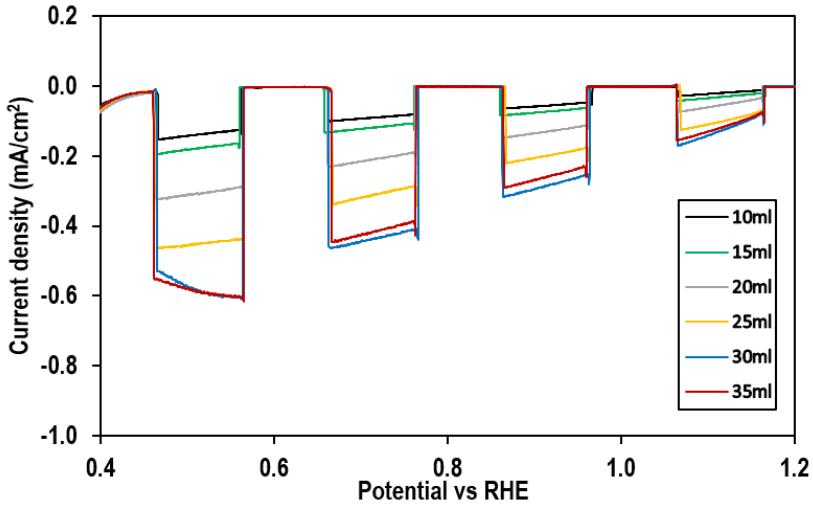

Figure 46: Photocurrent –potential (J-V) curves of different film thickness.

4.2.3. Optical and Electrochemical Measurements

The optical absorbance properties of $YFeO_3$ were investigated to help determine the materials band gap. The absorbance spectrum for the $YFeO_3$ photoelectrode was performed between the ranges of 350– 800 nm (see Figure 47). The recorded optical spectrum was used to determine the bandgap energy of $YFeO_3$ photoelectrode. The optical bandgap (Eg) can be calculated according to the following equation:

$$\alpha h\nu = A_o(h\nu - E_g)^n, \qquad (8)$$

where α is the absorption coefficient, $h\nu$ is the photon energy in eV, and E_g is the band gap energy. A_o is constants, and n value is equal to 1/2 for direct and 2 for indirect allowed transitions. Figure 48 shows the Tauc plot of $\alpha h\nu$ *vs.* $h\nu$ for

$YFeO_3$ photoelectrode and the direct bandgap of 2.45eV was estimated, where the red line intersects the x-axis. The bandgap value for $YFeO_3$ is in good agreement with the other works conducted.[7,18]

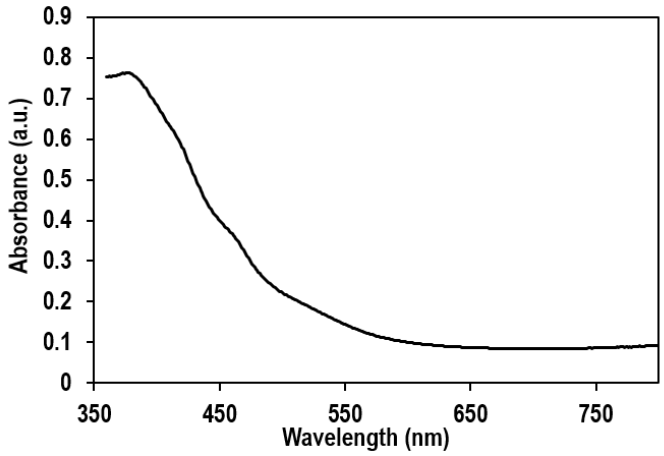

Figure 47: Absorbance spectra of $YFeO_3$ photoelectrode.

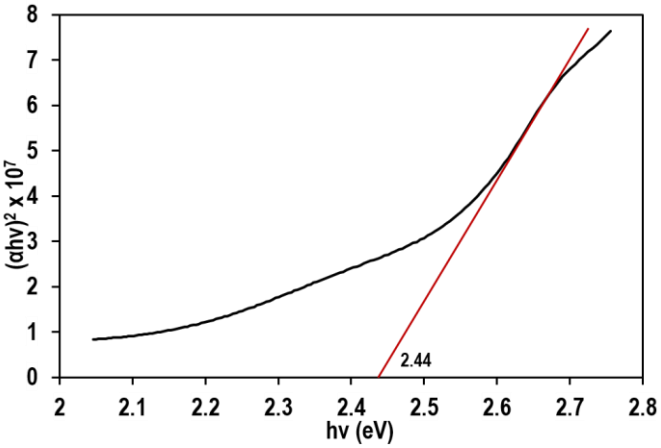

Figure 48: Tauc plot of $YFeO_3$ showing the band gap energy (Eg).

Electrochemical impedance measurements (EIS) were conducted in order to determine the semiconductors flat band potential. Figure 49 shows the Nyquist plot of impedance spectrum of our $YFeO_3$ film where the measurements conducted in a range between 0.6 and 1.5V vs VRHE where the electrode is in the depletion region and in a frequency range from 100 KHz to 100 mHz. The Mott-Schottky plot was constructed by using the space charge capacitance

values estimated by fitting the impedance responses to a Randles circuit and it shows p-type characteristics of the $YFeO_3$ film. The flat band potential of $YFeO_3$ electrode was determined through a linear fit in the linear region of the Mott-Schottky plot and were calculated to be 1.44V vs RHE (see Figure 50). The flat band potential agrees well with the photocurrent onset potential measured from *J-V* curve.

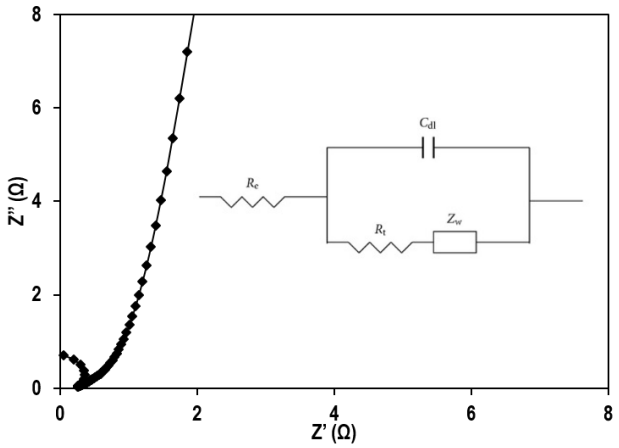

Figure 49: Electrochemical impedance plot showing experimental and fitted impedance data for the $YFeO_3$ thin film.

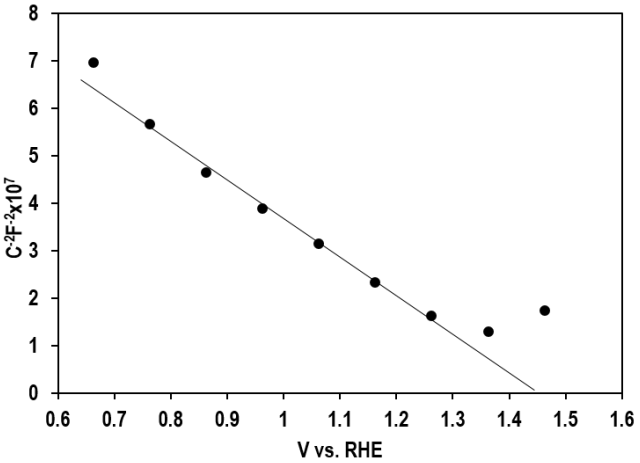

Figure 50: Mott-Schottky plot of $YFeO_3$ thin film.

From the flat band and band gap potentials values, I can construct a band diagram of the $YFeO_3$ electrode corresponding to the water redox potentials (see Figure 51). The band diagram shows that the valance and the conduction bands

is able to straddling the redox potential of water with a narrow band gap. These findings show that the $YFeO_3$ photoelectrode is able to generate hydrogen from water.

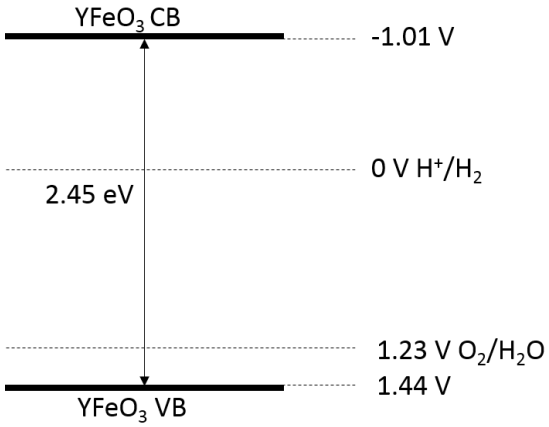

Figure 51: Band diagram of $YFeO_3$ electrode vs RHE.

4.2.4. Hydrogen Evolution Measurement

Water splitting experiments were carried out in custom-made glass reactor vessel (see Figure 33 in section 3.6) attached with fused silica viewport. Figure 52 shows the hydrogen evolution performance of the $YFeO_3$ photocathode in aqueous 0.1 M NaOH solution. Table 1, presents the amount of hydrogen generated at each hour for 1st and 2nd experimental attempts. The $YFeO_3$ as working electrode was connected with a Pt mesh counter electrode by a single outer wire, where no external bias is applied. Hydrogen was being produced spontaneously during the water splitting test during the first 6 hour cycle where the photoelectrode generated 0.41 µmol/cm^2 of hydrogen after 6hours. The $YFeO_3$ photoelectrode was subject to the second cycle of hydrogen evolution test to investigate the capability of reuse. After 6 hours illumination, the $YFeO_3$ photocathode generated 0.35 µmol/ cm^2 of hydrogen (see table 1). This proves that the film is re-usable, however, the amount of hydrogen produced is slight decrees. This can be due to

the electrolyte particles accumulated onto the film surface, which decreased the amount of light being absorbed by the film.

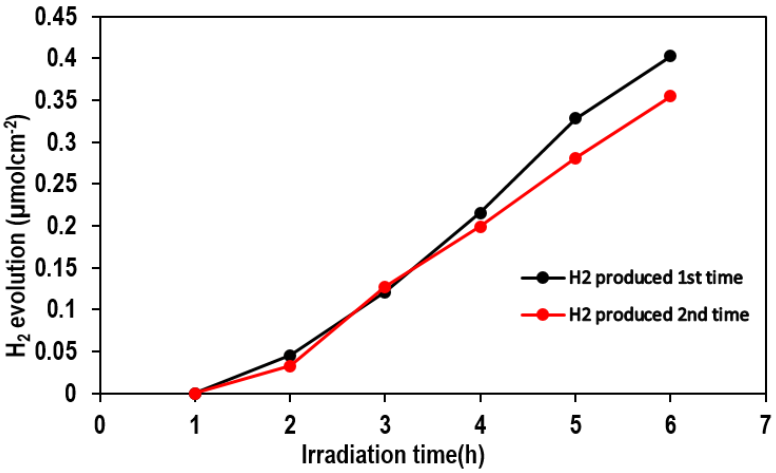

Figure 52: Hydrogen generation by $YFeO_3$ electrode in an aqueous 0.1 M NaOH.

Table 2: Hydrogen amounts generated (µmol/ cm^2)

	1h	2h	3h	4h	5h	6h
1st time	0	0.04	0.12	0.22	0.33	0.41
2nd time	0	0.03	0.12	0.19	0.28	0.36

4.3. Summary of $YFeO_3$ Work

In summary, stable p-type $YFeO_3$ photocathodes have been fabricated by a novel and inexpensive spray pyrolysis technique. The results showed that the best sample performance was obtained using a spray rate at 2ml/min and 600°C calcination temperature, which yields a photocurrent density of 0.6 mA cm^{-2} at 0.5 V vs. RHE. Chronoamperometric studies showed that the $YFeO_3$ film has high stability with a p-type response over a 6 hour period under chopped light and 21h

in the dark condition. Optical measurements showed that the photoelectrode has a bandgap of 2.45eV. Water splitting test demonstrated that the $YFeO_3$ photocathode generates 0.41 μmol/cm^2 of hydrogen after 6hours without external bias. The second cycle of hydrogen test proves that the electrode is re-usable and 0.35 μmol/cm^2 of hydrogen is generated after 6 hours of light illumination. These findings prove that $YFeO_3$ is a potential candidate to act as a photocathode for unassisted water splitting to generate hydrogen at a competitive cost.

4.4. References

(1) Pihosh, Y.; Turkevych, I.; Mawatari, K.; Uemura, J.; Kazoe, Y.; Kosar, S.; Makita, K.; Sugaya, T.; Matsui, T.; Fujita, D. *Scientific reports* **2015**, *5*, 11141.

(2) Yu, Q.; Meng, X.; Wang, T.; Li, P.; Liu, L.; Chang, K.; Liu, G.; Ye, J. *Chemical Communications* **2015**, *51*, 3630.

(3) Kim, J. Y.; Magesh, G.; Youn, D. H.; Jang, J.-W.; Kubota, J.; Domen, K.; Lee, J. S. *Scientific reports* **2013**, *3*, 2681.

(4) Tang, P. S.; Tang, C. W.; Ying, J. N.; Ni, D. J.; Yang, Q.; Wu, L. M. In *Key Engineering Materials*; Trans Tech Publ: **2015**; Vol. 636, p 7.

(5) Chen, Y.; Yang, J.; Wang, X.; Feng, F.; Zhang, Y.; Tang, Y. *Journal of the Ceramic Society of Japan* **2014**, *122*, 146.

(6) Khraisheh, M.; Khazndar, A.; Al-Ghouti, M. A. *International Journal of Energy Research* **2015**, *39*, 1142.

(7) Díez-García, M. I.; Celorrio, V.; Calvillo, L.; Tiwari, D.; Gómez, R.; Fermin, D. J. *Electrochimica Acta* **2017**, *246*, 365.

(8) Zhang, Y.; Yang, J.; Xu, J.; Gao, Q.; Hong, Z. *Materials Letters* **2012**, *81*, 1.

(9) Stevens, F., Université de Liège, Liège, Belgique, **2016**.

(10) Ong, C. K. **2013**.

(11) Sebastian, T.; Jayakrishnan, R.; Sudha Kartha, C.; P Vijayakumar, K. *The Open Surface Science Journal* **2009**, *1*.

(12) Yu, J.-G.; Yu, H.-G.; Cheng, B.; Zhao, X.-J.; Yu, J. C.; Ho, W.-K. *The Journal of Physical Chemistry B* **2003**, *107*, 13871.

(13) Lazarević, Z. Ž.; Jovalekić, Č.; Gilić, M.; Ivanovski, V.; Umićević, A.; Sekulić, D.; Romčević, N. Ž. *Science of Sintering* **2017**, *49*, 277.

(14) Mathur, S.; Veith, M.; Rapalaviciute, R.; Shen, H.; Goya, G. F.; Martins Filho, W. L.; Berquo, T. S. *Chemistry of Materials* **2004**, *16*, 1906.

(15) Ma, Y.; Chen, X.; Lin, Y. *Journal of Applied Physics* **2008**, *103*, 124111.

(16) Pawar, G. S.; Tahir, A. A. *Scientific reports* **2018**, *8*, 3501.

(17) Peter, L.; Wijayantha, K. *Electrochimica Acta* **2000**, *45*, 4543.

(18) Tang, P.; Chen, H.; Cao, F.; Pan, G. *Catalysis Science & Technology* **2011**, *1*, 1145.

Chapter 5: Fabrication of Bi_2WO_6 Photoelectrodes by Spray Pyrolysis for Rhodamine B (RhB) Degradation

In recent decades, a great deal of attention has been given to visible-light responding semiconductor photocatalysts in the degradation of organic pollutants in water for solving environmental pollution problems by the efficient full utilization of solar energy.[1] Various new visible-light-active semiconductor materials have been extensively investigated, such as InTaO4,[2] BiVO4,[3] InVO4,[4] etc. They show promising potential for utilization for solar energy. However, their application still restricted due to their limitation of low photocatalytic efficiencies. Therefore, great efforts have been made to improve the activity of these materials by preparing the semiconductor in a form of thin film.[5] Recently, Bi_2WO_6 has attracted extensive interest for its good performance in organic pollutants degradation,[6,7] visible-light-induced photocatalyst,[8] photoelectrochemical (PEC) water splitting[9] and CO_2 reduction.[10]

Bi_2WO_6 possesses very interesting intrinsic physical and chemical properties, such as ferroelectric piezoelectricity, catalytic activity and nonlinear dielectric susceptibility.[11] It is well known that the photocatalytic and PEC properties are closely interrelated and highly depends upon particle size, morphology and structure. In early work, photocatalysts have been utilized as suspended powders.[12] However, the limitations such as low photocatalytic activity and the laborious recollection of the powder from the suspension have considerably restricted their applications. In order to overcome such obstacles, nanostructured film photoelectrodes on solid supports have been developed later. Such nanostructured photoelectrodes exhibit a large internal surface area, high porosity, and excellent photocatalytic performance. In order to study the optical,

electrochemical, electronic and PEC properties, nanostructured photoelectrodes should be prepared on optically transparent conducting substrates. Unfortunately, the fabrication of highly crystalline nanostructured thin film photoelectrodes of Bi_2WO_6 on such substrates and a systematic study of PEC properties associated with nanostructure and texture has not yet been examined in detail.

Stimulated by novel properties related to nanostructures, the preparation of efficient visible-light sensitive Bi_2WO_6 photoelectrodes by systematically controlling the nanostructure and texture is the primary aim of this particular work. Also, the preparation of highly soluble and volatile solutions containing Bi and W compounds in aqueous and organic solvents have been described. In this work, Bi_2WO_6 nanostructured photoelectrodes with nanoplates structures are fabricated by Spray Pyrolysis (SP). This novel method is a simple and reproducible route to construct nanostructured Bi_2WO_6 photoelectrodes.

Moreover, the photoelectrodes prepared in this work has shown considerably high photocurrent as well as a high activity for photocatalytic degradation of Rhodamine B (RhB) dye. Our findings will undoubtedly have a significant influence on further exploitation of Bi_2WO_6 as a potential semiconductor material in solar energy conversion and photocatalytic applications.

5.1. Experimental

Since the purpose of this work is to fabricate nanostructured Bi_2WO_6 photoelectrodes, the effect of annealing/deposition temperature and fabrication method on the formation of crystalline Bi_2WO_6 photoelectrodes need to optimize. Based on observation from $YFeO_3$ fabrication mentioned in section (4.1.), film prepared by sol gel method facing crucial issues such the gases generated during

the heating process could evolve in the coated film, leading to bubbles, cracks or delamination.[13] Due to this limitation, I decided to use spray pyrolysis to fabricate the nanostructured Bi_2WO_6 photoelectrodes. The optimized parameters for fabrication of thin films using this method are discussed in section (4.1.1.). Meanwhile, the experimental work, measurements and results are discussed in this section.

5.1.1. Preparation of Precursor Solution

Analytical grade chemicals and reagents were purchased from Sigma-Aldrich and used without further purification. Distilled water was used throughout the experiment. The solution used for the deposition of Bi_2WO_6 photoelectrodes was prepared as follows: 5.0 g of diethylenetriaminepenta-acetic acid (DTPA) and 15 mL of ammonia water (30%) were added to 300 mL of distilled water. 1.8 g of Bi_2O_3 powder and 1.0 g of $(NH_4)_6\ H_2W_{12}O_{40}\cdot xH_2O$ powder were added to the above stirring solution. The mixture was further stirred and heated to 80 °C in order to promote the dissolution and subsequent reaction. After 4 hours of stirring, the mixture became a colorless transparent solution. The solution was evaporated to dryness under reduced pressure to eliminate any volatile by-product and access ammonia. The resulting powder was re-dissolved in 100 mL of distilled water to obtain a transparent precursor solution.

5.1.2. Deposition of Photoelectrodes by Spray Pyrolysis (SP)

The Bi_2WO_6 photoelectrodes were deposited by the SP process. Fluorine-doped tin oxide (FTO) glass substrates were cleaned according to the cleaning procedure described in section (3.7) in the experimental chapter. The spray system comprised of a syringe pump system (New Era Pump System NE-1000),

an ultrasonic atomizer nozzle (Sonozap) 1mm diameter and a vortex attachment.[14] 10 ml of the precursor solution was sprayed on to the FTO at a rate of 1 ml min^{-1} assisted with compressed air at a rate of 3 L min^{-1}, which is passed through the vortex attachment to generate a large plume of aerosol to get a uniform coverage on the FTO. After the completion of spray, the films were further annealed at different temperatures in air.

5.1.3. Characterization

The crystalline structure of deposited photoelectrodes was analyzed by an X-ray diffractometer (Siemens D5000 diffractometer) with Cu-K_α (λ= 1.541Å) radiation at a scan rate of 0.07˚ s^{-1}. The morphology and composition of film photoelectrodes were characterized by scanning electron microscopy (SEM, TESCAN VEGA3) operated at an acceleration voltage of 5.0 kV. Raman spectroscopy was undertaken using a Renishaw RM1000 Raman spectrophotometer. The spectrum was recorded in the range of 100 to1000cm^{-1}.

5.1.4. Optical and Electrochemical Characterization

Room temperature UV-Vis absorption spectra were recorded on a Lambda 35 Perkin-Elmer UV-Vis spectrophotometer in the wavelength range of 200-800 nm. A bare FTO coated glass substrate was placed in the reference optical path, thus the absorbance measurements included only contributions from Bi_2WO_6 photoelectrodes.

A three-electrode electrochemical cell, fitted with a quartz window, was used for photoelectrochemical studies. An aqueous solution of 1M NaOH was used as the electrolyte. The potential of the Bi_2WO_6 working electrode was controlled by a potentiostat (Metrohm Autolab). An Ag/AgCl/3M KCl electrode was used as the

reference electrode and a Pt wire was adopted as the counter electrode. In the electrochemical cell, light enters through a quartz window and travels about a 5mm path length in the electrolyte before illuminating the photoelectrode. The Bi_2WO_6 photoelectrode was illuminated through the electrolyte side and the illumination source was an AM1.5 solar simulator (Oriel LCS-100, Newport).

The Mott-Schottky relationship was used to calculate the flat band potential (V_{fb}) of nanostructured Bi_2WO_6 photoelectrodes. The Mott-Schottky plots were constructed using capacitance data obtained from a cyclic voltammetry (CV) technique described by Eggleston et al.[15] and Boschloo et al.[16] using the equation below.

$$c = \frac{dQ}{dV} = \frac{i\,dt}{dV} = \frac{i}{v} \qquad (9)$$

with Q the charge, V the potential and *i* the current. The Cyclic voltammograms (CVs) were measured in different pH electrolytes to calculate the pH dependence of flat band potential.

5.1.5. Photocatalytic Degradation of Rhodamine B (RhB)

The light source for photocatalytic measurements was a 100 W ozone free Xenon lamp (Oriel LCS-100, Newport) with 420 nm filter. Degradation of rhodamine B (RhB) was performed in a quartz cuvette reactor containing 60ml of RhB (20mg/L) and 1ml of H_2O_2. Prior to irradiation, the suspension was kept in the dark for 30 min to establish absorption/desorption equilibrium between RhB solution and the electrode. During the reaction, 3 mL of RhB solution was sampled at certain time intervals to check the degree of degradation, which was done by measuring the absorbance at 554 nm as a function of reaction time. After the measurement, the sampled RhB solution was returned to the reactor to keep the total volume of the

reaction roughly equivalent. Bi_2WO_6 electrodes prepared at different calcination temperatures were used in the experiment in order to investigate the influence of annealing temperature of electrodes on the efficiency of degradation.

5.2. Result and Discussion

Nanostructured Bi_2WO_6 photoelectrodes were successfully prepared through a simple procedure employing SP processes. A comparative study of the effect of annealing/deposition temperature on the morphology and PEC properties of the photoelectrodes was conducted.

5.2.1. Characterization

The phase and crystallinity of photoelectrodes were characterized by XRD and all peaks indexed by (*) in XRD peak pattern correspond to the substrate fluorinated SnO_2 layer, while the remaining reflections were indexed to orthorhombic phase (Russellite) Bi_2WO_6 with space group (see Figure 53). The peak pattern is in good agreement with the reported data for Bi_2WO_6 (ICDD 01-073-2020).[17]

Raman spectra of as-prepared photoelectrodes are shown in Figure 54. The peaks in the range of 600–1000 cm^{-1} are assigned to the stretches of the W–O bands, according to the Grane et al.[18] The bands at 760 and 790 cm^{-1} of Bi_2WO_6 were associated with the antisymmetric and symmetric A_g modes of terminal O–W–O chain. The band of 310 cm^{-1} could be assigned to translational modes involving simultaneous motions of Bi^{3+} and WO_4. The bands at about 300 cm^{-1} were assigned to the modes of the terminal WO_2 group. The W–O bonds of intermediate length (about unit valency) are characteristic of bridging W–O bonds

and are assigned to Raman mode stretching wavenumbers in the range of 700–1000 cm^{-1}.[19] As can be seen (Figure 54) the intensity of peaks increase with the increase in annealing temperature indicate that the crystallinity of photoelectrode increase with temperature. These observations are in good agreement with SEM and XRD results.

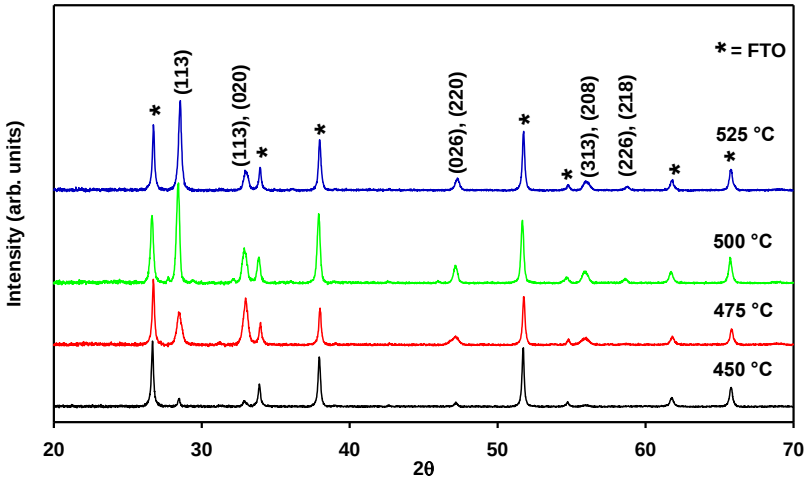

Figure 53: The XRD peak pattern of Bi_2WO_6 photoelectrode at different annealing temperatures.

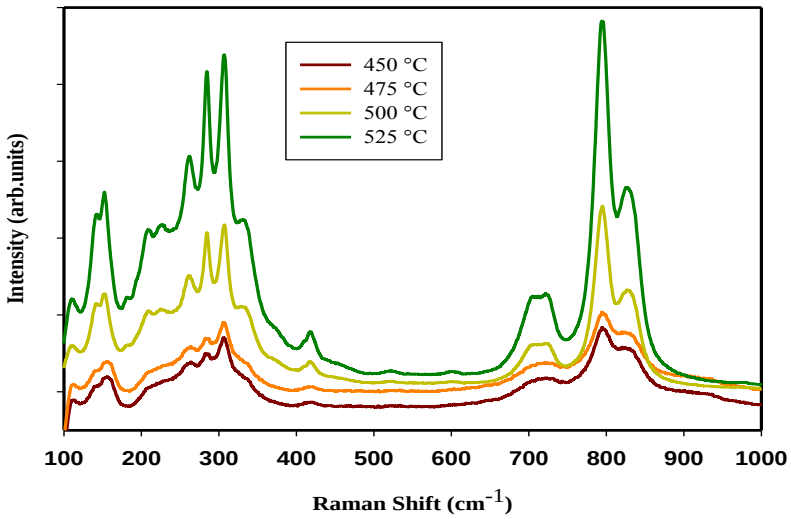

Figure 54: Raman Spectra of Bi_2WO_6 photoelectrodes deposited by spray pyrolysis and annealed at 450 °C to 525 °C

The effect of the annealing/deposition temperatures on the nanostructure and morphology of Bi_2WO_6 photoelectrodes prepared by SP were investigated in detail. In order to study the effect of substrate temperature on crystallinity and morphology, photoelectrodes were annealed on different substrate temperatures while all other parameters were kept constant.

The effect of annealing temperature on properties of photoelectrodes prepared by SP was studied over the temperature range of 450 - 525 ºC. Figure 53 illustrates the effect of annealing temperature on electrode structure and morphology. The XRD peak pattern showed that the Bi_2WO_6 phase was achieved at 450 ºC with very small peak intensities which may be due to poor crystallinity. The peak intensity increased with the increase in annealing temperature indicating the enhanced crystallinity which was further confirmed by SEM analysis of corresponding photoelectrodes.

The analysis of SEM images show that the photoelectrodes annealed at different temperatures. At 450 ºC the electrode consists of big lumps with very uniform (see Figure 55). With the increase of temperature, the lumps began to disperse and particles with divergent boundaries. The growth of particles with specific shape became more apparent with the increase of annealing temperature as elucidated by progressive SEM images (Figure 55b and 55c). The particles acquired a near cuboids shape after annealing at 525 ºC as shown in SEM image (Figure 55c). These Bi_2WO_6 particles have a length of about 100 – 150 nm and a thickness of about 50 - 70 nm and are linked together to make a porous structured electrode.

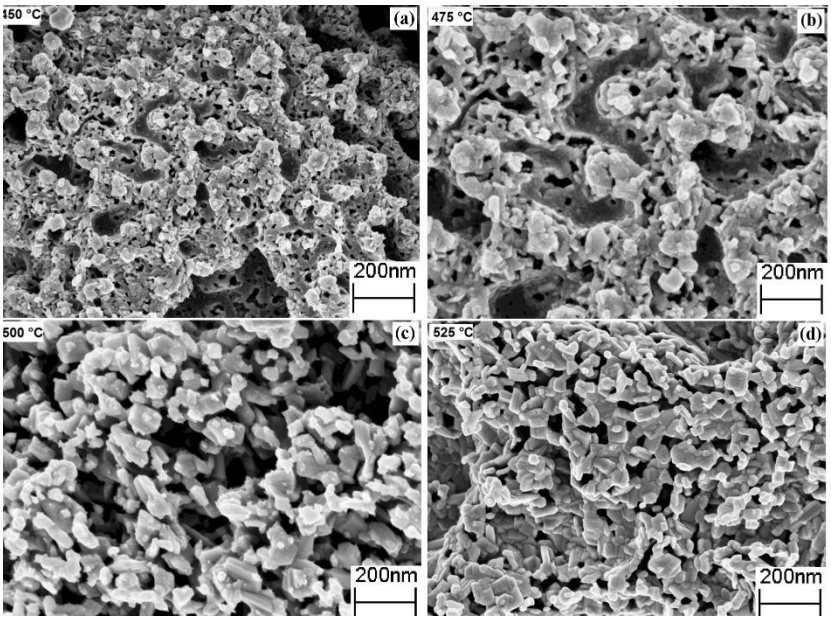

Figure 55: The SEM micrographs of photoelectrodes deposited by SP and annealed at 450 - 525 °C (a-d).

5.2.2. Photoelectrochemical Analysis

The photoelectrochemical properties of Bi_2WO_6 photoelectrodes were investigated under AM 1.5 illumination in a 3-electrodes open quartz cell. The steady-state *J*-V plots in Figure 56 show the dependence of photocurrent density on the annealing temperature. The photocurrent increases with the increase of annealing temperature. The crystallite size, orientation and morphology of the photoelectrodes drastically varied with the annealing temperature. Further increased of deposition/annealing temperature could not be continued beyond a certain limit due to the instability of glass substrate at high temperature (>550 °C). The result indicates that the textural properties ,as well as the degree of crystallographic preferred orientation, are the key factors in defining the light harvesting and charge transfer properties.[20] The photocurrent increased rapidly with the applied potential, which could be due to the fact that the high internal surface area exposed to the electrolyte provides a large effective semiconductor/electrolyte interface. Thus, the separation of photogenerated

carriers within the width of the space charge layer becomes a key factor to enhance PEC performance of photoelectrodes.

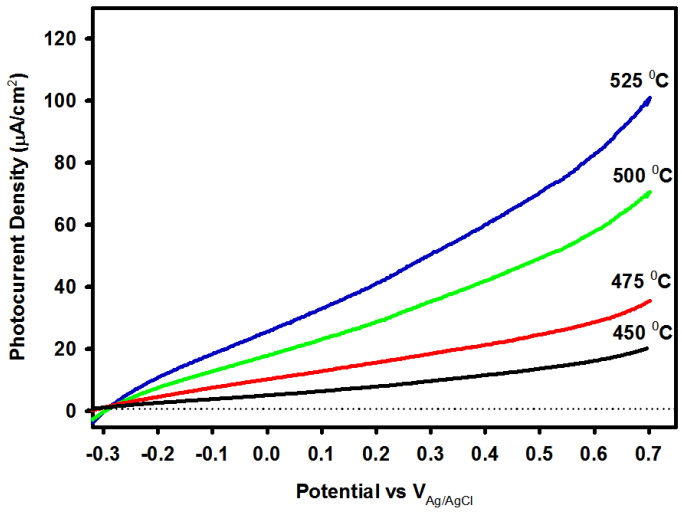

Figure 56: J-V plots showing the dependence of photocurrent on annealing temperature for the photoelectrodes.

The best photoelectrodes prepared using the SP methods have been studied under chopped light (AM 1.5 illumination) to reveal the dark current simultaneously. Figure 57 describes the photocurrent transients in the potential range that encompasses the photocurrent and dark current onset potentials. For comparison, the steady-state *J-V* plot was superimposed on the transient plot in each case. Steady-state and transient *J-V* plots agree well for all photoelectrodes. Generally dark current starts at about 0.6 V (vs. Ag/AgCl/3M KCl) in 1M NaOH electrolyte. This photoelectrode has shown about 42 μAcm^{-2} photocurrent density at 0.23 V (vs Ag/AgCl/3M KCl) under AM1.5 illumination and a negligible dark current (Figure 57). However, the recombination characteristics are evident in photocurrent transients. This indicates that the light harvesting properties of Bi_2WO_6 photoelectrodes depend on the fabrication conditions which are directly related to the texture, morphology and preferred orientation of photoelectrodes.[21]

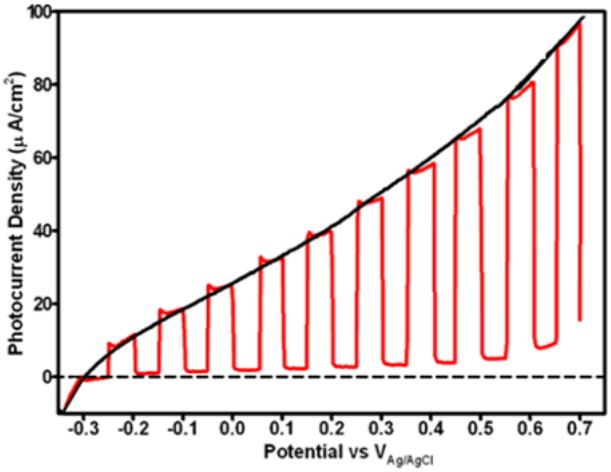

Figure 57: Chopped and steady state J-V plot of porous nanostructured annealed at 525 °C.

5.2.3. Optical and Electrochemical Measurements

In Bi_2WO_6, Bi^{+3} has two 6s valence electrons in the crystalline phase. The band structure of Bi_2WO_6 was suggested to be composed of W5d (conduction band, CB) and hybridization of Bi6s and O2p (valence band, VB).[22] It has been reported that Bi_2WO_6 thin films have a steep absorption edge in the visible range, indicating that it is due to the intrinsic transition within the material related to the fundamental absorption edge rather than the transition from impurity levels.[23]

The optical properties of Bi_2WO_6 samples were recorded using UV/Vis spectroscopy. Figure 58 shows direct bandgap of thin films for Bi_2WO_6 film photoelectrodes for porous nanoplate electrode deposited by SP at different temperatures. For a crystalline semiconductor, it was shown that the optical absorption near the band edge follows the equation $(\alpha h\nu)^n = A(h\nu - E_g)$, where α, ν, E_g, and A are light absorption coefficient, frequency, bandgap, and a constant, respectively. Among them, n decides the characteristics of the transition in a semiconductor. Bi_2WO_6 is a direct bandgap material. The annealing temperature has a slight effect on bandgap (E_g) and the bandgap estimated by extrapolation

of the plots of $(\alpha h\nu)^2$ versus $h\nu$ are 2.82 eV (Figure 58) and are comparable to the reported values for Bi_2WO_6 powder nanoparticles.[6]

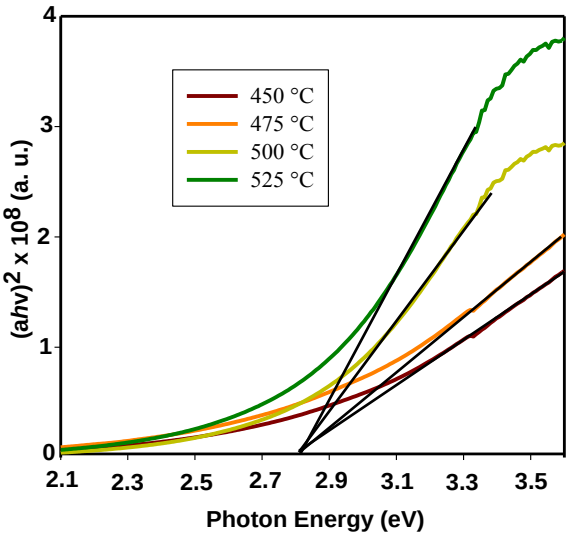

Figure 58: Plot of $(\alpha h\nu)^2$ versus photon energy (hv) for Bi_2WO_6 photoelectrodes deposited by spray pyrolysis and annealed at 450 °C to 525°C.

One of the important parameters in the study of the semiconductor-electrolyte interface is flat-band potential which explains the electrochemical characteristics of the system in dark and under illumination. Cyclic voltammograms of Bi_2WO_6 photoelectrodes are measured in three photoelectrodes mode under the dark condition at different scan rates in different pH electrolytes. The potential range is such that the Bi_2WO_6 photoelectrodes are always under depletion conditions; i.e., the applied potential is more negative than the flat band potential (V_{fb}). An intriguing feature of these CVs is that the current is an approximately linear function of the applied potential, in the directions of both the forward and the reverse scans. Furthermore, the current at a given potential is linearly dependent on the scan rate. The CVs of Bi_2WO_6 photoelectrodes did not show any electrochemical interfacial redox reactions indicates that the origin of the current is capacitive.

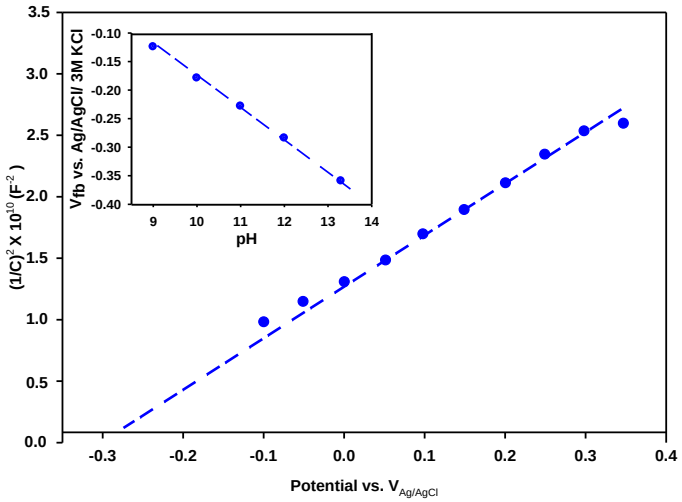

Figure 59: Mott−Schottky plot constructed using capacitance data calculated from slope of anodic lines of current vs. scan rate at each potential measured at pH 13.3 for Bi_2WO_6 photoelectrodes annealed at 525 °C while inset shows pH dependence of the flatband potential (V_{fb}) for Bi_2WO_6 photoelectrode.

In the absence of interfacial redox reactions, the scan-rate (n) dependence of current can be attributed to charging and discharging of the space charge layer. The CVs collected for a series of scan rates, the current (i) was plotted versus scan rate (n) at selected applied potential. The slope of the line in such a plot is a measure of space charge layer capacitance (C_{SC}) at each potential. The data from the forward scans of the CVs are used to calculate the capacitance to construct the Mott−Schottky plots (i.e., C^{-2} vs V) and the flat band potential was estimated by extrapolating the linear part of the Mott−Schottky plots. The Mott−Schottky plot determined at pH 13.3 for the photoelectrode is given in Figure 59. The flat band potential 2.85 V estimated from the Mott−Schottky plot remarkably agrees with the photocurrent onset potentials which further support the negative shift of the photocurrent onset associated with hierarchical microsphere structures.

It is well known that the flat band potential of many semiconductors in contact with aqueous electrolytes depends on the pH of the solution. The relationship between V_{fb} and the pH was linear with a slope of about 60 mV per pH unit (Figure

58 inset), which is very close to the Nernstian response (-59 mV/pH) expected for reactions involving protons and hydroxide ions. The photoelectrodes conform the Nernstian slope to the entire range of measured pH particularly and the V_{fb} and its pH dependence support the argument that the nanoplate structures provide high internal surface area which allows more electrolyte solution to penetrate to the interior of each porous nanostructure providing a large semiconductor/electrolyte interface to enhance the photoelectrochemical and photocatalytic performance of photoelectrodes.

5.2.4. Photocatalytic Activity

The photocatalytic activity of Bi_2WO_6 film has been evaluated by degradtion of rhodamine B (RhB) as the target pollutant. Figure 60 shows the Photocatalytic degradation of RhB over Bi_2WO_6 prepared at different calcination temperature, 525^{o}C, 500^{o}C, 475^{o}C, and 450^{o}C. It can be seen from figure 60a that, complete degradation of RhB is achieved in 45min for the film annealed at 525^{o}C. The photoactivity starts to decrease with decreasing in annealing temperature. The minimum photocatalytic activity is obtained by the film annealed at 450^{o}C as shown in figure 60d.

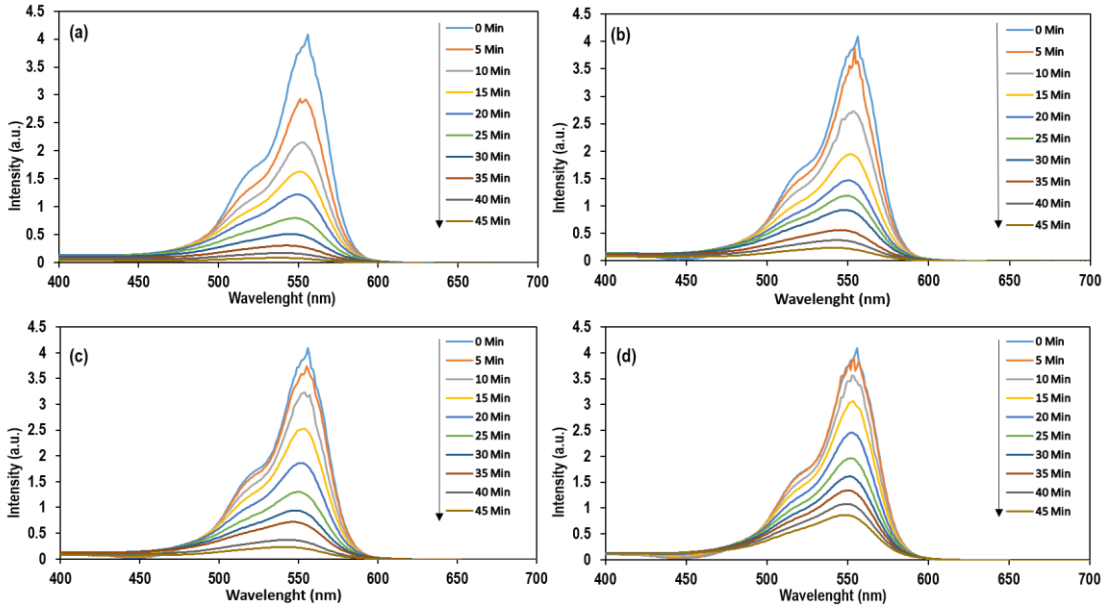

Figure 60: Photocatalytic degredation of RhB over Bi_2WO_6 prepared at different calcination tempreture, (a) 525°C, (b) 500°C, (c) 475°C, (d) 450°C.

Figure 61, shows the photocatalytic activity of Bi_2WO_6 films prepared at different temperatures at the wavelength of 554nm as a function of C/C_o *vs.* irradiation time. It is observed that calcination temperaure has a significant impact on the photocatalytic activity of as-prepared films. It is reported that increasing the annealing temperature lead to increase the crystallinity of the film and that may be the possible reason for the enhancement of the photocatalytic activity.[24,25] The dye degradation study prove that the light-harvesting performance is directly related to the texture, morphology and preferred orientation of photoelectrodes.

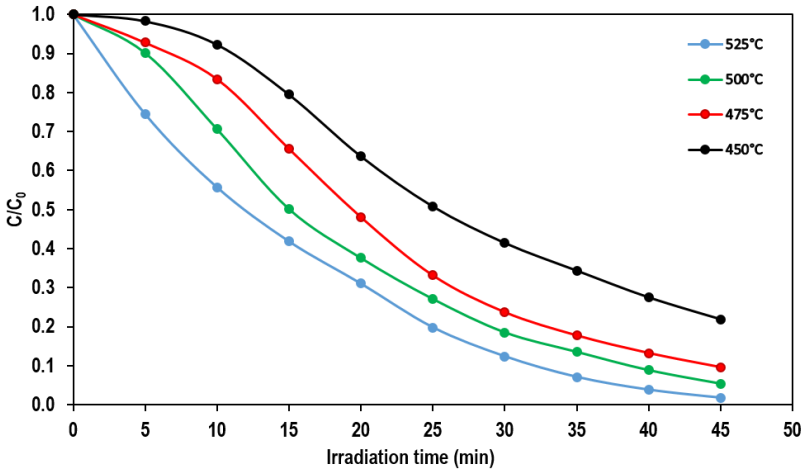

Figure 61: The plot of C/C_0 vs. the irradiation time of Bi_2WO_6 films prepared at different calcination temperatures.

5.3. Summary of Bi_2WO_6 by SP Method

In this work, a single solution source is used to fabricate Bi_2WO_6 photoelectrodes with different annealing temperature using a spray pyrolysis process. Bi_2WO_6 has shown high photocatalytic activity and complete degradation of RhB is achieved in 45min. The fabrication method and annealing temperature have a strong influence on the texture, morphology and the photocatalytic activity of Bi_2WO_6. The increasing in annealing temperature leads to increase in the photocatalytic activity. These photoelectrodes are highly reproducible and possess an optical bandgap of ~2.8 eV and exhibit anodic photocurrent. The present work opens new routes to improve the properties of Bi_2WO_6 photoelectrodes by controlling their texture, morphology and orientation. Overall, the methods reported here provide simple and convenient means for modulation of the surface properties of Bi_2WO_6 photoelectrodes. Our findings will trigger exploitation of Bi_2WO_6 photoelectrodes in a wide range of areas such as photocatalytic, electrochemical, photoelectrochemical and electronic applications.

5.4. References

(1) Zhou, Y.; Meng, X.; Tong, L.; Zeng, X.; Chen, X. *Energies* **2016**, *9*, 764.

(2) Zou, Z.; Ye, J.; Sayama, K.; Arakawa, H. *Nature* **2001**, *414*, 625.

(3) Sayama, K.; Nomura, A.; Arai, T.; Sugita, T.; Abe, R.; Yanagida, M.; Oi, T.; Iwasaki, Y.; Abe, Y.; Sugihara, H. *The Journal of Physical Chemistry B* **2006**, *110*, 11352.

(4) Zhang, L.; Fu, H.; Zhang, C.; Zhu, Y. *Journal of Solid State Chemistry* **2006**, *179*, 804.

(5) Sadale, S.; Chaqour, S.; Gorochov, O.; Neumann-Spallart, M. *Materials Research Bulletin* **2008**, *43*, 1472.

(6) Zhang, L.; Wang, W.; Zhou, L.; Xu, H. *Small* **2007**, *3*, 1618.

(7) Zhang, C.; Zhu, Y. *Chemistry of Materials* **2005**, *17*, 3537.

(8) Sun, C.; Wang, Y.; Su, Q. *Chemical Physics Letters* **2018**, *702*, 49.

(9) Dong, G.; Zhang, Y.; Wang, W.; Wang, L.; Bi, Y. *Energy Technology* **2017**, *5*, 1912.

(10) Jiang, Z.; Liang, X.; Zheng, H.; Liu, Y.; Wang, Z.; Wang, P.; Zhang, X.; Qin, X.; Dai, Y.; Whangbo, M.-H. *Applied Catalysis B: Environmental* **2017**, *219*, 209.

(11) Kim, N.; Vannier, R.-N.; Grey, C. P. *Chem. Mater.* **2005**, *17*, 1952.

(12) Li, J.; Zhou, J.; Hao, H.; Li, W.; Liu, G. *New Journal of Chemistry* **2017**, *41*, 6922.

(13) Stevens, F., Université de Liège, Liège, Belgique, **2016**.

(14) Pawar, G. S.; Tahir, A. A. *Scientific reports* **2018**, *8*, 3501.

(15) Eggleston, C. M.; Shankle, A. J.; Moyer, A. J.; Cesar, I.; Grätzel, M. *Aquat. sci.* **2009**, *71*, 151.

(16) Boschloo, G.; Fitzmaurice, D. *J. Phys. Chem. B* **1999**, *103*, 3093.

(17) Ma, D.; Huang, S.; Chen, W.; Hu, S.; Shi, F.; Fan, K. *J. Phys. Chem. C* **2009**, *113*, 4369.

(18) Crane, M.; Frost, R. L.; Williams, P. A.; Theo Kloprogge, J. *J. Raman Spectrosc.* **2002**, *33*, 62.

(19) Maczka, M.; Macalik, L.; Hermanowicz, K.; Kępiński, L.; Tomaszewski, P. *J Raman Spectrosc.* **2010**, *41*, 1059.

(20) Yang, B.; Zhang, Y.; Drabarek, E.; Barnes, P. R.; Luca, V. *Chem. Mater.* **2007**, *19*, 5664.

(21) Zhang, L. W.; Wang, Y. J.; Cheng, H. Y.; Yao, W. Q.; Zhu, Y. F. *Adv. Mater.* **2009**, *21*, 1286.

(22) Fu, H.; Zhang, L.; Yao, W.; Zhu, Y. *Appl. Catal. B: Envir.* **2006**, *66*, 100.

(23) Kudo, A.; Tsuji, I.; Kato, H. *Chem. comm.* **2002**, 1958.

(24) Yu, J.-G.; Yu, H.-G.; Cheng, B.; Zhao, X.-J.; Yu, J. C.; Ho, W.-K. *The Journal of Physical Chemistry B* **2003**, *107*, 13871.

(25) De, R.; Haque, S. M.; Tripathi, S.; Rao, K. D.; Singh, R.; Som, T.; Sahoo, N. *AIP Advances* **2017**, *7*, 095115.

Chapter 6: Fabrication of Bi_2WO_6 Photoelectrodes by AACVD for Methylene Blue (MB) Degradation

Fabrication of nanostructured materials with well-defined shapes and morphology considered a great challenge in materials chemistry and nanotechnology.[1,2] Recently, a noteworthy interest has been acknowledged on controlling the shape and structure of nanostructured materials and that is because of the solid connection between morphology and chemical/physical properties.[3,4] Nanostructured materials with well-design morphologies have been inspiring significant research owing to their important role in the studies of structure-property relationships.[5,6] Well-designed hierarchical structures of given inorganic materials offer novel chemical and physical properties because the structures possess the advantage of both microstructural and nanostructural nature.[7]

Traditional methods for controlling the shape, size and structure are based on two strategies: first is the chemical approach that includes hydrothermal[8], surfactant,[9] and molecular assemblies as soft templates,[10] and so on; the second is the physical strategy which includes thermal evaporation,[11] physical exfoliations,[12].

Among different electrode deposition techniques, aerosol-assisted chemical vapour deposition (AACVD) is simple, possess advantages that a single solution source can be used to fabricate multicomponent electrodes. Significant effort has been made to prepare of Bi_2WO_6 particles by a hydrothermal process and then deposition of electrodes by dip-coating,[13] spin coating,[14] spray pyrolysis,[15] electrostatic layer by the layer deposition technique.[16] However, a few reports have published on the deposition of Bi_2WO_6 electrodes using AACVD in the

literature. Ishikawa *et al*. prepared Bi_2WO_6 thin films by MOCVD using a vertical cold-wall type reactor. Tri-methyl bismuth and pentaethoxy tungstate were used as the Bi and W sources in the presence of O_2 gas as an oxidant.[17]

Bi_2WO_6 has attracted considerable attention for its physical and chemical properties, such as catalytic activity, ferroelectric and piezoelectricity.[18] Recently, people's attention has been focused on the Bi_2WO_6 due to its successful uses as a photocatalyst[19] and as a semiconductor material in photoelectrochemical (PEC) water splitting[20-24] and in CO_2 reduction.[25]

In this work, Bi_2WO_6 nanostructured electrodes with different textures and morphologies such as compact, porous, nanoplates and buckyball-shaped hierarchical microsphere structures are fabricated by expediently controlling the process parameters of Aerosol Assisted Chemical Vapor Deposition (AACVD). These novel methods are a simple and reproducible route to construct nanostructured Bi_2WO_6 electrodes. Furthermore, the photoelectrodes prepared in this work has shown high activity for photocatalytic degradation of Methylene Blue (MB) dye. Our findings will undoubtedly have a significant impact on further development of Bi_2WO_6 as a potential semiconductor material in solar energy conversion and photocatalytic applications.

6.1. Results and Discussion

Nanostructured thin films of Bi_2WO_6 were successfully prepared through a simple one-step approach employing spray pyrolysis and AACVD processes. The effect of annealing/deposition temperature on the morphology and PEC properties of the thin films has been studied.

6.1.1. Characterization

Effect of annealing/ deposition temperature on crystallinity and morphology

To investigate the effect of deposition temperature on structure and morphology, electrodes were deposited at different temperatures from solution by AACVD. The XRD patterns of Bi_2WO_6 electrodes deposited at different temperatures with their respective morphology and structure are given in Figure 62. The effect of temperature on crystallinity was demonstrated through the systematic change of the XRD patterns. The reflection pattern became more clean-cut and the peak intensities gradually increased, indicating better crystallinity with the increase of substrate temperatures from 425 - 500 ºC. The unidentified peaks present in the XRD pattern (Figure 61) of the electrode deposited at 425 °C disappeared with the increase of substrate temperature indicating that these peaks may be correspond to un-decomposed materials.

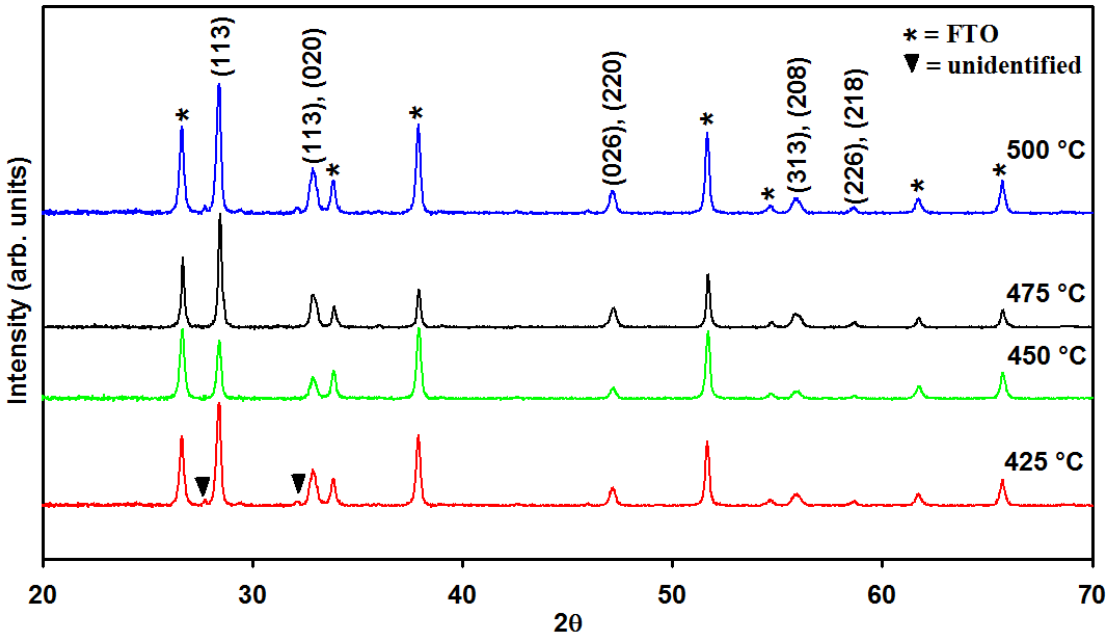

Figure 62: The XRD peak pattern of electrodes deposited by AACVD at deposition temperature of 425- 500°C.

The SEM micrograph of the electrode (Figure 63) indicates a dense homogeneously dispersed microstructure without any distinguishable features. As shown in Figure 63b, nanoplates started to emerge from the dense microstructures, when the deposition temperature is increased to 450 °C. It is also evident from Figure 63b that the size and shape of nanoplates are not well defined although long edges were clearly visible. When the deposition temperature was further increased to 475 °C, the electrode morphology showed specific plate-like features with short edges. Further increase in deposition temperature to 500 °C resulted in large and thin nanoplates. The length of the edge of an average nanoplate is about 110 nm and the thickness is about 10 nm. As shown in the Figure 63d the nanoplates emerged from the substrate are aligned almost perpendicular to the FTO substrate.

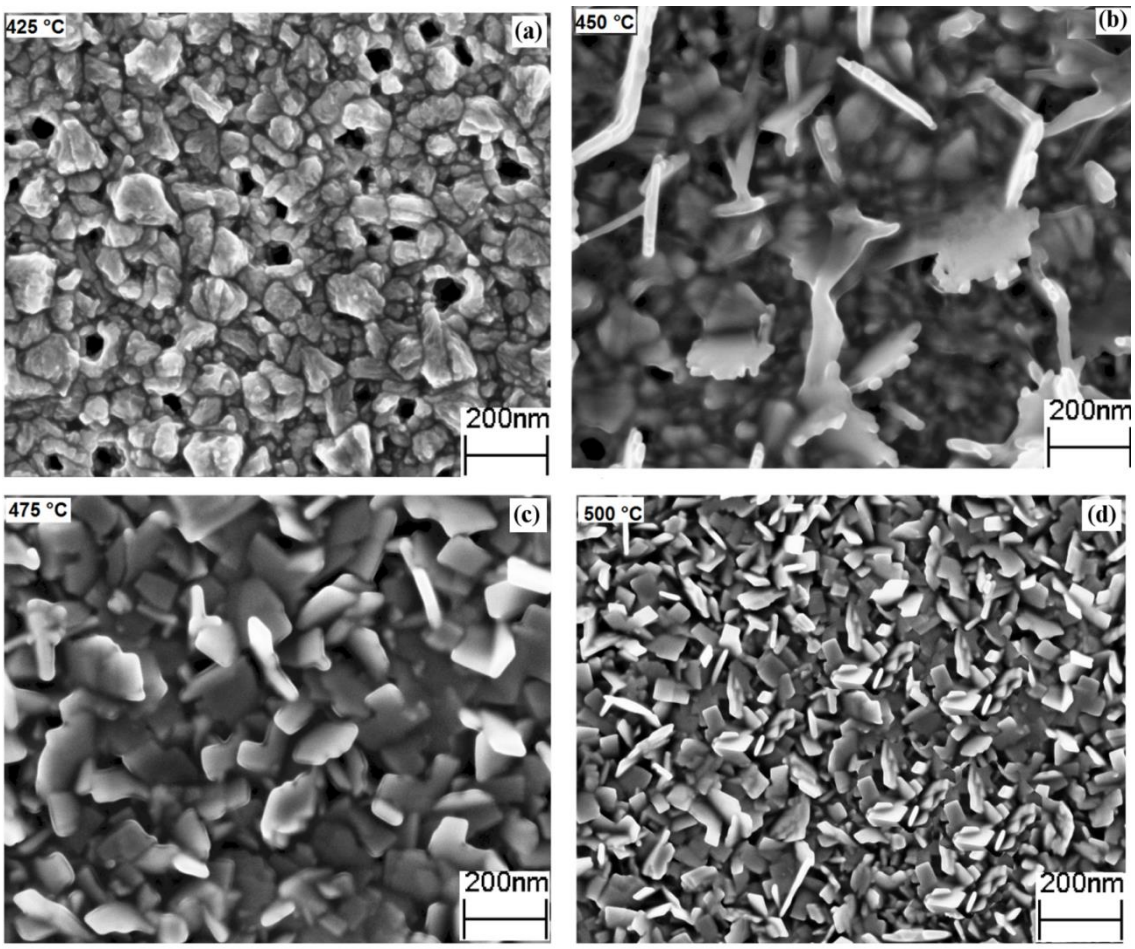

Figure 63: The SEM of electrodes deposited by AACVD at deposition temperature of 425- 500°C.

Effect of Carrier Gas on morphology

Although the carrier gas flow can potentially influence the deposition temperature due to the cooling effect, the change of carrier gas flow had no pronounced effect on the morphology of electrodes deposited below 500 °C. Surprisingly, increasing the deposition temperature to 500 °C and simultaneously reducing the carrier gas flow to 100 mL/min resulted in the formation of a hierarchical buckyball-like microsphere structured electrodes (Figure 64). Further SEM analysis (Figure 64a or 64c) showed that the buckyball-like microsphere structure covers almost the entire FTO surface constructing a very uniform electrode of Bi_2WO_6. The close-up view of an individual sphere (Figure 64b) indicates that the Bi_2WO_6 possesses superstructures with buckyball-like

appearance. These microspheres have a diameter ranging from 0.4 to 0.8 μm. Interestingly, the superstructures are built from two-dimensional nanoparticles with a thickness of about 10 - 30 nm, which can be vividly demonstrated from the SEM images. The surfaces of these microspheres are coarse and have many individual nanoparticles. The SEM images also reveal that these nanoparticles are aligned perpendicularly to the spherical surface with clearly oriented layers, pointing toward a common centre within the buckyball-like microstructure (Figure 64b). More importantly, the microspheres have many pores with different diameter sizes, which may have the potential to provide improved the physicochemical properties or serve as transport paths for small molecules. Among the microspheres, one can easily see some nanoplates formed on the surface of the FTO (Figure 64a & b), which suggests a two-stage growth process of Bi_2WO_6 microspheres. The primary stage is the formation of nanospheres/nanoplates and then these nanoplates self-assembled to form microsphere structures, which is a common phenomenon in the formation of microspheres in the hydrothermal process.[5,26] A cross-section of the electrode (Figure 64c) showed the growth of the Bi_2WO_6 hierarchical structures on top of each other, increasing the thickness of the electrode up to 3 μm. The cross-section image further confirmed that each microsphere is about 0.4 - 0.8 μm in diameter.

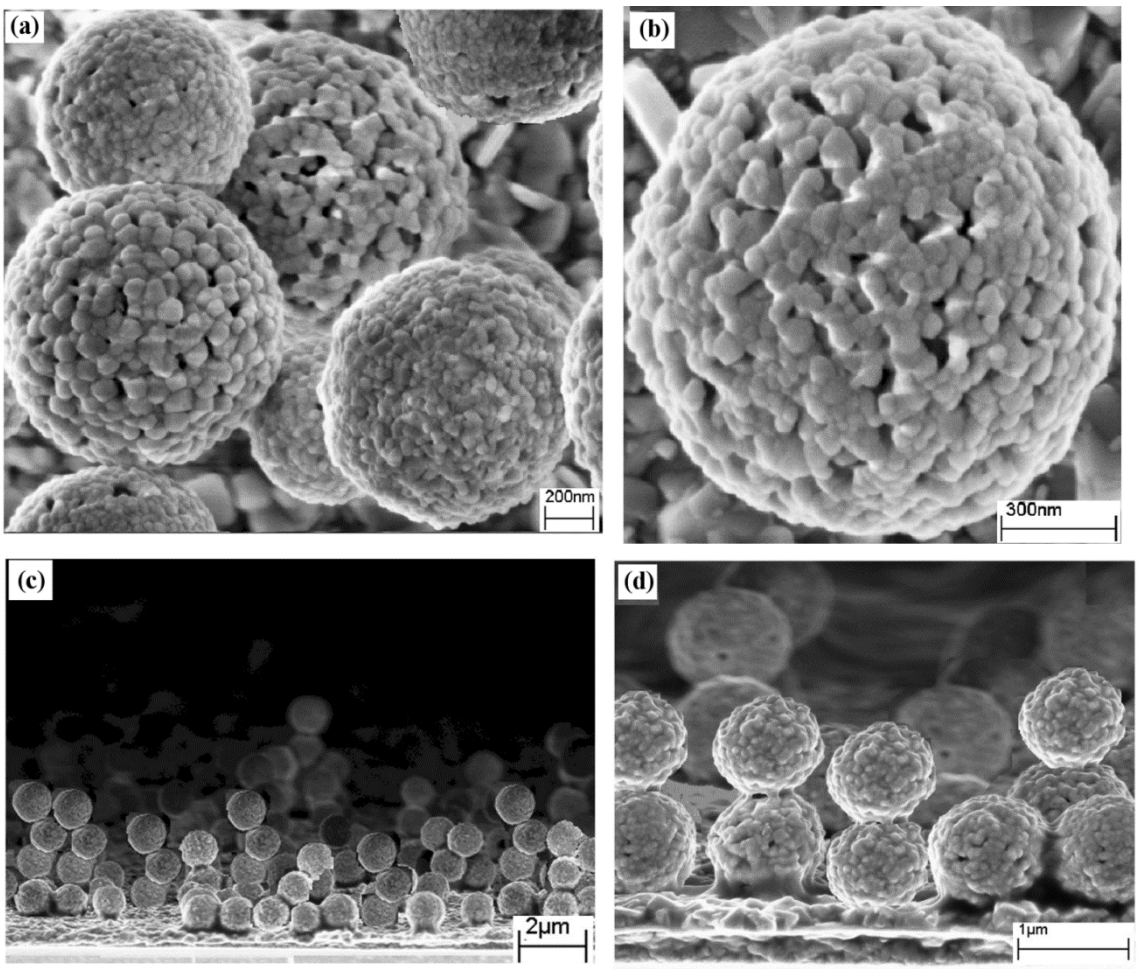

Figure 64: The SEM hierarchical buckyball-like microsphere structured of electrodes deposited by AACVD at deposition temperature of 500°C: (a) and (b) surface morphology, (c) and (d) cross section of the electrodes.

Mechanism of Formation of Nanoplates and growth of Hierarchical microsphere by AACVD

Formation of Bi_2WO_6 nanoplates and hierarchical microsphere structures by the hydrothermal process has been already explained on the basis of the various characteristic times: residence time, reaction time of the precursor and sintering time.[27,28] Similarly, in our work changing in sintering time behavior play a multifold role in the growth of Bi_2WO_6 nanoplates and hierarchical buckyball-like microsphere structures.

During the deposition process, aerosol droplets travel through different temperature zones, the first step is the evaporation of solvent molecules and the

second step is the vaporization of the precursor. As a results, two different deposition regimes of vapor-particle and particle dominant were obtained. If the residence time is equal to the reaction time, then a mixed particle-vapor mixture deposits onto the substrate, resulting in the formation of nanoplates structured films (scheme A in Figure 65). It can be seen from the XRD diffraction pattern that the nanoplates morphology was polycrystalline anatase, with grains that were about 10 nm to 30nm in size.

On the other hand, if the reaction time is less than the residence time, then a particle dominant regime is formed, resulting in the growth of particles in the gas phase of the reaction zone, followed by deposition onto the substrate. The continuous follow of gases may help these nanoparticles to spin along the c-axis to build hierarchical microsphere structures (scheme B in Figure 65). The formation of hierarchical microsphere structures over the top of each other (Figure 64d) is a clear evidence for the nucleation and formation of nanoparticles in vapour phase before they plunge on to the substrate.

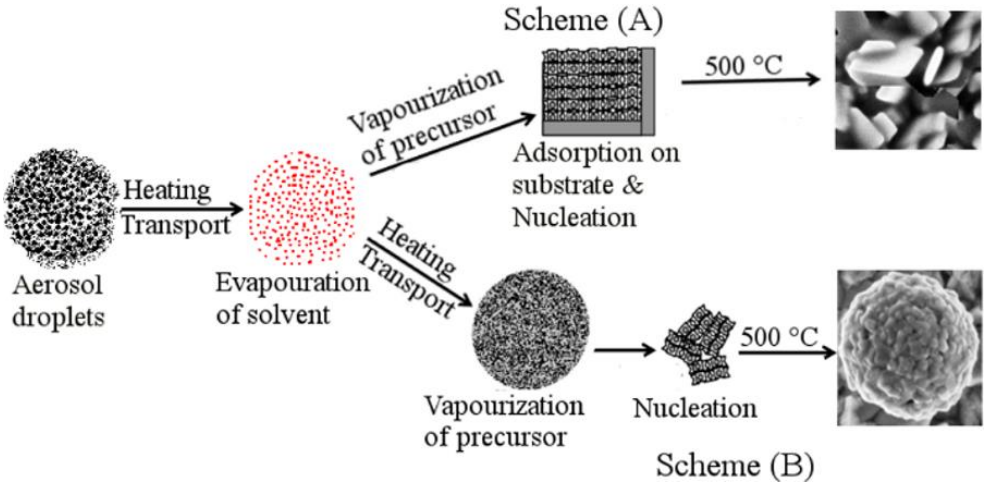

Figure 65: A schematic illustration of possible growth process of nanoplate-like hierarchical buckyball-like microsphere structures formation during AACVD process.

6.1.2. Photoelectrochemical Analysis

The photoelectrochemical properties of Bi_2WO_6 electrodes were investigated under AM 1.5 illumination in a 3-electrode open quartz cell. The steady-state *J*-V plots in Figure 66 show the dependence of photocurrent density on the deposition temperature for each set of electrodes. Generally, for all electrodes the photocurrent increases with the increase of annealing/deposition temperature. The present results, therefore, confirm that there is a strong dependence of photocurrent on the deposition/annealing temperature. The crystallite size, orientation and morphology of the electrodes drastically varied with the annealing/deposition temperature. For all electrodes, the increase of deposition and annealing temperature improved the photocurrent density. Further increased of deposition/annealing temperature could not be continued beyond a certain limit due to the instability of glass substrate at high temperature (>550 °C), premature decomposition of aerosol and film adherence issues experienced at high temperatures.

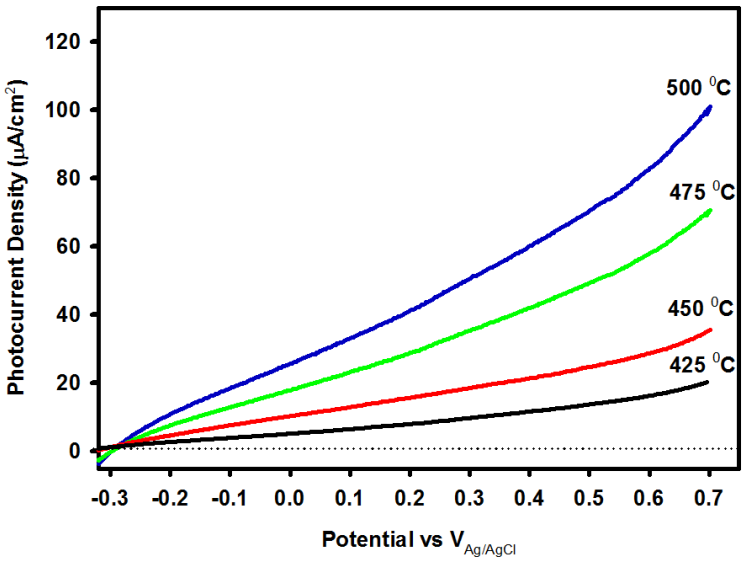

Figure 66: J-V plots showing the dependence of photocurrent on electrode preparation temperature for the electrodes deposited by AACVD from solution.

Generally, the textural properties ,as well as the degree of crystallographic preferred orientation, are the key factors in defining the light harvesting and charge transfer properties.[29] In the case of Bi_2WO_6 electrode deposited by AACVD, the photocurrent increased rapidly with the applied potential, which could be due to the fact that the high internal surface area exposed to the electrolyte provides a large effective semiconductor/electrolyte interface. Thus, the separation of photogenerated carriers within the width of the space charge layer becomes a key factor.

The best photoelectrodes prepared AACVD methods have been studied under chopped light (AM 1.5 illumination) in order to reveal the dark current simultaneously. Figure 67 describes the photocurrent transients for electrodes deposited at 500°C with a different carrier gas. For comparison, the steady-state *J-V* plot was superimposed on the transient plot in each case. Steady-state and transient *J-V* plots agree well for all electrodes. The electrode deposited at 500°C with a high carrier gas (300 mL/min) has shown about 40 μAcm^{-2} photocurrent density at 0.23 V (Figure 67a). The electrode deposited with a low carrier gas (100 mL/min) has shown about 67 μAcm^{-2} photocurrent density at 0.23 V (vs Ag/AgCl/3M KCl) under AM1.5 illumination and a negligible dark current (Figure 67b) which is among the highest photocurrent density for Bi_2WO_6 electrodes reported in this work. The photocurrent onset of this electrode had a further negative shift (by about 0.5 V compared to the flat Bi_2WO_6 electrodes) which is one of the key findings of this work. This can be attributed to the hierarchical microsphere structures and preferred orientation along (001) plane. The considerable negative shift of the photocurrent onset associated with preferred orientation along (001) plane provides a route to engineering the energetic and interfacial charge transfer properties at Bi_2WO_6 electrode/electrolyte interface.

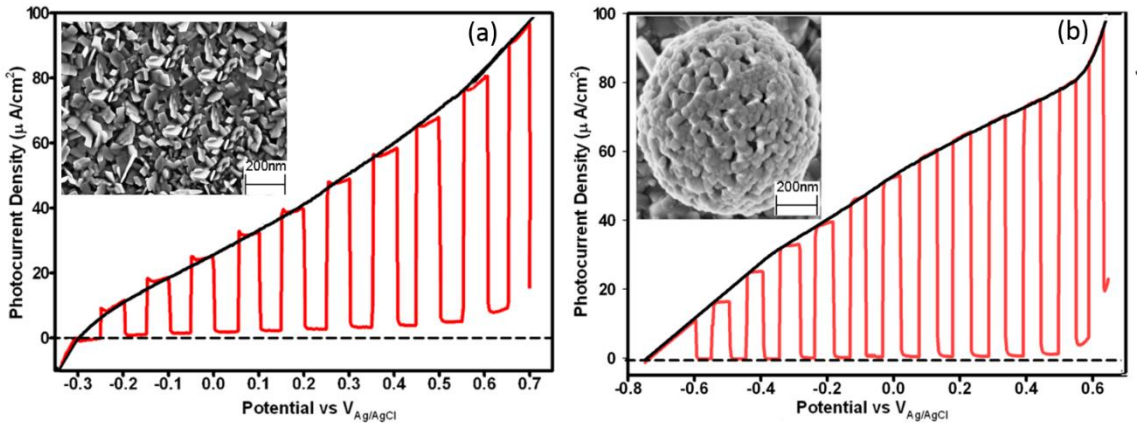

Figure 67: Current–voltage characteristics for Bi_2WO_6 electrodes deposited by AACVD at 500°C, (a) nanoplate-like electrode deposited at low carrier gas. (b) Hierarchical buckyball-like microsphere structured electrode deposited at high carrier gas.

This finding can have a significant influence on studies of processes at electrode/electrolyte interface. Along with the preferred crystallographic orientation, the hierarchical microsphere structures have numerous microspores and a high internal surface area which allows more electrolyte solution to penetrate to the interior of each microsphere providing a large semiconductor/electrolyte interface.

6.1.3. Optical and Electrochemical Measurements

It has been reported that Bi_2WO_6 thin films have a steep absorption edge in the visible range, indicating that it is due to the intrinsic transition within the material related to the fundamental absorption edge rather than the transition from impurity levels.[30] The optical properties of Bi_2WO_6 samples were recorded using UV/Vis spectroscopy.

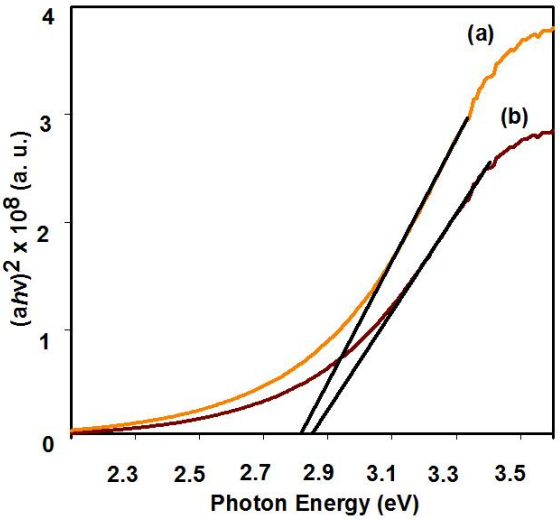

Figure 68: Plot of $(\alpha h\nu)^2$ versus photon energy (hv) for Bi_2WO_6 electrodes (a) for hierarchical buckyball-like microsphere structured electrode deposited by AACVD at 500°C (b) for squarer shaped nanoplates electrode deposited by AACVD at 500 °C.

Figure 68 shows direct bandgap of thin films for Bi_2WO_6 film electrodes (a) for hierarchical buckyball-like microsphere structures electrode deposited by AACVD at 500 °C, (b) for nanoplate-like electrode deposited by AACVD at 500 °C. For a crystalline semiconductor, it was shown that the optical absorption near the band edge follows the equation;

$$(\alpha h\nu)^n = A(h\nu - E_g) \qquad (10)$$

where α, v, E_g, and A are light absorption coefficient, frequency, bandgap, and a constant, respectively. Among them, n decides the characteristics of the transition in a semiconductor. Bi_2WO_6 is a direct bandgap material. The bandgap (E_g) of the electrodes were estimated by extrapolation of the plots of $(\alpha h\nu)^2$ versus $h\nu$ are 2.81 and 2.85,eV respectively (Figure 68), and are comparable to the reported values for Bi_2WO_6 powder nanoparticles.[5]

6.1.4. Photocatalytic Activity

Photocatalytic activity of Bi_2WO_6 film was evaluated by measuring the

degradation of methylene blue (MB), under UV light irradiation of 0 min, 10 min, 20 min, 30 min, 40 min and 50 min. For comparison, two Bi_2WO_6 photoelectrodes prepared at 500°C with different carrier gas flow have experimented under the same condition as shown in Figure 69. The maximum absorption peaks of MB were reported at 653nm. Figure 70, shows the photocatalytic activity of Bi_2WO_6 films prepared at different carrier gas flow as a function of C/C_o vs. irradiation time.

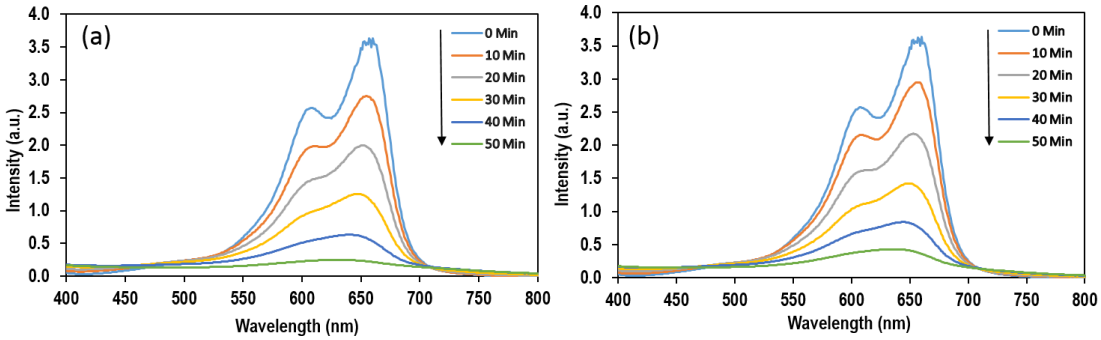

Figure 69: Photocatalytic degredation of MB over Bi_2WO_6 prepared at 500°C with different carrier gas flow, (a) 100mL/min, (b) 300mL/min.

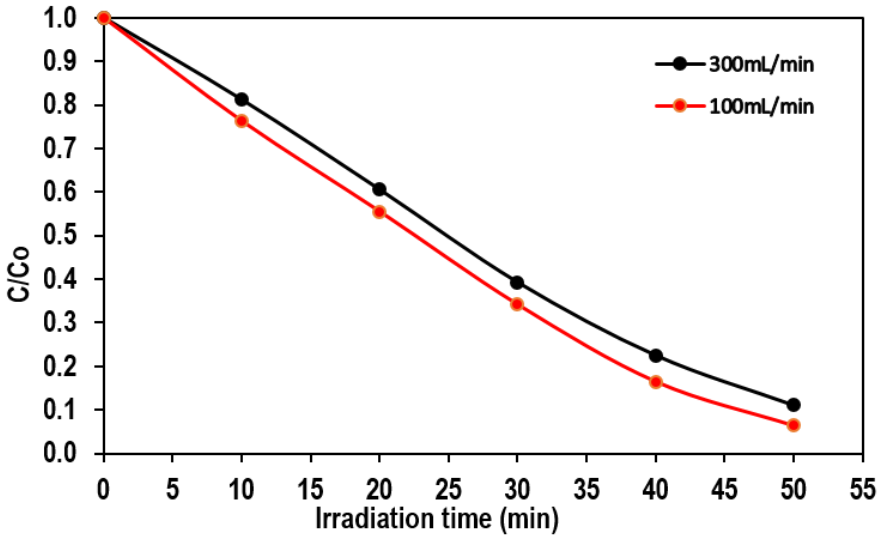

Figure 70: The plot of C/C_0 vs. the irradiation time of Bi_2WO_6 films prepared at different carrier gas flow.

It is observed that the degradation efficiencies of Bi_2WO_6 photoelectrode increased with increasing of calcination temperature as discussed before in

section 4.3.3.4 using the spray method. In addition, It is reported that increasing the calcination temperature lead to increase the crystallinity of the film and that may be the possible reason for the enhancement of the photocatalytic activity.[31,32] As discussed before, film prepared by AACVD using low carrier gas flow resulted in the formation of a hierarchical buckyball-like microsphere structured electrodes which has the highest photocurrent amongst other electrodes. Here, the effect of carrier gas flow on photocatalytic activity of the electrodes has been investigated. Two electrodes prepared with 100mL/min and 300mL/min carrier gas flow were used in this study. Figure 69a shows highest degradation efficiency of MB achieved by electrode prepared at low carrier gas flow compared to the one prepared at high carrier gas flow as shown in figure 69b. As shown in Figure 70, hierarchical microsphere structures electrode showed much better photocatalytic activities than the nanoplate-like electrode. It could be seen that changing the carrier gas flow has a significant impact on the photocatalytic activity of the prepared films. Moreover, the catalytic performance of Bi_2WO_6 is strongly affected by the shape of the Bi_2WO_6 catalyst.[33] The photodegradability study proves that the photocatalytic performance is directly related to the texture, morphology and preferred orientation of photoelectrodes.

6.2. Summary of Bi_2WO_6 by AACVD Method

In this work, the aerosol-assisted chemical vapour deposition (AACVD) method can be used to deposit complex ternary metal oxide semiconductor films of Bi_2WO_6. These thin film electrodes are highly reproducible and posse an optical bandgaps of (2.8-2.9) eV and exhibit anodic photocurrent. The deposition method, deposition solution, annealing/deposition temperature and carrier gas flow have a strong influence on the Bi_2WO_6 films. Bi_2WO_6 photoelectrodes prepared by AACVD using low carrier gas flow shows the highest degradation

efficiency of MB. Hence, the current work offers simple methodologies of controlling the texture of Bi_2WO_6 films.

In general, present work opens up a new route to improve the physical and chemical properties of Bi_2WO_6 by controlling the texture that will eventually allow the utilization of Bi_2WO_6 in catalytic electrochemical, photoelectrochemical and electronic applications. For example, photoelectrochemical properties of Bi_2WO_6 thin film electrodes can be significantly enhanced by systematically controlling their texture. The following specific conclusions can also be drawn from the present work.

(1) Hierarchical microsphere structures and structured Bi_2WO_6 thin films can easily be deposited using AACVD by controlling the temperature and carrier gas flow.

(2) The results clearly show that highly ordered morphology and higher porosity give a high photocurrent at low bias potential. The films deposited by AACVD have shown a considerable shift of the photocurrent onset potential (up to -0.5 V vs Ag/AgCl/3M KCl) with the decrease of carrier gas flow. This finding will undoubtedly have a significant influence on further exploitation of Bi_2WO_6 as a potential semiconductor material in solar energy conversion applications.

(3) Our results suggest that film texture is a major factor in determining the performance of the Bi_2WO_6 films, and the methods reported here provides a simple and convenient means for modulation of surface properties of Bi_2WO_6 thin films.

6.3. References

(1) Niu, K.; Yang, J.; Kulinich, S.; Sun, J.; Li, H.; Du, X. *J. Am. Chem. Soc.* **2010**, *132*, 9814.

(2) Amano, F.; Nogami, K.; Ohtani, B. *J. Phys. Chem. C* **2009**, *113*, 1536.

(3) Buonsanti, R.; Grillo, V.; Carlino, E.; Giannini, C.; Gozzo, F.; Garcia-Hernandez, M.; Garcia, M. A.; Cingolani, R.; Cozzoli, P. D. *J. Am. Chem. Soc.* **2010**, *132*, 2437.

(4) Whang, D.; Jin, S.; Wu, Y.; Lieber, C. M. *Nano Lett.* **2003**, *3*, 1255.

(5) Zhang, L.; Wang, W.; Zhou, L.; Xu, H. *Small* **2007**, *3*, 1618.

(6) Kuang, D.; Brezesinski, T.; Smarsly, B. *J. Am.Chem. Soc.* **2004**, *126*, 10534.

(7) Wang, Y.; Zhu, Q.; Zhang, H. *J. Mater. Chem.* **2006**, *16*, 1212.

(8) Tian, Y.; Chang, B.; Lu, J.; Fu, J.; Xi, F.; Dong, X. *ACS appl. Mater. interfaces* **2013**, *5*, 7079.

(9) Chen, S.; Fan, Z.; Carroll, D. L. *J. Phys. Chem. B* **2002**, *106*, 10777.

(10) Li, Y.; Liu, J.; Huang, X.; Li, G. *Crystal growth & design* **2007**, *7*, 1350.

(11) Liang, C.; Shimizu, Y.; Sasaki, T.; Umehara, H.; Koshizaki, N. *J. Phys. Chem. B* **2004**, *108*, 9728.

(12) Gautam, U. K.; Vivekchand, S.; Govindaraj, A.; Kulkarni, G.; Selvi, N.; Rao, C. *J. Am. Chem. Soc.* **2005**, *127*, 3658.

(13) Zhao, X.; Wu, Y.; Yao, W.; Zhu, Y. *Thin Solid Films* **2007**, *515*, 4753.

(14) Li, J.; Zhang, X.; Ai, Z.; Jia, F.; Zhang, L.; Lin, J. *J. Phys. Chem. C* **2007**, *111*, 6832.

(15) Mann, A. K.; Skrabalak, S. E. *Chem. Mater.* **2011**, *23*, 1017.

(16) Zhang, S.; Shen, J.; Fu, H.; Dong, W.; Zheng, Z.; Shi, L. *J. solid state chem.* **2007**, *180*, 1456.

(17) Ishikawa, K.; Watanabe, T.; Funakubo, H. *Thin solid films* **2001**, *392*, 128.

(18) Kim, N.; Vannier, R.-N.; Grey, C. P. *Chem. Mater.* **2005**, *17*, 1952.

(19) He, D.; Wang, L.; Xu, D.; Zhai, J.; Wang, D.; Xie, T. *ACS Appl. Mater. Interfaces* **2011**, *3*, 3167.

(20) Zhang, C.; Zhu, Y. *Chem. Mater.* **2005**, *17*, 3537.

(21) Saison, T.; Gras, P.; Chemin, N.; Chanéac, C.; Durupthy, O.; Brezova, V.; Colbeau-Justin, C.; Jolivet, J.-P. *J. Phys. Chem. C* **2013**, *117*, 22656.

(22) Yan, Y.; Wu, Y.; Yan, Y.; Guan, W.; Shi, W. *J. Phys. Chem. C* **2013**, *117*, 20017.

(23) Osterloh, F. E. *Chem. Mater.* **2007**, *20*, 35.

(24) Shang, M.; Wang, W.; Ren, J.; Sun, S.; Wang, L.; Zhang, L. *J. Mater. Chem.* **2009**, *19*, 6213.

(25) Zhou, Y.; Tian, Z.; Zhao, Z.; Liu, Q.; Kou, J.; Chen, X.; Gao, J.; Yan, S.; Zou, Z. *ACS Appl. Mater. Interfaces* **2011**, *3*, 3594.

(26) Ma, D.; Huang, S.; Chen, W.; Hu, S.; Shi, F.; Fan, K. *J. Phys. Chem. C* **2009**, *113*, 4369.

(27) Thimsen, E.; Rastgar, N.; Biswas, P. *The Journal of Physical Chemistry C* **2008**, *112*, 4134.

(28) An, W.-J.; Thimsen, E.; Biswas, P. *The Journal of Physical Chemistry Letters* **2009**, *1*, 249.

(29) Yang, B.; Zhang, Y.; Drabarek, E.; Barnes, P. R.; Luca, V. *Chem. Mater.* **2007**, *19*, 5664.

(30) Kudo, A.; Tsuji, I.; Kato, H. *Chem. comm.* **2002**, 1958.

(31) Yu, J.-G.; Yu, H.-G.; Cheng, B.; Zhao, X.-J.; Yu, J. C.; Ho, W.-K. *The Journal of Physical Chemistry B* **2003**, *107*, 13871.

(32) De, R.; Haque, S. M.; Tripathi, S.; Rao, K. D.; Singh, R.; Som, T.; Sahoo, N. *AIP Advances* **2017**, *7*, 095115.

(33) Zhang, H.; Zhang, H.; Zhu, P.; Huang, F. *ChemistrySelect* **2017**, *2*, 3282.

Chapter 7: Fabrication of α-Fe_2O_3 Counter Electrodes for Dye- Sensitized Solar Cells

This section is based on collaborative work with another group member. The aim of this work is to fabricate Fe_2O_3 films and use it as counter electrodes for dye-sensitized solar cells in order to compete for platinum counter electrode. My contribution in this work is to fabricate Fe_2O_3 counter electrodes and performed characterization and PEC measurements of the prepared electrodes. To do that, two different deposition techniques have been used: spray pyrolysis (SP) and aerosol assisted chemical vapour deposition (AACVD).

7.1. Introduction

During the past two decades, tremendous efforts have been dedicated to the so-called third generation of solar cells represented by dye-sensitized solar cells (DSSCs), because this type of cells offers compatibility with flexible substrates, low cost, easy fabrication, environmental friendliness and high energy conversion efficiency which allows them to compete with traditional silicon-based solar generation.[1-3] In general, a DSSC comprises a dye-sensitized TiO_2 photoanode, an electrolyte containing the iodide/triiodide (I^-/I_3^-) redox couple, and a counter electrode (CE). As an important component of DSSC, the counter electrode plays a pivotal role in terms of the collection of electrons from the external circuit and then injecting electrons into the electrolyte to reduce the reduction of redox species used as a mediator in regenerating the dye.[4,5]

In order to achieve the functional design, the efficient reduction of iodine /triiodide redox couples and high electrical conductivity for transport electrons are required for finding benchmark counter electrode (CE) materials. Traditionally,

platinum (Pt) has been confirmed as a superior CE material for the DSSC due to its excellent catalytic activity and high electrical conductivity.[6,7] However, the high cost of Pt as a noble metal and its poor stability limits its application in DSSCs. Therefore, it is of crucial importance to explore alternative materials with low-cost, high electronic conductivity and good electrical stability without sacrificing the DSSCs photovoltaic performances.

To overcome these challenges, various alternative materials such as carbon-based materials,[8,9] conductive organic polymers,[10-12] inorganic compounds,[13-15] metal oxides,[16] metal carbides,[17] metal nitrides [18] and transition metal sulphides[19] have been investigated to replace Pt-based electrodes in DSSCs. However, compared to Pt, the performance of those electrode materials is still limited by their poor thermal stability and low electron conductivity, thus leading to the inferior performance.[20-22]

Due to its good conductivity, the low cost, nontoxicity and high abundance, α-Fe_2O_3 has superiority over other electrode materials. α-Fe_2O_3, which is an n-type semiconductor with an indirect band gap of 2.1 eV, has received much attention as a promising material with many applications in photoelectrochemical devices,[23] photocatalysts,[24] gas sensor,[25] pigment.[26] Previous research shows several types of α-Fe_2O_3 nanostructure were used in DSSC applications. It has been found that the α-Fe_2O_3 NPs can exhibit almost identical adsorption energy of I compared to that of Pt, which makes it the most promising inorganic material for DSSCs.[27] However, the obtained efficiency was still lower than that of Pt as CE because of the poor electron transport efficiency across α-Fe_2O_3 nanoparticles.[28] Hybrid α-Fe_2O_3 flower-like morphology has been reported as a working electrode in DSSC which contribute 1.8% power conversion efficiency.[29] Recently, biohybrid hematite and titanium oxide (TiO_2) nanostructure thin film was

used as an anodic component in biohybrid DSSC.[30] However, the solar conversion efficiency of this photoanode is below that required for practical use.

Herein, nanostructured α-Fe_2O_3 photoanodes have been fabricated using different fabrication methods such as spray pyrolysis (SP) and aerosol assisted chemical vapour deposition (AACVD). The performance of these nanostructures was examined as photoanodes in DSSC and compared to the Pt counter electrodes.

7.2. Experimental

7.2.1. Preparation of α-Fe_2O_3 Counter Electrode

Preparing of Precursor Solution

In a typical experiment, 0.4g of iron (III) acetylacetonate Fe $(acac)_3$ were dissolved in 100ml ethanol containing 7mL of trifluoroacetic acid (TFA) under magnetic stirring.

Fabrication of α-Fe_2O_3 counter electrode by SP

Spray pyrolysis deposition techniques described in section 3.4 were used to fabricate α-Fe_2O_3 counter electrode. Fluorine-doped tin oxide (FTO) glass was used as a substrate. The precursor solution was sprayed at 375^{o}C via a syringe pump (New Era Pump Systems NE-1000), an ultrasonic atomizer nozzle (Sonozap) 1mm diameter and a vortex attachment. A certain amount of prepared solution was sprayed on to the FTO at a rate of 1mlmin^{-1} assisted with compressed air at a rate of 4Lmin^{-1}.

Fabrication of α-Fe_2O_3 counter electrode by AACVD

AACVD deposition method described in section 3.5 was used to fabricate α-Fe_2O_3 counter electrode at 500°C. Fluorine-doped tin oxide (FTO) glass was used

as a substrate in this work. In brief, 25 mL of α-Fe_2O_3 precursor solution was taken in a 20 mL round-bottom flask and placed above the ultrasonic generator. Air at a flow rate of 120 mL/min was used as the carrier gas to transfer the generated aerosol from the solution flask to the trapped flask. The aerosol of fine droplets was transferred into the heated substrate placed on the hotplate surface by another carrier gas with a flow rate of 300ml/min. The substrate was heated up to the deposition temperature for 20 min brier to the deposition starts.

7.2.2. Characterization

X-ray diffraction (XRD) was acquired using Siemens D5000 diffractometer using a Cu Kα radiation. 40kV/ 40mA, 0.02 $^{o}2\theta$ step and a scan time of 2.5 seconds per step) in the range of 20-80 $^{o}2\theta$. The surface morphology and composition of the thin film was characterized using a high-resolution scanning electron microscope (SEM, TESCAN VEGA3).

7.2.3. Photoelectrochemical Measurements

The photoelectrochemical (PEC) measurements of α-Fe_2O_3 electrode were acquired in 0.1 M NaOH electrolyte (pH 13) using Metrohm Autolab potentiostat under chopped light using a 100 W ozone free Xenon lamp equipped with an AM 1.5 filter (Oriel LCS-100, Newport). The light intensity was 1 sun illumination (100 mW cm^{-2}). A liner sweep voltammetry (LSV) was scanned in the negative to the positive direction between the ranges of -0.3 V to +0.7 V vs Ag/AgCl. All the potentials described in this study refer to the reversible hydrogen electrode (RHE) potential, which was calculated according to following the formula: $V_{RHE} = V_{Ag/Agcl} + 0.197+0.059*pH$.

7.2.4. DSSC Fabrication

The DSSC solar device was fabricated by another collaborated member according to the literature procedure.[31] Briefly, a layer of transparent TiO_2 paste was coated on the conductive glass (FTO) by screen printing as a working electrode. The thickness of TiO_2 working electrode was controlled by controlling the number of TiO_2 layers coated on the FTO. The prepared films were annealed at 450°C in order to remove the organic particles. The prepared TiO_2 films were immersed into 0.2mM N719 dye in ethanol at room temperature for 12-15h. The iodide/tri-iodide electrolyte was prepared and stirred for 24h at room temperature. Pt counter electrode was placed over the dye-adsorbed TiO_2 electrode with a 25µm hot-melt spacer between two electrodes. The electrolyte was introduced into the cell through the small hole drilled in the counter electrode. The hole in the counter electrode was sealed with a film (Meltonix-solaronix) and a piece of cover glass. To be compared with conventional platinum counter electrodes, this procedure was repeated with α-Fe_2O_3 as a counter electrode.

7.2.5. Device Characterization

The device was tested in an indoor controlled environment using setup consists of a solar simulator which is a light source from a xenon lamp and an I-v tracer which is used to characterise the electrical performance of the solar cell. The photovoltaic performance of the assembled device was measured under 1000W/m2 of light from a Wacom AAA continuous solar simulator (model: WXS-210S-20, AM1.5G). The I-V characteristics of the device were recording using EKO MP-160i I-V Tracer.

7.3. Results and Discussion

7.3.1. Characterization

To investigate the effect of deposition method on structure and morphology, α-Fe_2O_3 electrodes were deposited by AACVD and SP deposition methods. The XRD patterns of α-Fe_2O_3 electrodes deposited by these deposition methods with their respective morphology and structure are given in Figure 71. The effect of deposition technique on crystallinity was demonstrated through the systematic change of the XRD patterns. Figure 71a shows that the reflection pattern became more clean-cut and the peak intensities gradually increased, indicating better crystallinity of electrode deposited by AACVD. The unidentified peaks present in the XRD pattern (Figure 71b) of the electrode deposited by SP disappeared in electrode deposited by AACVD indicating that these peaks may correspond to un-decomposed materials.

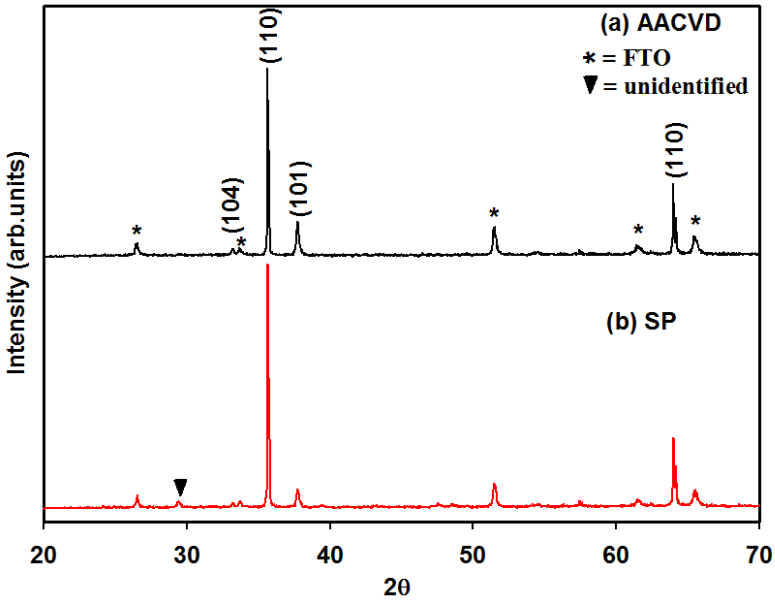

Figure 71: The XRD peak pattern of α-Fe_2O_3 electrodes deposited by SP and AACVD.

The SEM micrograph of the α-Fe_2O_3 electrode deposited by AACVD and SP are presented in Figure 72. As shown in Figure 72a, the electrode deposited by SP shows a mixture of thick nanoplates and triple pyramids microstructures. By using AACVD method, these nanoplates and triple pyramids becomes thinner and resulted in the formation of a leaf-like microstructure electrode as shown in Figure 72b. It is observed that α-Fe_2O_3 electrode deposited by AACVD shows high crystalline structured compared to the one deposited by SP. This could be due to the high deposition temperature in AACVD (500°C). It's reported that the deposition temperature has a significant impact on the structural properties of the α-Fe_2O_3 film such as crystallinity and phase.[32] Another reason could be due to both small and large particles decomposed on the FTO surface in electrodes deposited by SP. While in electrodes deposited by AACVD, the large particles are filtered by a trapped flask, leaving only small particles to travel through the tubes and decomposed on the FTO surface.

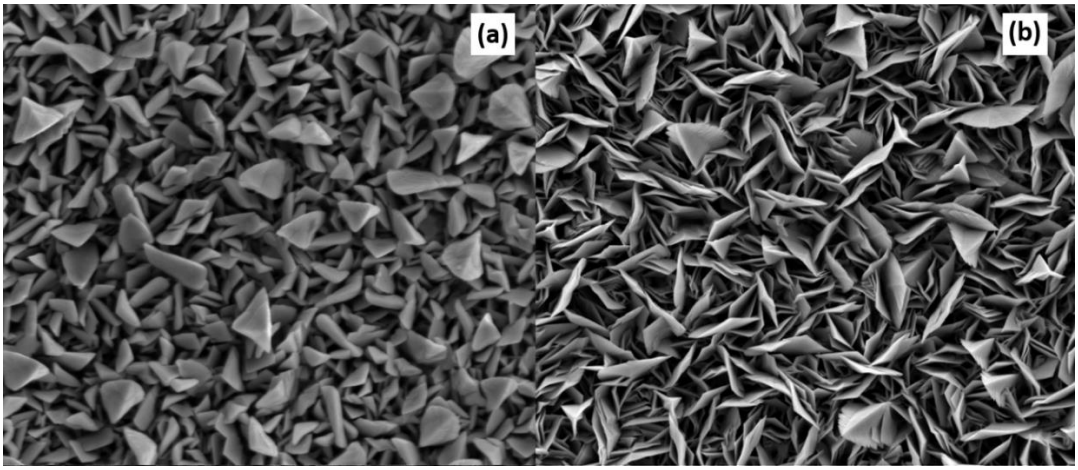

Figure 72: The SEM of α-Fe_2O_3 electrode deposited by; (a) SP. (b) AACVD.

7.3.2. Photoelectrochemical Analysis

The photoelectrochemical properties of α-Fe_2O_3 electrodes were investigated under chopped light (AM 1.5 illumination) in a 3-electrode open quartz cell in

order to reveal the dark current simultaneously. The steady-state *J*-V plots in Figure 73 show the photocurrent density of α-Fe_2O_3 electrodes deposited by AACVD and SP techniques. It's observed that the electrode deposited by AACVD exhibit highest photocurrent up to 2.5 mA cm^{-2} at 1.23 V vs. RHE. While the electrode deposited by SP has shown about 1.5 $mAcm^{-2}$ photocurrent density at 1.23 V vs. RHE. The result indicates that the textural properties are the key factor in defining the light harvesting and charge transfer properties.[33] The electrode deposited by AACVD has better crystalline structure resulted in highest photocurrent, which could be due to fact that the high internal surface area exposed to the electrolyte provides a large effective semiconductor/electrolyte interface. Thus, the separation of photogenerated carriers within the width of the space charge layer becomes a key factor to enhance PEC performance of photoelectrodes.

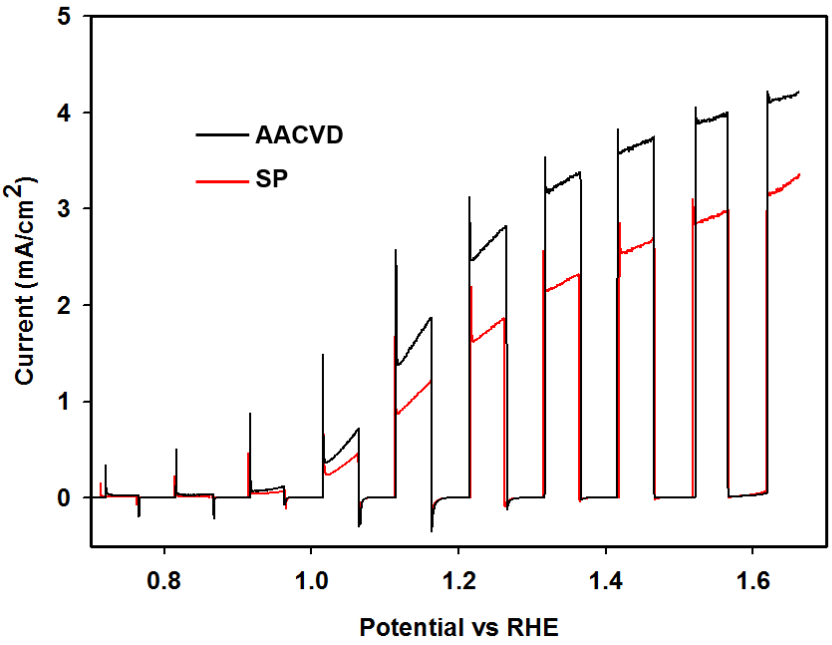

Figure 73: Photocurrent –potential (J-V) curve of α-Fe_2O_3 electrodes deposited by AACVD and SP.

7.3.3. Photovoltaic Analysis of α-Fe_2O_3 Counter Electrode

The photovoltaic analysis of DSSCs was obtained by other collaborated group member. The performance of α-Fe_2O_3 as counter electrodes in DSSCs was studied in comparison to that of the DSSCs with a Pt CE. Figure 74 shows the *J-V* characteristics of DSSCs fabricated by the prepared α-Fe_2O_3 CEs. The Photovoltaic parameters of these devices and the Pt CE device, including the short-circuit current (J_{sc}), the open-circuit voltage (V_{oc}), the fill factor (FF) and conversion efficiency (η), are reported in Table 1. From the table, different performance can be observed for the α-Fe_2O_3 samples prepared by different deposition methods. The energy conversion efficiency of 0.8% and 1.08% were obtained for the DSSCs applying α-Fe_2O_3 deposited by SP and AACVD respectively.

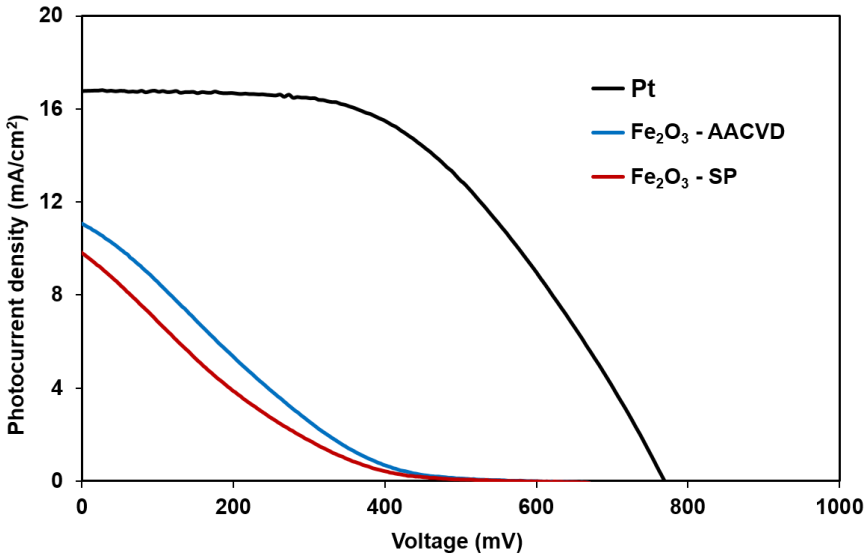

Figure 74: Photocurrent –voltage characteristic curve of DSSCs with different counter electrodes including Pt, α-Fe_2O_3 electrodes deposited by AACVD and SP.

Table 3: Photovoltaic parameters of DSSCs using Pt CE and α-Fe_2O_3 CE.

Device	J_{sc} [mA/cm^2]	V_{oc} [mV]	FF [%]	η [%]
Pt	16.92	769	50.5	6.57
Fe_2O_3- SP	9.91	507	16.0	0.80
Fe_2O_3- AACVD	11.16	518	18.7	1.08

J_{sc}: short-circuit current density, V_{oc}: open-circuit voltage, FF: fill factor, η: energy conversion efficiency.

The *J-V* curves presented in Figure 74 suggest that the impact of the CE morphology on the *J-V* characteristics of the fabricated solar cells is remarkable. α-Fe_2O_3 CE deposited by AACVD exhibit higher *J-V* characteristics than that of CE prepared by SP and that's due to its high crystalline surface. An increase in the crystallinity causes a less trap-state density, which seems to significantly affect the interfacial electron-transfer dynamics and lead to a slower electron recombination rate in this material.[34] However, the current density and conversion efficiency of α-Fe_2O_3 CE is much lower than Pt CE. Compared to α-Fe_2O_3 electrodes, Pt shows remarkable catalytic activity for I_3^- reduction with a sharp slope of current-voltage curve. The low performance of α-Fe_2O_3 could be due to various factors such as specific surface area, porosity and crystal plane orientation.[35] The morphology of counter electrode materials can act as an effective factor in improving the catalytic activity in a DSSC.[36,37]

7.4. Summary of α-Fe_2O_3 as Counter Electrodes

In this research, a facile deposition methods such as AACVD and SP were used to synthesis different morphologies of α-Fe_2O_3 as counter electrodes. Also, photovoltaic performance of different morphologies of α-Fe_2O_3 was examined.

The results show that the efficiency of the samples prepared by AACVD is higher than of the samples prepared by SP. Although, the performance of α-Fe_2O_3 with better crystalline exhibit higher electrocatalytic activity, it still far away from that of Pt. This lack of performance can be attribute to several reasons such as specific surface area, porosity, crystal plane orientation and morphology. The enhanced electrocatalytic activity of α-Fe_2O_3 counter electrodes leads to more efficient DSSCs. All the above findings will offer useful insights into designing and develop cost-effective and highly efficient CE structures in DSSCs.

7.5. References

(1) O'regan, B.; Grätzel, M. *Nature* **1991**, *353*, 737.

(2) Yella, A.; Lee, H.-W.; Tsao, H. N.; Yi, C.; Chandiran, A. K.; Nazeeruddin, M. K.; Diau, E. W.-G.; Yeh, C.-Y.; Zakeeruddin, S. M.; Grätzel, M. *Science* **2011**, *334*, 629.

(3) Labat, F. d. r.; Le Bahers, T.; Ciofini, I.; Adamo, C. *Accounts of Chemical Research* **2012**, *45*, 1268.

(4) Bai, Y.; Cao, Y.; Zhang, J.; Wang, M.; Li, R.; Wang, P.; Zakeeruddin, S. M.; Grätzel, M. *Nature Materials* **2008**, *7*, 626.

(5) Halme, J.; Vahermaa, P.; Miettunen, K.; Lund, P. *Advanced Materials* **2010**, *22*, E210.

(6) Calogero, G.; Calandra, P.; Irrera, A.; Sinopoli, A.; Citro, I.; Di Marco, G. *Energy & Environmental Science* **2011**, *4*, 1838.

(7) Hu, Y.; Yella, A.; Guldin, S.; Schreier, M.; Stellacci, F.; Grätzel, M.; Stefik, M. *Advanced Energy Materials* **2014**, *4*, 1400510.

(8) Ahmad, I.; McCarthy, J. E.; Bari, M.; Gun'ko, Y. K. *Solar Energy* **2014**, *102*, 152.

(9) Ahn, J. Y.; Kim, J. H.; Kim, J. M.; Lee, D.; Kim, S. H. *Solar Energy* **2014**, *107*, 660.

(10) Tsao, H. N.; Burschka, J.; Yi, C.; Kessler, F.; Nazeeruddin, M. K.; Grätzel, M. *Energy & Environmental Science* **2011**, *4*, 4921.

(11) Tai, Q.; Chen, B.; Guo, F.; Xu, S.; Hu, H.; Sebo, B.; Zhao, X.-Z. *ACS nano* **2011**, *5*, 3795.

(12) Tian, H.; Yu, Z.; Hagfeldt, A.; Kloo, L.; Sun, L. *Journal of the American Chemical Society* **2011**, *133*, 9413.

(13) Wang, Y. C.; Wang, D. Y.; Jiang, Y. T.; Chen, H. A.; Chen, C. C.; Ho, K. C.; Chou, H. L.; Chen, C. W. *Angewandte Chemie* **2013**, *125*, 6826.

(14) Xin, X.; He, M.; Han, W.; Jung, J.; Lin, Z. *Angewandte Chemie International Edition* **2011**, *50*, 11739.

(15) Wu, M.; Lin, X.; Wang, Y.; Wang, L.; Guo, W.; Qi, D.; Peng, X.; Hagfeldt, A.; Grätzel, M.; Ma, T. *Journal of the American Chemical Society* **2012**, *134*, 3419.

(16) Jiang, Q.; Li, G.; Gao, X. *Chemical Communications* **2009**, 6720.

(17) Wu, M.; Ma, T. *ChemSusChem* **2012**, *5*, 1343.

(18) Wang, H.; Wei, W.; Hu, Y. H. *Journal of Materials Chemistry A* **2013**, *1*, 6622.

(19) Wu, M.; Wang, Y.; Lin, X.; Yu, N.; Wang, L.; Wang, L.; Hagfeldt, A.; Ma, T. *Physical Chemistry Chemical Physics* **2011**, *13*, 19298.

(20) Brennan, L. J.; Byrne, M. T.; Bari, M.; Gun'ko, Y. K. *Advanced Energy Materials* **2011**, *1*, 472.

(21) Das, S.; Sudhagar, P.; Verma, V.; Song, D.; Ito, E.; Lee, S. Y.; Kang, Y. S.; Choi, W. *Advanced Functional Materials* **2011**, *21*, 3729.

(22) Kang, S. H.; Choi, S. H.; Kang, M. S.; Kim, J. Y.; Kim, H. S.; Hyeon, T.; Sung, Y. E. *Advanced Materials* **2008**, *20*, 54.

(23) Dotan, H.; Sivula, K.; Grätzel, M.; Rothschild, A.; Warren, S. C. *Energy & Environmental Science* **2011**, *4*, 958.

(24) Zhong, L. S.; Hu, J. S.; Liang, H. P.; Cao, A. M.; Song, W. G.; Wan, L. J. *Advanced Materials* **2006**, *18*, 2426.

(25) Yan, W.; Fan, H.; Zhai, Y.; Yang, C.; Ren, P.; Huang, L. *Sensors and Actuators B: Chemical* **2011**, *160*, 1372.

(26) Andreola, F.; Barbieri, L.; Bondioli, F. *Dyes and pigments* **2012**, *94*, 207.

(27) Hou, Y.; Wang, D.; Yang, X. H.; Fang, W. Q.; Zhang, B.; Wang, H. F.; Lu, G. Z.; Hu, P.; Zhao, H. J.; Yang, H. G. *Nature communications* **2013**, *4*, 1583.

(28) Yang, W.; Xu, X.; Li, Z.; Yang, F.; Zhang, L.; Li, Y.; Wang, A.; Chen, S. *Carbon* **2016**, *96*, 947.

(29) Agarwala, S.; Lim, Z.; Nicholson, E.; Ho, G. *Nanoscale* **2012**, *4*, 194.

(30) Ocakoglu, K.; Krupnik, T.; van den Bosch, B.; Harputlu, E.; Gullo, M. P.; Olmos, J. D. J.; Yildirimcan, S.; Gupta, R. K.; Yakuphanoglu, F.; Barbieri, A. *Advanced Functional Materials* **2014**, *24*, 7467.

(31) Narra, V. K.; Ullah, H.; Singh, V. K.; Giribabu, L.; Senthilarasu, S.; Karazhanov, S. Z.; Tahir, A. A.; Mallick, T. K.; Upadhyaya, H. M. *Polyhedron* **2015**, *100*, 313.

(32) Martinez, A.; Pena, J.; Labeau, M.; Gonzalez-Calbet, J.; Vallet-Regi, M. *Journal of Materials Research* **1995**, *10*, 1307.

(33) Yang, B.; Zhang, Y.; Drabarek, E.; Barnes, P. R.; Luca, V. *Chem. Mater.* **2007**, *19*, 5664.

(34) Shahpari, M.; Behjat, A.; Khajaminian, M.; Torabi, N. *Solar Energy* **2015**, *119*, 45.

(35) Wang, W.; Pan, X.; Liu, W.; Zhang, B.; Chen, H.; Fang, X.; Yao, J.; Dai, S. *Chemical Communications* **2014**, *50*, 2618.

(36) Lan, Z.; Wu, J.; Lin, J.; Huang, M. *Journal of Materials Chemistry* **2012**, *22*, 3948.

(37) Duong, T.-T.; Choi, J.-S.; Le, A.-T.; Yoon, S.-G. *Journal of The Electrochemical Society* **2014**, *161*, H166.

Chapter 8: Conclusion and Future Work

8.1 Conclusion

The work detailed in this thesis has covered a detailed study on the fabrication and design of nanomaterials for solar energy conversion and photo-catalytic applications. One of the main contributions of our work is to study new material and investigate there application in hydrogen generation and photo-catalytic dye degradation.

A comprehensive literature on different materials used for photoelectrochemical water splitting and photocatalytic water treatments have been provided. In particular, investigate the basic principle and mechanism behind water splitting and dye degradation processes have been investigated. This allows us to investigate a new material that can strudel these reactions efficiently. The materials used in these reactions have to satisfy three conditions in order to perform high- efficiency solar water splitting and photocatalytic dye degradation. They should have an appropriate bandgap energy, a suitable position of the bandgap, and chemical stability. Moreover, the nanostructured thin film shows superiority over nanoparticle powders that have issues of recollection and their toxicity to the environments which hinder their use in hydrogen generation and photocatalytic application.

P-type $YFeO_3$ photocathode fabricated by a novel and inexpensive spray pyrolysis technique has yields a photocurrent density of 0.6 mA cm^{-2} at 0.5 V vs. RHE. In addition, $YFeO_3$ photocathode has shown high stability with a p-type response over a 21 hour period. Optical measurements showed that the photoelectrode has a bandgap of 2.45eV. Water splitting test prove that the

$YFeO_3$ photocathode generate 0.41 μmol/cm^2 of hydrogen after 6 hours without external bias. The second cycle of hydrogen test proves that the electrode is re-usable and 0.35 μmol/cm^2 of hydrogen is generated after 6 hours of light illumination. These findings undoubtedly prove that $YFeO_3$ is a potential candidate to act as a photocathode for unassisted water splitting to generate hydrogen at a competitive cost.

Bi_2WO_6 photoelectrode is successfully fabricated with controlling texture using spray pyrolysis (SP) process and photocatalytic performance in degradation of Rhodamine B(RhB) is investigated. It is found that the annealing temperature has a strong influence on the texture, morphology and the photocatalytic activity of Bi_2WO_6. The sample prepared at high temperature (525°) has shown high photocatalytic activity and complete degradation of RhB is achieved in 45min.

Bi_2WO_6 photoelectrode is successfully fabricated using aerosol assisted chemical vapour deposition (AACVD) method. There photocatalytic performance in degradation of methylene blue (MB) dye is investigated. It is found that the fabrication method and carrier gas flow have a strong impact on the texture, morphology and the photocatalytic activity of Bi_2WO_6. The sample prepared at low carrier gas flow with Hierarchical microsphere structures has shown the highest degradation efficiency of MB compared to the one prepared at high carrier gas flow.

Based on collaborated work, α-Fe_2O_3 electrodes with different morphologies are fabricated using facile deposition methods such as AACVD and SP. Its photovoltaic performance as counter electrodes in dye-sensitized solar cells (DSSCs) was examined. Our results show that deposition methods have a strong effect on morphology and photovoltaic performance of α-Fe_2O_3 electrodes.

Samples prepared by AACVD method possess high efficiency than of the samples prepared by the SP method. However, this performance still far away from that of Pt. The enhanced electrocatalytic activity of α-Fe_2O_3 counter electrodes leads to more efficient DSSCs. All the above findings will offer useful insights into designing and develop cost-effective and highly efficient CE structures in DSSCs.

8.2 Future Work

To the best of my knowledge, hydrogen is produced successfully for the first time spontaneously during a water splitting test without any external bias being applied using $YFeO_3$ photocathode as a single material. These results exhibit that $YFeO_3$ is a promising candidate to act as a photocathode for unassisted PEC water splitting to generate solar fuel (hydrogen) cost effectively. However further work is required to investigate and improve the efficiency and stability challenges of $YFeO_3$ photoelectrodes. If we intend solar-to-hydrogen devices to be competing with other sources of renewable energy there is need to lower both the cost of the materials and increase their efficiency (and to start testing photoelectrochemical devices bigger than 3 cm^2 !).

Future works on the $YFeO_3$ photocathodes will be focused on understanding and improving the efficiency and stability of this photocathodes. Doping has been proven to be a highly successful method of enhancing the photocatalytic activity of semiconductor materials. Noble metals such as gold and silver have the potential of improving performance and light-harvesting capabilities. Furthermore, investigation of new strategies and fabrication methods to improve the process of water splitting in the hope that it will become an industrially applicable clean energy resource in the near future.

Bi_2WO_6 photoelectrode shows potential photocatalytic performance in degradation different types of dyes such as MB and RhB. Future studies can be focused on understanding and improving their characteristic. Furthermore, employing the combination of chemical modification with different synthesis strategies can play an important role for further improvement.